

## DISSERTATION

# Novel applications of Secondary ion mass spectrometry in thin film analysis

ausgeführt zum Zwecke der Erlangung des akademischen Grades eines Doktors der technischen Wissenschaften unter der Leitung von

Ao.Univ.Prof.Dipl.-Ing.Dr.techn. Herbert Hutter

Am Institut für Chemische Technologien und Analytik

E 164

eingereicht an der Technischen Universität Wien

Fakultät für Technische Chemie

von

Dipl.-Ing. Karl Emanuel Mayerhofer

e9325086

Wilhelm Kress-Platz 29-31/67/9

A – 1110 Wien

(Herbert Hutter)

## **Danksagung:**

I would like to thank Prof. Herbert (“Hörbi”) Hutter for the possibility to perform this thesis in his research group, supporting this work at his best, further for his relaxed way of supervising the group, allowing a deep insight into SIMS subject.

Special thanks to Kurt Piplits. His unique knowledge of the SIMS equipment was essential for all high performance measurements. During my time working in this group he straightened out a few aerations.

I want to thank all the members of the teams I was honoured to cooperate with:

At first the group of Christoph Eisenmenger-Sittner, including Clemens Schrank and Erich Neubauer from the Institute of Solid State Physics for their patience on waiting for SIMS measurement periods, for providing samples and assists during the whole thesis;

Martina Griesser and René Traum from the Kunsthistorisches Museum for the most interesting topic and the warm welcome to their community;

The team round Prof. Uwe Breuer from the Forschungszentrum Jülich for their short-termed allocation of their device for a few days’ measurements and the profound backup in TOF-SIMS knowledge (especially the tutorials in data interpretation);

Prof. Gerhard Hobler, Alexander Burenkov as well as Prof. Palmetshofer for providing samples and their support in the complex topic of implantation simulation;

And last but not least Peter Wilhartitz for the toughest SIMS-sessions during my work, whose samples gave interesting insight into the state of the art of high tech sputter deposition.

Special credits are due to my group members during my work with the SIMS-group, especially to Dragan Krekar for his friendship and company at our group during most part of the time, also Dr. Martin Rosner, Dipl.-Ing. Michael Fuchs, Dipl.-Ing. Jürgen Zwanziger, Dipl.-Ing. Markus Hochegger and last but not least Dipl.-Ing. Johann Moser; additionally Dr. Johannes Foisner and Dr. Andreas Glaser for their company.

I want to thank “FWF – Fonds zur Förderung der wissenschaftlichen Forschung” for the financial support of the research project.

Ganz besonderer Dank geht an meine ganze Familie, besonders meinem Vater Karl, Mutter Eva, meiner Großmutter und auch meinem Bruder Helmut für ihre finanzielle und geistige Unterstützung, die dieses Studium erst ermöglicht hat, aber natürlich auch allen Mitgliedern der Familie Lederer/Frühstück.

To all my friends, especially Michael, Raffaella, Thomas, Izzy, as well as Thomas, Flo, Misi, Albert and the rest of the Schubert-boys (here not forgetting Mr. Trabesinger) for being real mates!

1. ABSTRACT.....	6
1.1. Zusammenfassung in deutscher Sprache.....	8
2. INTRODUCTION.....	10
3. SECONDARY-ION MASS-SPECTROMETRY .....	14
3.1. Principles .....	14
3.2. Sputter regime and secondary ion generation.....	15
3.3. Device assembly .....	16
3.3.1. Vacuum system .....	17
3.3.2. Primary ion guns .....	17
3.3.3. SIMS mass analyzers .....	18
3.3.4. Ion detection systems .....	19
3.4. The CAMECA IMS series.....	20
3.4.1. A brief history of the TU-Wien SIMS device and the present TU-Wien device configuration.....	21
3.5. Dynamic SIMS detection modes .....	22
3.5.1. Offset voltage .....	22
3.5.2. Mass scan .....	22
3.5.3. Depth profile .....	22
3.5.4. Direct imaging mode.....	23
3.5.5. Scanning imaging mode.....	23
3.5.6. 3D imaging.....	24
3.6. Static SIMS detection modes.....	24
3.6.1. Surface imaging.....	25
3.6.2. Depth profiling .....	25
3.6.3. 3D analysis .....	25
3.7. Illuminated area vs. analyzed area.....	26
3.8. Crater depth evaluation.....	26
3.9. SIMS data processing .....	27
3.9.1. Adjusting depth profiles with reference masses.....	27
3.9.2. Signal background determination.....	28
3.9.3. Quantification.....	29

4. RESEARCH.....	31
4.1. Research on the enhancement of Cu-C layers .....	31
4.1.1. Comparison of samples electrochemically and sputter deposited.....	34
4.1.2. Comparison of samples as deposited and heat treated .....	45
4.1.3. Hydrogen and nitrogen plasma pre-treated samples .....	46
4.1.4. Chromium intermediate layers .....	49
4.1.5. Molybdenum intermediate layers.....	51
4.2. Investigations on Corrosion of golden coins and medals .....	54
4.2.1. Investigations with dynamic SIMS .....	55
4.2.2. Investigations on historic coins with TOF-SIMS.....	64
4.2.3. Conclusion on the gold research .....	83
4.3. SIMS profile analytics attending research on implantation simulation.....	85
4.3.1. Research on Erbium implantations .....	86
4.3.2. Simulation of boron channelling .....	88
4.4. Quantification of oxynitride layers by evaluation of $MCs^+$ secondary ions.....	92
5. PUBLICATIONS.....	94
5.1. Characterization of Cr intermediate layers in Cu-C-system with SIMS method ...	95
5.2. Adhesion promotion of Cu on C by Cr intermediate layers investigated by the SIMS method .....	96
5.3. Influence of thermal treatment on the adhesion of copper coatings on carbon substrates.....	97
5.4. Characterization of molybdenum intermediate layers in Cu-C system with SIMS method .....	98
5.5. Dose-rate dependence of damage formation in Si by N implantation as determined from channelling profile measurements .....	99
5.6. Range evaluation in SIMS depth profiles of Er-implantations in silicon.....	100
5.7. Multiscale approach for the analysis of channelling profile measurements of ion implantation damage.....	101
5.8. Quantitative SIMS depth profiling of diffusion barrier gate-oxynitride structures in TFT-LCDs .....	102
5.9. Investigations of corrosion phenomena of gold coins with SIMS.....	103
5.10. Brown spot corrosion on historic gold coins and medals .....	104
6. IMAGES.....	106

## 1. Abstract

40 years of development of Secondary ion mass spectrometry have turned this method to an important technology in surface and thin film analysis of solids. Especially with the introduction of TOF-SIMS the field of application has broadened eminently. This work focuses three topics out of a few, realised within this PhD-Thesis. It centres the adoption of dynamic SIMS technology to novel applications.

1) Investigations on novel materials: Materials science often uses means of SIMS in the characterisation of new materials. In this study carbon fibres and copper should merge to a novel material with high thermal conductivity and tailorable coefficient of thermal expansion (CTE). In order to enhance the adhesion of both materials, several tests with surface pre-treatment and investigations with interlayers of chromium or molybdenum have been performed. SIMS was able to characterise the elemental distribution in thermally deposited test layers.

2) SIMS application in the investigation of historical objects: The minimal sample destruction and the enormous gain on information from the measurement makes SIMS a suitable method of choice. This study investigates corrosion stains on gold coins. In a first run only test coins were investigated, a second run, performed with a TOF-IV device at the Kernforschungszentrum Jülich, also consisted of two historical coins from the 19<sup>th</sup> century. SIMS studies revealed the presence of silver and copper at the corrosion stains in connection with sulphur and some chlorine. The silver grains imprinted into the test coin surface and treated with  $K_2S_x$  for 5 hours at 60° C were still partly metallic, whereas all stains at the ancient coins seems fully corroded.

3) Characterisation of implantations in order to confirm simulation calculations: Computer simulations of ion implantations are widely used in semiconductor research and development. Still in some applications a minor mismatch between simulation and practise is observable. SIMS measurements accompanied two investigations on the implantation of rare earth element erbium and on the defect simulation of boron channelling implantation. Both studies

afforded a maximum precision and repeatability of the measurement. This study also takes a closer look at the depth evaluation, especially when interpreting near surface regions.

## 1.1. Zusammenfassung in deutscher Sprache

Sekundärionen Massenspektrometrie (SIMS) hat sich in den 40 Jahren ihres Bestehens zu einer wichtigen Methode in der Oberflächen- und Dünnschichtanalytik entwickelt. Besonders mit der Einführung der Flugzeit Massenspektrometrie hat sich das Anwendungsgebiet deutlich erweitert. Diese Arbeit konzentriert sich auf drei Themen, welche im Rahmen dieser Dissertation durchgeführt wurden. Dabei wird besonders Wert auf die Erschließung neuer Anwendungsgebiete für die dynamische SIMS gelegt.

1) Untersuchungen an neuartigen Materialien: In der Materialwissenschaft wird oftmals SIMS bei der Charakterisierung neuer Materialien herangezogen. In der vorliegenden Studie sollen Kohlenstofffasern und Kupfer zu einem neuartigen Material mit hoher thermischer Leitfähigkeit und frei anpassbarem thermischen Ausdehnungskoeffizienten verbunden werden. Zur Verbesserung der Haftfestigkeit der beiden Materialien wurden Versuche mit vorbehandelten Oberflächen sowie mit Zwischenschichten aus Chrom oder Molybdän durchgeführt. Dabei konnte die Verteilung der Elemente in thermisch beschichteten Testproben mit SIMS charakterisiert werden.

2) Anwendung von SIMS bei der Untersuchung von historischen Objekten: Die geringe Zerstörung der Oberfläche, und der enorme Informationsgewinn der Messung machen SIMS zu einer idealen Methode für die Untersuchung von historischen Objekten. In dieser Studie wurden Punktkorrosionen an Goldmünzen des Kunsthistorischen Museums, Wien, untersucht. Dabei wurden in einer ersten Messserie nur Testmünzen untersucht, eine zweite Serie, welche auch historische Münzen aus dem 19. Jahrhundert beinhaltete, wurde mit einem TOF-IV Gerät am Forschungszentrum Jülich durchgeführt. Die SIMS Messungen zeigten, dass die Korrosion vor allem an Splintern aus Kupfer und Silber unter Bildung von Sulfiden und Chloriden stattfindet. Dabei waren die in die Testmünzen eingepprägten Metallspäne nach einer 5-stündigen Behandlung mit  $K_2S_x$  bei  $60^\circ C$  noch immer teilweise metallisch, wohingegen die Splitter an den historischen Münzen gänzlich korrodiert waren.

3) Charakterisierung von Implantationen zur Bestätigung von Simulationsrechnungen: Der Einsatz von Computersimulationen von Ionenimplantationen ist in der Halbleiterentwicklung weit verbreitet. Dennoch ist in einigen Randanwendungen eine Abweichung von Simulation



und Praxis zu bemerken. SIMS begleitete zwei Studien, eine betreffend die Implantation schwerer Seltenerdelemente am Beispiel von Erbium, eine über die Defektabhängigkeit von Bor-, „Channeling“-Implantationen. Dabei wird auch Augenmerk auf die Ermittlung der Tiefenskala gelegt, besonders in Zusammenhang mit oberflächennahen Regionen.

## 2. Introduction

In the last centuries, secondary ion mass spectrometry has become a well established high end analysis method in a wide field of application. With increasing requirements on high tech products (miniaturization, advanced materials, increasing output, decreasing material cost...) the research of new technologies more and more accesses advanced analysis techniques such as SIMS. With this method the researcher is able to gather data from the materials composition in lateral direction as well as from several nanometres depth, with an included ability of data quantification. Its major disadvantage is the complex data interpretation, which requires trained scientific personal. For a long time this prevented SIMS from becoming a universal method in materials science. With the introduction of a new application of SIMS, the Time of Flight SIMS, device costs sank to about 1 Mio Euro for a basic unit (recent TOF V by IONTOF [1]), on the other hand increased its field of application drastically. Additionally a recent British low cost application (Mini SIMS by Millbook Instruments Ltd. [2]) accesses the field of routine analytics for SIMS application.

Secondary ion mass spectrometry was developed in 1949 by Herzog and Viehböck [3], first serviceable applications were applied in the early 1960s from two independent groups [4,5]: by Herzog and Liebl [6] from the GCA corp. in cooperation with the NASA and at the University of Orsay by Castaing and Slodzian [7]. In its now 40 years of development it has become a most powerfully method in surface analytics. Most important areas of application are:

- Semiconductor analytics (depth profiling, quantification, contamination monitoring...)
- Thin films (adhesion, diffusion, wettability...)
- Metal and metal oxide films (segregation, diffusion...)
- Insulator materials (ceramics, glass...)
- Organic substrates (polymers, paper...)
- Biomaterials and Pharmaceuticals

First three categories are classical applications to conventional dynamic SIMS (see also chapter 3). Recent developments have widened this area of application to small sized insulating materials and established organic compound analysis with SIMS.

At hand for this work was an enhanced CAMECA IMS 3f. This device is still restricted to classical application (TOF-SIMS data presented in chapter 4.2 “Investigations on Corrosion of golden coins and medals” are more kind of recent SIMS analytics). Nevertheless, in some areas, an up to date level of investigation is still obtainable.

In this thesis, three topics are chosen out of a few done within this PhD work representing a state of the art application of secondary ion mass spectrometry. Our workgroup focuses the enhancement of the measurement process itself. This implicates, that there is no facility for sample creation available. That’s why all topics presented here were done in cooperation with other institutions.

The first application is a project on copper-carbon-composites (chapter 4.1). It was done in cooperation with the thin film group of Prof. Eisenmenger-Sittner at the Institute of Solid State Physics. Composites give ability to combine two completely different materials into a novel one and enable the composition of high tech materials with widely tailorable properties. In copper-carbon composites, two materials with high thermal conductivity are joined. Aim of this project was the development of a composite with high thermal coefficient and a tailorable coefficient of thermal expansion (adjustable to changing substrate materials). Common fabrication routines for such materials base on powder metallurgical joining of copper powder and nanometre sized carbon fibres. The low wettability of copper and carbon causes the resulting material to become brittle and thermally instable and thus it may not confirm requirements. This project should point out the possibility of enhancing the adhesion of copper and carbon first by using thermal and electrochemical deposition and second by insertion of an interlayer. SIMS should thereby investigate the distribution of the used materials in the deposited layers (main compounds copper, carbon, the interlayer materials chromium or molybdenum, and some trace elements respectively). We were able to show diffusion processes and changes in the chemical composition, sometimes corrupting, sometimes enhancing the adhesion (adhesion tests were performed at the Institute of Solid State Physics).

Second SIMS task was done in cooperation with the “Kunsthistorisches Museum”. The application of SIMS in analytics of ancient artefacts opened up in recent years. Investigations on historical objects require the acquisition of maximal information from minimal sample volume (ideally non-destructive). Though SIMS is a destructive method, its high information depth is predestined to such investigations. Topic of this very investigation is the research on the corrosion of historical gold coins (see also chapter 4.2). When in 1998 the coin cabinet of the “Kunsthistorisches Museum” started a reassignment of its collection, a few gold coins

were detected to have spots of different size (100  $\mu\text{m}$  to several mm) and colour (reddish brown to black) at the surface. These spots were first investigated by several non-destructive methods like electron microscopy, AES (Auger electron spectroscopy), XPS (X-Ray photoelectron spectroscopy) and isoelectric focusing before getting in touch with SIMS the first time. SIMS investigations on the coins were designated to give a complete view on the distribution of the main and trace elements in the corroded area. Investigations were done in two parts: In the first part measurements were carried out at two test-coins prepared at the “Münze Österreich”. The measurements were done with the SIMS-device at hand at the Technical University (an enhanced “CAMECA IMS 3F” dynamic SIMS device). The second part of this investigation was performed with a TOF-SIMS instrument (TOF IV) at the “Kernforschungszentrum Jülich”. The investigation showed copper and silver stains of several 100  $\mu\text{m}$  size with a coverage of sulphide and chlorine (XPS showed  $\text{Ag}_2\text{S}$  at the surface) in the investigated corroded areas. Additionally both SIMS methods were able to show an encrustation of the surface with organic material, detected via the carbon and oxygen distribution.

The third investigation concludes depth profiling measurements, which were designated to support the research on the modelling of implantation mechanism. The workgroup of Gerhard Hobler at the “Institut für Festkörperelektronik” is working on the simulation of ion implantation with focus on the damages done by the implanted ions. Two tasks were done within this thesis. In a first erbium was implanted into silicon. Due to common implantation simulation programs basing on a few fully characterized implantations of lightest elements (hydrogen, helium, lithium), there is supposed to be a mismatch between simulation and real implantation when implanting heavy elements. Erbium is one heavy element, whose implants are of technical use. SIMS investigations concentrated on an as close as possible evaluation of the depth distribution of erbium in the silicon substrate. Additional enhancements of the depth scale were performed, including a correction of the deviant sputter rate at the surface.

Another SIMS investigation on implantation simulation was performed with subsequent implants of nitrogen and boron. This study was assigned to reveal the influence of a previous nitrogen implantation on the subsequent boron implantation. The nitrogen implantation rate (implantation dose per second) varied; boron was implanted in channelling direction (direction of the crystalline plane of the substrate). The investigation revealed that the influence on the boron implantation caused by the nitrogen defects is constant over a wide range of the implantation rate. Only over approximately 200 nA/sec the channelling portion of

the boron implantation drops slightly. This effect was predicted from simulation, but at a much lower value. The cause for this mismatch is still under discussion.

### 3. Secondary-ion mass-spectrometry

Secondary Ion Mass Spectroscopy is a powerful tool among the major techniques of surface analysis and microstructure characterization of solids.

SIMS is denoted for its outstanding sensitivity of chemical and isotopic detection. Quantitative or semiquantitative analysis can be performed for small concentrations of nearly all elements in the periodic table, including the lightest e.g. hydrogen, lithium, and boron, which are out of range for most other common solid state detection methods. However, the high versatility of SIMS is mainly due to the combination of high sensitivity with good topographic resolution both in depth and laterally (for imaging SIMS).

R. Viehböck and F. Herzog develop the principles in the 1940ies from mass spectroscopy [3]. Since then a lot of modifications and improvements have been improved the method considerably to its present state.

#### 3.1. Principles

Secondary-ion mass-spectrometry is the analysis method of detecting mass separated ions formed by sputter depletion of material from a sample surface by high energy ion beams. Its benefits are summarized below [8].

- Detection limit below 1ppm for all elements, some limits reach ppb range.
- All elements are detectable.
- Isotopes are distinguishable.
- Depth resolution of lower than 1nm is possible, ~10nm are typical.
- Lateral resolution of typically 1  $\mu\text{m}$ , with certain ion sources down to 20 nm.
- Quantification with standards and RSF-values possible.
- Insulators analyzable.
- Capability of recording depth profiles.
- 3 dimensional visualisation of data.

Disadvantages of SIMS are the sample destruction during analysis and the dependence of the ion yield on the element species and the matrix and due to the handling of atoms and ions SIMS needs high vacuum conditions.

Due to its detection system, two types are presently in use:

**Dynamic SIMS:** uses constant working ion beams for depletion; the ion analysis is done with scanning mass spectrometers like double focusing mass spectrometers or quadrupole mass spectrometers. Benefits are the high detection sensitivity down to  $10^{14}$  atoms/cm<sup>2</sup> (~10ppb); drawback is the restriction of detecting each mass separately. Devices of this type are all CAMECA IMS-series [9] (using double focusing ion separation), the former ATOMECA devices (also CAMECA now, equipped with quadrupole mass separator), but also the Millbrook mini-SIMS [2].

**Static SIMS:** works with pulsed ion beams in combination with time of flight mass analyzers. Their advantage is a high mass resolution and the benefit of recording whole mass spectra with each pulse. The static/dynamic SIMS classification was previously introduced by Benninghoven [10] in opposition to dynamic SIMS. It figures out the low sputter rate permitting longer data acquisition at a single spot without degradation with static SIMS.

### 3.2. Sputter regime and secondary ion generation

The process of sputtering separates into three regimes according to the ion mass and impact energy [11].

At low energy ( $< 10$  eV) and/or mass respectively **Single-Knock-On-Regime** is the pre-dominating sputter mechanism; each input ion knocks a single particle out of the surface by directly knocking on or by direct transmission of thermal energy (evaporation).

The **Linear Collision Cascade** (0.1 – 20 keV) is the dominating sputter mechanism in SIMS [4]. The ion penetrates the sample and initiates in a certain depth a collision cascade (dependent on the mean free path of particles in solids). Some branches of this cascade proceed back to the surface and knock some particles from the first few atomic layers into the vacuum. Both the ion penetration and the particle movement during the cascade cause atomic mixing within a certain region dependent on the ion mass and energy respectively. This is the limiting factor of the depth resolution in SIMS [8].

With more increasing the impact energy ( $> 10$  keV) the sputter mechanism turns to the **Thermal-Spike-Regime**, where the penetrating causes an evaporation of atoms in a few atomic layers radiance. But it has to be mentioned that the principle chance of sputtering particles and not just penetrating the surface and be implanted is dependent on the ion mass

and for atomic ions relatively small. On the other hand this mechanism is also discussed to be dominating at lower energy when molecule or cluster ions are in use ( $C_{60}$ ,  $Au_3$ ,  $Bi_3$  sources).

**Equation 1**

$$Y = \frac{\langle n \rangle}{n_{PI}}$$

Y	Sputter Yield
$\langle n \rangle$	average number of emitting particles
$n_{PI}$	number of primary ions hitting the surface

The sputter yield Y (Equation 1) of materials depends on the surface composition, the primary ion species, the ion impact energy and the impact angle [8, 11] and is in the range of 0.1 to 10 atoms per primary ion in typical SIMS measurements [8]. The impact energy is also influencing the depth resolution. A maximal sputter yield will be achieved with approximately 10 eV, the depth resolution is then about 10 nm, when the impact energy is reduced, the depth resolution becomes better, but also the sputter yield drops.

Some of these sputtered atoms become ionized when leaving the sample. The ionized quota of the sputtered atoms is in the range of 0.001% up to 2% (e.g. alkaline metals); it is as well dependent on the used primary ions and the species of the sputtered particle [8]. In the case of oxygen primary ions the top surface is oxidized, most of the sputtered ions are positively charged. In the case of caesium also a considerable part of negative charged ions are generated.

Mostly sputtered ions are single atom ions, but also molecule ions (typically up to 10 atoms) are generated. There are two important processes of molecule-ion generation: First one the direct sputtered clusters from the surface and second is the impact of sputtered ions or atoms with atoms in the residual gas above the sample.

Secondary ions are mostly single charged, but twofold and threefold charge is possible.

### 3.3. Device assembly

Both static and dynamic SIMS are classified into a primary part handling the target ions and a secondary part handling the ions stemming from the sample surface ion bombardment.

The **primary part** commonly consists of one or more ion sources, and a column, which is separating the ion species to a single mass and accelerating and focusing them onto the surface. In static SIMS devices also the beam pulsation is done here also.



The **secondary part** consists of the secondary ion accumulation, the mass separator (depending on the SIMS type) and the secondary ion detection units.

Both parts merge in the sample chamber. Here the sample is fixated. Besides the sample holder it may also contain optical monitoring devices (microscopes, cameras), sample stage coolers or heaters, electron flood guns, secondary electron detectors, oxygen leak inlets, optical profile detectors, and more.

### **3.3.1. Vacuum system**

SIMS is a surface sensitive method. The coverage with adsorbate from the residual gas has to be repressed to preserve clean surfaces during measuring. The maximum pressure in the sample chamber therefore is dependent on the average recovering rate. SIMS needs a half-time of the surface recovery in the minute range (dynamic SIMS) or hour range (static SIMS) respectively. Therefore ultra high vacuum ( $10^{-7}$  to  $10^{-9}$  mbar) is necessary. For the primary part mostly  $10^{-5}$  mbar are sufficient (limiting is the mean free path of the ions), the secondary part mostly needs ultra high vacuum as well to suppress detector background noise. In most recent devices high vacuum conditions are provided by turbo molecular pumps in combination with rotary vane pumps, older systems may also use cryo-pumps and sublimation pumps [12].

### **3.3.2. Primary ion guns**

A main characteristic of SIMS is the surface depletion by bombarding ions. The used sputter beam has to achieve some of the conditions described as follows:

- High sputter yield of sample material with used ions
- High ion current for fast sample ablation
- Narrow focus for high image resolution, especially in raster mode (see chapter 3.5.5)
- Low surface roughening throughout sputtering
- High ion formation probability with used ions
- Narrow pulse width in static SIMS

Some of these articles are not to achieve together, the used ion gun setting is mostly a compromise according to the experimental conditions. Increasing requirements in modern TOF-SIMS devices afford the access of two ion guns, a continuous working sputter gun, and a pulsed analysis gun.

There are 4 types of ion sources commonly used with SIMS devices [13]:

The **Electron impact** (EI) ion source is the simplest type. It gains a high ion current, but a broadened focus. Typically gaseous elements like oxygen or noble gases are used in this source, recently introduced  $C_{60}$  guns are of this type as well.

In a **Duoplasmatron** an arc plasma generates the ions (as well of gaseous elements). It is able to produce a better focused beam compared with an electron impact source, but the maximum ion current is lowered.

**Liquid metal ion guns** (LMIG) produce fine focus ion beams by extracting ions from a liquid metal film on a tungsten needle tip with high voltage. At the moment 3 elements are commercially available for this type sources: gallium, gold and bismuth. Due to the extremely low ion current together with a small focus, they are mostly used in static SIMS devices.

The **Caesium ion source** is a mixture of LMIG and EI-gun. Onto an electron beam heated tungsten frit caesium ions are extracted by an applied high voltage. This ion source is a compromise between high ion current and low beam diameter. Additionally caesium influences the ionization yield of electronegative ions and is therefore an often used sputtering element in SIMS.

### 3.3.3. SIMS mass analyzers

As described in chapter 3.1 the method SIMS splits up into two branches, static and dynamic SIMS. Each branch has its own typical mass analyzers: Dynamic SIMS devices ordinary are equipped with quadrupole or double focusing mass analyzers, static SIMS almost ever use time of flight analyzers:

The **magnetic sector field** (= double focusing mass analyser) is the most common analyser in high end dynamic SIMS devices. Ions are separated with a magnetic field according to their mass/charge ratio according to equation 2. This ratio is only dependent on the magnetic field  $B$ , the curve radius  $R$  in the magnetic sector (at its end sits the detector or the exit slit) and the ions kinetic energy shown by  $U_0$ . Due to the blur of latter, an electric sector field precedes the

magnetic sector, filtering deviant ions [13,14]. So the ion first gets focused by its kinetic energy, subsequently by its mass/charge ratio. Simultaneous detection of multiple masses is only possible with detector arrays.

**equation 2**

$$\frac{m}{q} = \frac{R_m^2 B^2}{2U_0}$$

m.....ion mass

g.....ion charge

R<sub>m</sub>.....radius of ion curvature

B.....magnetic field

U<sub>0</sub>.....ion accelerating voltage

The **Quadrupole** mass analyzer is an easy to use analyzer, but lacks in the transmission and mass resolution at high masses. It uses inhomogeneous oscillatory electric fields for mass selection [4]. Typically this detector is used as a single mass analyser, when used in multidimensional mass spectrometers also mass ranges are penetrably.

The **Time of flight mass analyzer** is predominating in static SIMS. It needs secondary ions generated with short pulses, accelerated into a field free drift tube, where the ions are separated according to their velocity. Presuming all ions have the same kinetic energy at their origin, the flight of heavier ions will take longer than lighter ones. With the application of a reflectron unit, bending the flight path with a certain angle, it is possible to compensate differences in the kinetic energy.

The high transmission of this analyzer is coupled with a high mass resolution [8].

Recently other detection systems like ion traps or triple quadrupole analyzers (e.g. [15]), basically known from organic mass spectrometry, have also been equipped to SIMS devices.

### **3.3.4. Ion detection systems**

Depending on the application, several detector types are commonly in use:

Dynamic SIMS commonly uses **secondary electron multiplier** for single ion detection. Each ion actuates an electron cascade of 10<sup>8</sup> electrons detected at the end. At an ion current of

$2 \cdot 10^6$  ions per second the detector is saturated. If the ion current exceeds, **faraday cups** are switched into the beam [13].

Static SIMS devices also use **microchannel plate electron multiplier arrays** (array of about 2000 channels, each  $10 \mu\text{m}$  in diameter,  $\sim 400 \mu\text{m}$  length, each tube operates like a secondary electron multiplier). The electron pulse is switched by a scintillator plate into a photon, which is detected by a photosensitive detector [14].

Some dynamic SIMS devices allow direct imaging with their stigmatic optics. The ions are detected with double channel plates (2 channeltron array layers are coupled to boost the electron current), generated photons are recorded by CCD-cameras subsequently [13].

### **3.4. The CAMECA IMS series**

Most investigations described in this work were performed with a strongly upgraded CAMECA IMS 3f. The basic IMS 3f dynamic SIMS device was patented in 1975 [16] and first introduced in [17] in 1979. Compared with similar instruments of that time it had the advantage of a direct imaging mode and a much better primary ion beam focus than any device. Changes in the geometry to a  $60^\circ$  inclined primary impact allowed an orthogonal secondary ion extraction.

Since its first introduction, CAMECA presented a series of upgrades and enhancements. The IMS 4f [18] in 1985 the secondary ion extraction system has been enhanced and besides other minor improvements a first caesium gun and a normal incidence electron gun has been presented (both were also implemented into the TU-Vienna device subsequently).

In the 5f device, presented in 1991 [19], the primary section has been improved. The common primary gun is now in the serial composition equipped with two ion guns: a duoplasmatron and a fine focus caesium ion gun. An upgrade for the 3f device was as well available and implemented into the TU-Vienna device. Additionally it has the opportunity of a second primary ion column allowing the use of a gallium liquid metal ion source.

The 6f device from 1993 [12] had an improved analysis chamber, ready for better pumping system, lowering the oxygen detection limit in ultra shallow depth profiles. Instead of former 4.5 keV secondary acceleration voltage this device works with  $\pm 10$  keV! This needed also enhancements in the secondary magnet (now a laminar magnet replaces the ..... ) and the electron gun. The IMS 7f shows dramatically better results in ultra shallow depth profiles

using a novel primary beam acceleration/deceleration system [20]. A new rotating sample holder represses surface roughening during sputtering (useful in ultra shallow depth profiles). It represents the actually device configuration put for sale. While upgrades of the series 4f and 5f were available for the IMS 3f, the improvements in the series 6f and 7f are no more compatible to the 3f configuration and therefore no upgrade is available [21].

### **3.4.1. A brief history of the TU-Wien SIMS device and the present TU-Wien device configuration**

The IMS 3f of the Technical University Vienna was purchased in 1980, first publications followed by 1981 [22,23].

According to the enhancements of the IMS-series (see previous chapter) the device has been equipped with the improved secondary ion extraction from the IMS 4f and the novel primary column from the IMS 5f including a fine focus caesium gun and a duoplasmatron.

Additionally some improvements were designed in the workgroup itself. In 1991, when CAMECA presented the IMS 5f, at our device a new interface was presented, linking the device to a DOS-compatible interface [24] (first time worldwide). It includes a novel magnet control unit (replacement of the installed 16 bit digital analogue converter by a 24 bit unit) allowing better magnet stabilization; a digital counting system allowing a readout frequency of down to 10 ms; a faraday cup plug in for better signal readout, a motor control unit for the sample positioner allowing a manual or automated sample positioning of down to 5  $\mu\text{m}$  precision.

Another enhancement was done in 1995 [25] regarding the primary beam: A digital beam control allows sweeping the beam with highest precision and enables recording of element maps of the surface limited only by the primary beam diameter (=scanning imaging).

The enhancements of the IMS 6f were no more compatible with the former 3f-5f geometry.

The device in its present configuration is very similar to an IMS 5f, able for depth profiling with caesium and oxygen primary ions with a depth resolution of down to 5 nm and imaging capability with lateral resolution of approximately 2  $\mu\text{m}$  (in seldom used scanning mode below 1  $\mu\text{m}$ ). Additionally an interface modification allows recording of 3 dimensional element mapping combining common depth profiling and imaging mode with automated

readjustment routines. The device control is performed with a self-developed software package [26], 3D profile visualization is as well unique in our group [27].

### **3.5. Dynamic SIMS detection modes**

Due to the varying geometry of dynamic and static SIMS devices, there are different measurement modes available both for dynamic and static SIMS.

#### **3.5.1. Offset voltage**

This is less a detection mode than a feature only available in dynamic SIMS. By shifting the secondary ion acceleration voltage it is possible to suppress signals from molecule ions.

In this behalf a certain voltage (commonly 80 to 500V) is subtracted from the sample high voltage (at IMS 3f devices 4.5 kV). Depending on this voltage the ion fraction passing the energy slit between electrostatic and magnetic sector varies in its initial energy (the energy distribution at the slit levels off, only the initiation energy of the passing ions becomes higher!). The higher the offset, the more ions will be repelled. Utilizing the different energy distribution of molecule and atomic ions [14], this is a possibility of blocking commonly low energy molecule ions.

#### **3.5.2. Mass scan**

The sector magnet sweeps with a given speed over the chosen mass area (or with given step size); the secondary ion beam is detected with the electron multiplier. For optimal resolution, the scan speed and the summation range can be varied.

#### **3.5.3. Depth profile**

A set of masses is measured in cycling mode mass by mass. Each mass is recorded a given time (commonly 1 second), then the magnet sweeps to the next one. After measuring the last mass of the set the loop starts again with the first one. Commonly (like in our software [26])

the masses are arranged from lowest to highest. The detection is done with an electron multiplier or faraday cup. In depth profiles it is possible to measure each mass with an individual offset value to reduce the background of molecule ions and residual gas (see also 3.5.1 Offset).

To prevent drifts of the secondary magnet calibrations can be implemented into the measuring routine. With our adapted device [24, 25] we are also able to correct charging of the sample surface up to ~1500V with another additional calibration routine, shifting the sample high voltage.

#### **3.5.4. Direct imaging mode**

With the channel plate (see 3.3.4 Ion detection systems) it is possible to obtain m/e resolved images of the sample surface. Using a CAMECA IMS device the imaged size is limited to a circular area with 150  $\mu\text{m}$  diameter. The lateral resolution of these pictures is 2  $\mu\text{m}$ .

Optimal image definition is gained by limiting the contrast diaphragm (an aperture at the first defocused plane of the secondary ion beam, which is able to sharpen the picture by filtering high deviated ions, reducing the brightness of the signal alike) and narrowing the energy slit (limits the energy distribution of the detected ions).

The stigmatic secondary tube of the CAMECA IMS equipment is optimized to 4500V sample voltage (correlating with 0V offset) and low initial ion energy. As a result, it is impossible to record images when using an offset voltage; the image will blur. A constant charging sample normally is also defocusing. By changing the sample high voltage in some cases images are possible, but the focus of these images is never as good as with non-charging samples.

#### **3.5.5. Scanning imaging mode**

Another chance obtaining images especially in devices without stigmatic secondary part is the scanning mode. A very fine focused (and thus weak) beam is moving a raster point by point over the surface. For each point the ion-detector (usually the electron multiplier) records the ion count. Provided the beam diameter is fine enough, it is possible to alter the detector signals to images of single masses with resolution of the raster pixel size. In common dynamic SIMS devices the resolution is better than 1 $\mu\text{m}$ , the NanoSIMS 50 [28] is able to

reach resolution of down to 50nm. Advantage of these images is the easier quantitation of the signals due to the direct qualitative information of each pixel.

### **3.5.6. 3D imaging**

3D imaging is a combination of depth profiling and imaging mode (direct as well as scanning imaging). Data of several images of a single mass combine to a three dimensional stack, gaining the view to a three dimensional distribution of this mass.

Combining direct imaging images, further quantitative information is necessary to calibrate the image brightness; a simple depth profile is monitoring the overall mass intensity. As a result each mass is detected both with the electron multiplier and afterwards with the channel plate during measurement. Usually direct imaging uses a high current primary beam, resulting in a fast sample ablation and an overall information depth of up to 10  $\mu\text{m}$ .

When stacks of scanning imaging images are used, there is no need of further quantitative information from a depth profile. Images are directly rendered to 3d-plots. Due to the necessity of a fine focused beam, this mode is only useful for thin samples; the low primary ion beam is not able to ablate much material during measuring (usually up to 100 nm). Alternative solution is using an intermediate for abrading the surface with a high current beam. This means loosing information, a circumstance especially applying to TOF-SIMS depth profiling.

## **3.6. Static SIMS detection modes**

In static SIMS the beam is firing pulses onto the sample. Due to detector latency each pulse gains single bit information of each atomic mass unit (amu) detected. The pulses are set onto the surface in a raster pattern. Simple mass spectra are available by summing up single mass spectra of all points. Completing one full scan of the raster pattern is called a cycle in comparison to dynamic SIMS depth profiles. The length of time recording a single cycle depends on the chosen mass resolution and the raster size and is ordinary in the range of a few seconds.



### **3.6.1. Surface imaging**

Detecting the distribution of single masses needs recording of several pulses at each raster point. The more points are recorded the bigger becomes the information depth. Images therefore sum up several cycles. Due to low abrasion of the measurement gun, the ablation of a full image scan is still within atomic layer size. The lateral resolution of these images is dependent on the raster pixel size and/or the primary beam diameter. With common instruments 500 nm lateral resolution are feasible.

### **3.6.2. Depth profiling**

The low ablation speed of the measurement gun disables recording of depth profiles. Modern TOF-SIMS instruments therefore are equipped with an additional sputtering gun, ablating the surface with high current and low energy (low impact depth of the primary ions!). It fires an ion pulse after a complete raster cycle onto the surface. So deeper regions become accessible to measurement. Thus TOF SIMS is able to record depth profiles similar to dynamic SIMS, with the advantage of all masses are available, also with lateral information, disadvantage is an overall lack of sensitivity to all masses.

### **3.6.3. 3D analysis**

As mentioned above, in a common static SIMS depth profile still each cycle contains data of the lateral distribution. Due to each cycle consists of a set of pixels, each containing single bit information, for proper 3D-analysis several cycles needs to be summed up. Still the information per pixel in the 3D-plot remains weak, unless a high amount of cycles are summed up, which means long lasting data acquisition.

### **3.7. Illuminated area vs. analyzed area**

Proper depth information in static as well as in dynamic SIMS needs equally ablation of the sample within the analyzed area. Directing a sputter beam onto a single point of the surface gives u- or even v-shaped craters. Therefore the sputter beam ordinary is directed with high frequency sweep-shaped over a wider area. The sweep diameter is chosen depending on the sputter beam shape and the anticipated maximum depth of the profile. The wider the sweep, the lower the ablation; the smaller, the more the measurement “sees” crater edges.

The analyzed area then is chosen once by the raster size of the measurement gun (TOF SIMS and dynamic SIMS scanning mode) or by an aperture in the secondary ion part limiting the analyzed area (dynamic SIMS).

### **3.8. Crater depth evaluation**

Depth profiling needs as the name implies, proper information of the depth. While a few devices are equipped with inline depth measurement units (light interference method using lasers), mostly the depth is measured off line after the SIMS measurement. There are several choices evaluating the depth of SIMS craters. Commonly used stylus method provides depth information with at best 1 nm accuracy for craters with at least 20 nm crater depth [11]. Better results may accomplish AFM, but this is only available to very ultra shallow depth profiles. Also well available are microscope image based methods, evaluating the depth from focus shifts of certain points of the surface.

### 3.9. SIMS data processing

SIMS generates a huge amount of data, which has to be processed to extract information and become comparable to each other as well as to other methods. This needs besides simple data plotting several correcting steps considering fluctuations of the primary ion beam intensity and changes in the secondary ion yield, evaluating the signal background, but also to quantify data.

#### 3.9.1. Adjusting depth profiles with reference masses

Normally the secondary ion yield is not stable over a longer period. Instabilities of the primary ion current (e.g. the CAMECA Cs<sup>+</sup> ion gun has a guaranteed stability of +/- 5% over 5 hours), variation of the sample position (height and sample edges causing changes in electric field conditions) change the secondary ion intensity and yield slightly.

In order to correct such influences, a reference signal is recorded subsequently, ordinary a constant matrix signal. The reference mass must fulfil certain conditions:

- Equal distribution in all samples: No enrichments or inclusion in the range of the SIMS resolution, best correction will do when the signal levels off in all samples (matrix signal).
- Negligible noise: As a disadvantage of the calculation the noise of the reference mass is added onto all other signals. A high signal/noise ratio increases the noise of all other masses.
- No or negligible signal background
- Similar offset value to most other elements: The behaviour of masses without offset differs from masses with low offset due to the presence of molecule ions. High offset values additionally change the primary beam position (beam impact angle is dependent on the sample high voltage).

The easiest correction is to fit the reference signal height of each profile by multiplying with a constant (Equation 3). Subsequently this constant is applied to each signal. This approach keeps the matrix signal progression, i.e. in samples with signals influencing the matrix signal or matrix changes. It is only advisable when the primary ion beam remains stable during one depth profile.

**Equation 3** 
$$I_i [s^{-1}] \cdot C = I_i^* [s^{-1}]$$

$I_i$ : Signal Intensity  
 $C$ : correction constant  
 $I_i^*$ : corrected signal intensity

When more exacting statements are recommended, or the ion beam was not stable during measurement, a correction point by point is usual. This needs a non influenced reference signal during the whole depth profile. In each cycle the signal data points are divided by the reference signal of this cycle (Equation 4)

**Equation 4** 
$$\frac{I_i [s^{-1}]}{R_i [s^{-1}]} \cdot C = I_i^* [a.u.]$$

$I_i$ : Signal intensity  
 $R_i$ : Reference signal intensity  
 $I_i^*$ : corrected signal  
 $C$ : normalizing constant

Here  $C$  is a correction factor to adjust the signals to the range of the original depth profile. This value has to be equal to all depth profiles. It is a merely chosen value only dependent on the average of the reference signal's intensity.

In profiles with changing matrices a correction layer by layer is possible.

### 3.9.2. Signal background determination

Usually all SIMS devices operate with a pressure of at least  $10^{-7}$  mbar in the sample chamber ( $\sim 3 \cdot 10^7 \text{ cm}^{-3}$ ; app. 10 minutes surface monolayer recovery [11]). During sputtering particles covering the surface will be removed, but yet residual gas molecules are re-covering the sample surface. Sputtering these particles result in a signal background. The residual gas is mostly composed of oxygen and nitrogen (from sample changing), hydrogen and helium (accumulated due to bad pumpability) and organic molecules (from lubricants...).

There are two possibilities of discovering a signal's background level:

- Measuring a clean sample (e.g. pure silicon: all non silicon signal intensities should be the background level).
- Calculation of background by changing the primary ion beam intensity. This method is chosen, when no clean samples are available. It needs a reference mass similar to the reference mass defined in the previous chapter. Additional condition is an assumed negligible background level and high overall signal, guaranteed from most matrix signals.

Latter method needs calculations as follows:

**Equation 5**

$$\frac{I_{\text{Int1}}(m_{\text{ref}})}{I_{\text{Int2}}(m_{\text{ref}})} = \frac{I_{\text{Int1}}(m) - I_{\text{backgr}}(m)}{I_{\text{Int2}}(m) - I_{\text{backgr}}(m)}$$

- $I_{\text{Int}}(m_{\text{ref}})$  Intensity of the background free mass ( $m_{\text{ref}}$ ) ( $I_{\text{backgr}}(m_{\text{ref}}) = 0$ )
- $I_{\text{Int}}(m)$  Intensity of another mass  $m$ , of which the background will be calculated.
- $I_{\text{backgr}}(m)$  Theoretical intensity of the signal originating from background
- Int1, Int2 Primary ion current levels

This formula presumes that the adsorption rate is constant at the whole sampled area and during the whole measurement. Additionally the area of secondary ion extraction (analyzed area) needs to be constant and much smaller than the area illuminated by primary ions.  $I_{\text{backgr}}(m)$  then gives the intensity (in counts per second) of the ions stemming from signal background.

Nevertheless, interpreting the results of such a background evaluation needs further expert knowledge. Detector saturation, a bad beam positioning, surface artefacts influence the results dramatically.

### 3.9.3. Quantification

Knowledge of the concentration of a species in a sample is one major task in analytics. Unfortunately, this is not the strong point of SIMS. SIMS needs standards for quantification. Accurate quantification is only practicable with well defined samples with equalling matrix. Interfaces and sample impurities affect it adversely.

The basic equation (Equation 6) describes the dependence of the secondary ion intensity on several parameters depending on the analyte characteristics (isotopic abundance, ionization probability), and process relevant characteristics (sputter yield, transmission).

**Equation 6**

$$I_s(^n A) = I_p \cdot c_A \cdot (\alpha_A \cdot Y \cdot f_{nA} \cdot \eta)$$

$I_s(^n A)$ : secondary ion intensity of the isotope n of the element A

$I_p$ : primary ion beam intensity

$c_A$ : concentration of the element A in the sample

$\alpha_A$ : ionisation probability of the element A

$Y$ : sputter yield

$f_{nA}$ : abundance of the isotope n of the element A

$\eta$ : transmission factor of the spectrometer

In this equation, some parameters (in Equation 6 all values within the brackets) are constant when samples with similar composition are in use and no change of measurement condition is done. Besides the concentration only the secondary ion intensity is variable. In a larger sample batch the stability is not as good as afforded. Usually a correction, similar to the description in chapter 3.9.1, is done by doing the calculation with a reference mass (matrix element). Thus most parameters cancel down:

**Equation 7**

$$\frac{c_A}{c_M} = S_{A,M} \cdot \frac{I_s(^a A) \cdot f_M}{I_s(^m M) \cdot f_A}$$

$c_A, c_M$ : concentration of analyte A or of the matrix element, respectively

$I_s(^a A), I_s(^m M)$ : secondary ion intensity of isotope a of element A or the matrix, respectively

$f_M, f_A$ : abundance of the isotope n of the element A or of matrix M, respectively

$S_{A,M}$ : Relative sensitivity factor (RSF) of element A in matrix M

The relative sensitivity factor is gathered from standard samples with homogeneous concentration or implantation profiles, both of known concentration in the same way.

## 4. Research

### 4.1. Research on the enhancement of Cu-C layers

The more the miniaturization of semiconductor devices proceeds, the more processor heating becomes the limiting factor. Enhancements of cooling units have turned these devices into high tech instruments in the last years. But the most need of improvement is due the gap within the coolant chain between semiconductor surface and the chip device outer hull. It needs a heat draining material contacting the semiconductor directly at the hot spot and transferring the heat away with most effectiveness. The employed material has to satisfy a few requirements. Most necessary are high thermal conductivity and equal thermal coefficient of thermal expansion (CTE) to the semiconductor material (mostly silicon). The latter is due to the spot-like appearance of heat causing tension to the contacting region. If the CTE of semiconductor and heat drain is not quite similar, a debonding is possible. Unfortunately commonly used materials with high thermal conductivity differ in their CTE from silicon. On the other hand materials with equal CTE are as bad heat drains as silicon itself. One chance may be a combination of materials into a composite.

The best heat conducting material by far is carbon [29]. Among the many modifications of this element diamond tops all solids with 2000 W/mK. Only single tube carbon nanotubes range higher, so far 3500 W/mK have been reached [30], from theory 6000 W/mK are possible[31]. Latter are still under development and not accessible to wider technical application. The use of compact diamond containing material fails both on materials costs and processability.

Similar, slightly worse physical properties to diamond has carbon fibre material. There are two common ways of producing carbon fibers: From PAN-threads (PAN=polyacrylnitrile) with low thermal conductivity or from spun pitch with high thermal conductivity [29] (both see table 1). Both diamond and fibers have a lower CTE than silicon. It needs a second material with reverse CTE properties. Widely used aluminium tends to corrode and diffuse into the carbon at higher temperatures [29]. Best thermal conductivity combined with a high CTE does have the metals copper and silver. Due to its lower price and better corrosion resistance copper was further investigated.

**Table 1:** some physical properties of heat conducting materials

Material		$\alpha$ [ppm/°K]	$\rho$ [g/cm <sup>3</sup> ]	$\lambda$ [W/m°K]	Reference
Silicon		2.6-4.1	2.3	150	
GaAs		6	5.3	46	
Copper				385	
C (diamond)		0.8-1.2	3,51	2000-2100	[29]
C (vitreous carbon)	Common		1.4-1.5	6-12	
	Sigradur G	2.6	1.42	6.3	[35]
C (carbon fibre, longitudinal)	PITCH-fibre			530-1100	[1]
	PAN-fibre			8-70	[1]
Single tube carbon nanotubes		-	-	1000-3500 (Theory up to 6000)	[30,31]

There are several ways of combining copper and carbon in order to form composite material. Some are very academic and therefore limited in their application due to high costs; some of them would be much more economic after optimizing the process parameters.

- *Powder metallurgical fabrication:* is the state of the art method. The composites are fabricated from copper powder blended with carbon fibers and subsequently cold and/or hot pressed (sintering, hot pressing, hot isostatic pressing...). The variety of methods allows customizing several product parameters such as density and porosity [32].
- *Processing precoated fibers:* provides a better contact of copper and carbon. Before joining the fibers, they get coated with copper; ordinary by means of electrochemical deposition, this research project also investigated physical vapour deposition (sputter deposition). Afterwards they are treated similar to powder metallurgical fabrication using sintering, hot pressing or hot extrusion methods [32].
- *Liquid methods:* A few methods operate with liquid copper such as Vortex method, RF-melting, infiltration, pressure infiltration and squeeze casting [32].



The European Project (CAFICOM) was initiator for our investigations. The overall goal was the research of new production routines for copper carbon composites. The recent research-project focuses on the coating of fibers by various deposition techniques [32] in combination with a hot pressing step afterwards joining the fibers.

It quickly showed the weak bonding of copper onto carbon, which was forecast by several studies in the 70ies [33,34].

The dimension of carbon fibers (1-10 $\mu$ m thick, several 100 $\mu$ m long) complicates the basic research on coating. In our experiments flat substrates of vitreous carbon, a glassy modification of carbon, replaced the carbon fibers. This material is fabricated from non-saturated carbon compounds, carbonized at temperatures above 600 $^{\circ}$ C. Substrates used in our experiments were fabricated from HTW Hochttemperatur-Werkstoff GmbH, Germany under name of SIGRADUR<sup>®</sup> (detailed characteristics at [35]). In this modification carbon is believed to form a stable random network of graphitic ribbons (**Figure 1**). Compared with PITCH-fibre material it has a much lower density and thermal conductivity. Studies from Mortimer and Nicholas [33] state the comparability of studies focusing on wettability and diffusion mechanisms.

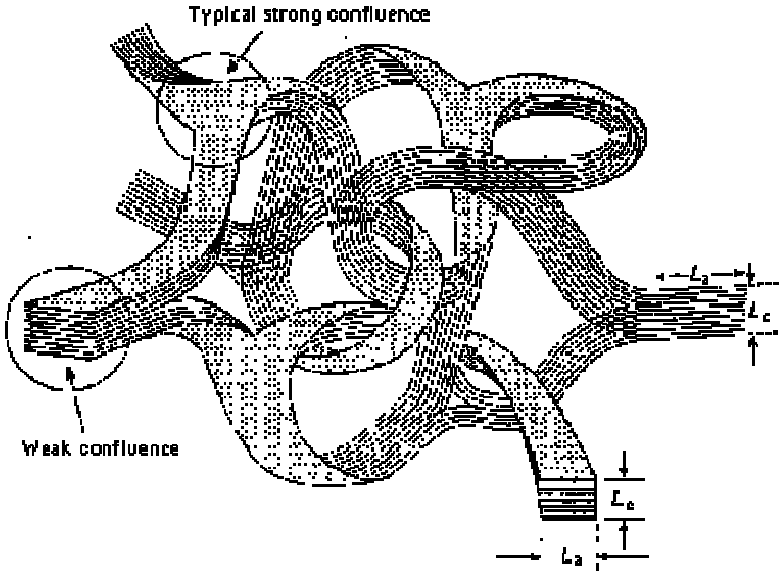


**Figure 1:** proposed model of the ribbon structure of glassy carbon

#### 4.1.1. Comparison of samples electrochemically and sputter deposited

In this approach 3 steps were intended for the material fabrication:

- Surface cleaning (of carbon fibers);
- Deposition of copper;
- Hot pressing.

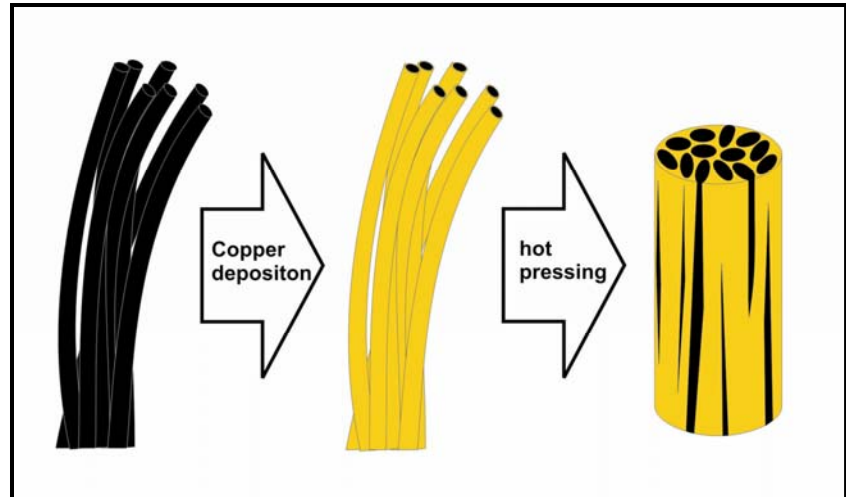


**Figure 2:** Scheme of the planed composite fabrication route.

Experiments in the laboratory benchmark focused at first the second (=deposition) step. For this purpose samples with different deposition techniques were made. In literature 3 techniques seem to be preferred: electrochemical deposition, evaporation and magnetron sputter deposition. Best wetting without further sample treatment (cleaning, etching, deposition of an interlayer) provided by far both physical vapour deposition techniques. Means of SIMS were firstly consulted, when differences in the layer quality became obvious using different deposition methods. Especially the adhesion strength of copper onto carbon varied when deposited electrochemically or by means of sputter deposition. Particularly Eisenmenger-Sittner et al [36] discovered, that PVD deposition is the much better bonding method. In our cooperation, sputter deposition was further investigated, but the first sample batch for SIMS measurements also consisted electrochemically deposited samples.

The first task for SIMS was to observe differences at the interfaces resulting from traces of additives (salts and stabilizer from the electrochemical deposition method) or from residual gas (PVD). In this behalf some samples were re-analyzed recording negative ion spectra with caesium primary ions. This first measurement was not published and it will be discussed more detailed therefore.

The first sample series consisted of some samples, where the deposition was done with physical vapour deposition (means of sputter deposition), and some where copper was deposited electrochemically (see table 2).

**Table 2:** sample description for samples used in chapters 4.1.1 and 4.1.2

No.	Substrate Cleaning Procedure	Chromium Inter-Layer	Copper Layer	Heat Treatment
A39	<i>Vapour phase cleaning (Ethanol)</i>	<i>non</i>		<i>non</i>
S105		<i>non</i>	<i>1.3μm ECD</i>	
B39		<i>non</i>	<i>1.0μm PVD</i>	<i>Heat treated for 1 hour at 800°C under vacuum</i>
B41		<i>10 nm</i>		
S79		<i>non</i>	<i>1.3μm ECD</i>	
S45		<i>10nm</i>		

In a first run mass spectra were done, to obtain information of the detectable ion species and their distribution. They were done from several samples at the surface as well as after sputtering into the carbon substrate.

Figure 3 shows a mass spectrum of the surface of a PVD deposited sample. Besides copper and some molecule-fragments also corrosion indicating elements like oxygen and sulphur, and contamination indicating electronegative elements chlorine and fluorine are visible. Latter two are most sensitive in SIMS using negative detection mode, and therefore detectable in almost all mass spectra. Nevertheless the qualitative distribution sometimes points out the presence of inorganic contaminants at the surface and within the layer. Most mass peaks are followed by a second smaller peak with one mass up, the  $MH^-$  signal. It is typical for spectra recorded without offset voltage. They are formed by collisions with hydrogen in the residual gas or with hydrogen-deposits at the surface. Interesting are the  $(Cu_2X)^-$  ions. Two species are more prominent against all others:  $(Cu_2OH)^-$  and  $(Cu_2O_2)^-$ . They point out an important

formation mechanism of bigger molecule ions: in the gaseous phase near or at the surface by collisions with residual gas molecules like H<sub>2</sub>O or O<sub>2</sub>. The O<sup>-</sup>/O<sub>2</sub><sup>-</sup> ratio shows the preferred formation of multi-atomic molecule ions in negative mode comparing with positive detection modes. In this special case, the O<sub>2</sub><sup>-</sup> signal tops the single atom ion O<sub>2</sub><sup>-</sup>, but also Cu<sub>2</sub><sup>-</sup> and Cu<sub>3</sub><sup>-</sup> are clearly visible.

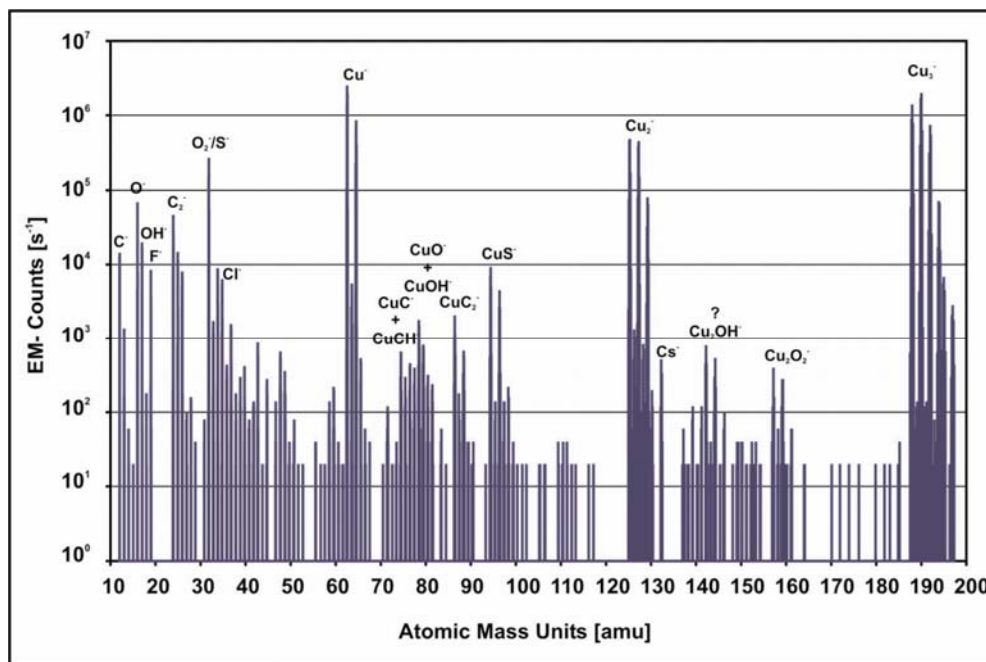
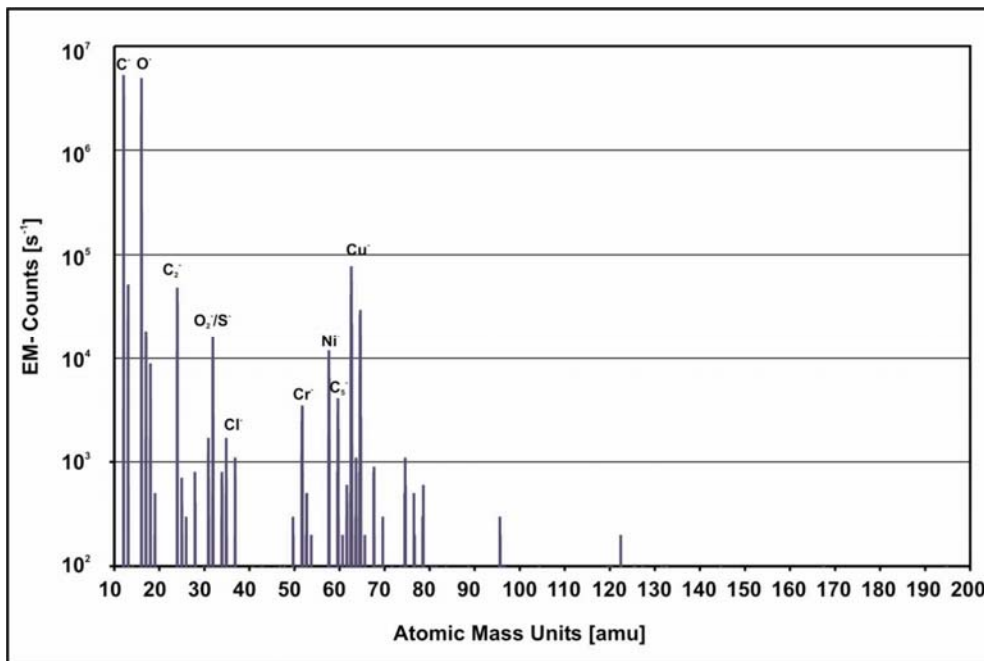


**Figure 3:** Mass spectrum of a physical vapour deposited sample at the surface (measurement consumption is app. 100nm); negative ion spectrum was done with 100nA Cs<sup>+</sup> primary ions, 15keV acceleration voltage.

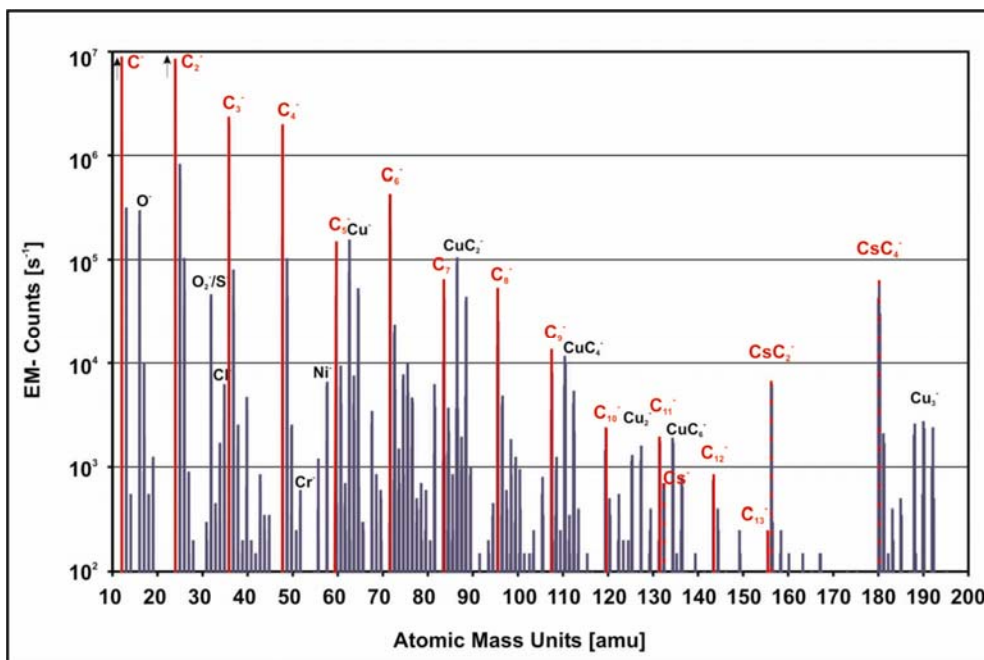
Completely different look has Figure 4, where offset voltage retards the detection of multi-atomic molecules using the different energy distribution of molecule- and atomic ions. Only fractions of C<sub>2</sub><sup>-</sup> and O<sub>2</sub><sup>-</sup> as well as of CH<sup>-</sup> and OH<sup>-</sup> are detectable. The drop of the atomic ion signals is not as strong; dynamic SIMS depth profiles mostly use this ability to prevent interferences with molecule ions.

Figure 5 shows the mass spectrum of the carbon substrate after sputtering without offset voltage. Most prominent in this spectrum are the multiple peaks of C<sub>n</sub><sup>-</sup> fragments (first 4 are at or near the detector limit and are not representing correct values). Measurements of pure carbon substrates often were topic of SIMS papers studying the formation mechanism and the energy distribution of secondary ions [37]. Besides C<sub>n</sub><sup>-</sup> ions (here n = 1...13) also fragments of CsC<sup>-</sup>, CsC<sub>2</sub><sup>-</sup> and CsC<sub>4</sub><sup>-</sup> are visible. Not visible is the ion CsC<sub>3</sub><sup>-</sup> (and all CsC<sub>2n+1</sub><sup>-</sup> ions, which is not shown in **Figure 5**). They are not forming stable ions or disintegrate during their flight to

the detector. Besides also residues of the upper metallic layers (Cu, Cr and in this layer also Ni) are visible; trace indicators fluorine and chlorine are weaker compared to Figure 3.



**Figure 4:** Mass spectrum of an electrochemical deposited sample near the surface (measurement consumption is app. 100nm); negative ion spectrum was done with 100nA  $\text{Cs}^+$  primary ions, 15keV acceleration voltage, 100V offset voltage.



**Figure 5:** Mass spectrum of an electrochemical deposited sample some 100nm below the interface. C-fragments have been red marked,  $\text{CsC}_n$  ions are red dashed; negative ion spectrum was done with 100nA  $\text{Cs}^+$  primary ions, 15keV acceleration voltage.

After investigating the mass spectra, the ions ( $^{12}\text{C}$ )<sup>-</sup>, ( $^{16}\text{O}$ )<sup>-</sup>, ( $^{16}\text{OH}$ )<sup>-</sup>, ( $^{19}\text{F}$ )<sup>-</sup>, ( $^{12}\text{C}^{14}\text{N}$ )<sup>-</sup>, ( $^{35}\text{Cl}$ )<sup>-</sup>, ( $^{52}\text{Cr}$ )<sup>-</sup>, ( $^{63}\text{Cu}$ )<sup>-</sup>, ( $^{63}\text{Cu}^{12}\text{C}$ )<sup>-</sup>, ( $^{63}\text{Cu}^{16}\text{O}$ )<sup>-</sup>, ( $^{12}\text{C}$ )<sub>8</sub><sup>-</sup>, ( $^{133}\text{Cs}$ )<sup>-</sup> were selected for depth profiling. Measuring negative secondary ions allows a sensitive detection of electronegative elements and molecules like Carbon, Oxygen, Fluorine, Chlorine, or the Cyanide (in some cases an indicator for nitrogen, which is directly not well detectable by means of SIMS). Commonly metallic and thus electropositive matrix elements are less sensitive in this mode, so only main components Copper, Chromium and the primary ion Caesium were detectable.

Figure 6 shows a depth profile of sample B39 (compare Table 2). From both main components only carbon signals (black line) show reasonably the distribution of this element whereas copper (grey line), plane in the copper layer itself, rises at the interface a factor 2. This merely demonstrates a matrix effect influencing all signals in the range of the interface. A comparison of the signal approach in the copper layer with the approach in the carbon layer does not make sense; the huge change of the matrix (both in composition and density) influences all signals drastically. For instance signals of the sputter atom caesium are almost absent in the copper layer, in the carbon layer they average 1600 counts/second, maybe pointing out an enrichment of caesium at the surface. Another striking fact is the warped depth scale. It will be reminded that the copper layer thickness of 1 $\mu\text{m}$  and the measured depth of 1.6 $\mu\text{m}$  (stylus method). This means, that the first 1 $\mu\text{m}$  is pictured by 130 cycles, and the remaining 170 cycles picture only 0.6 $\mu\text{m}$  carbon, what means a sputter velocity of 7.5  $\mu\text{m}/\text{cycle}$  within copper and 3.5  $\mu\text{m}/\text{cycle}$  within carbon. The immense change of density connected with a high porosity of the vitreous carbon substrate makes this indeed plausible. Concluding the interpretation at hand of a single depth profile is almost senseless, only in comparison to other depth profiles with similar matrices significant.

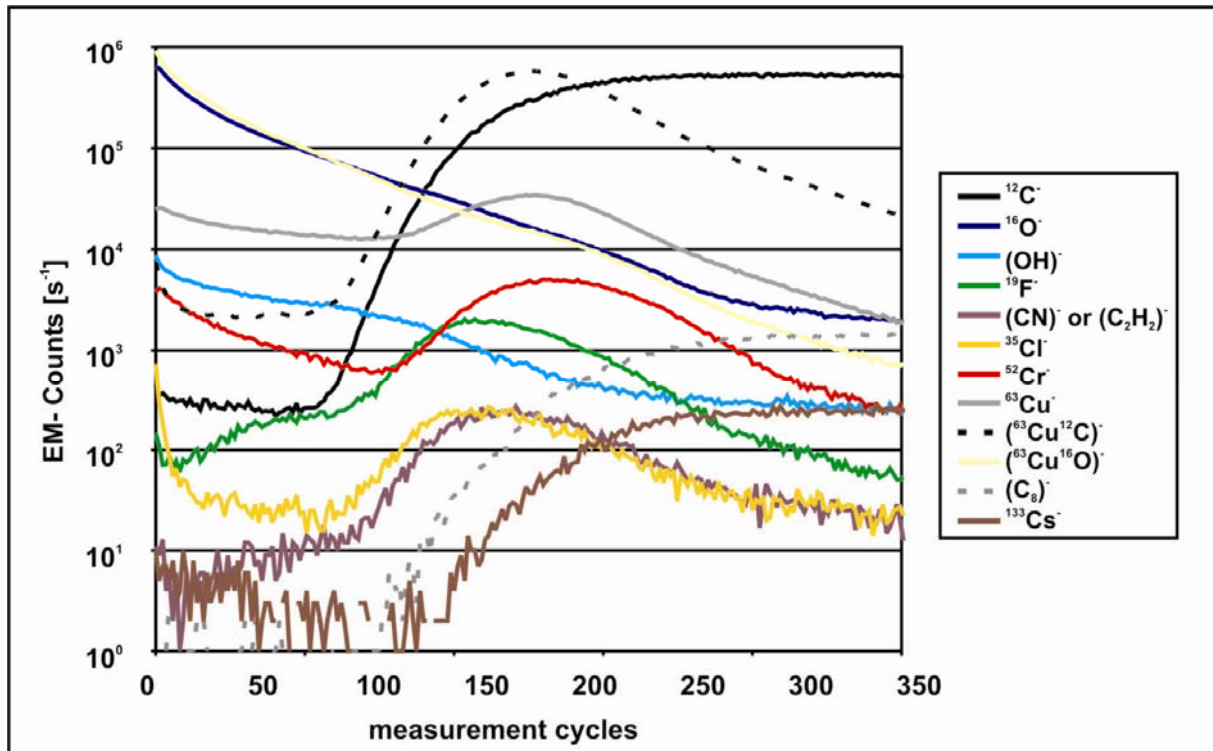


Figure 6: Depth profile of sample B41: 10nm Cr and 1 $\mu$ m Cu PVD-deposited onto vitreous carbon substrate subsequently heat treated for 1 hour at 800°C; Cs<sup>+</sup> primary Ions (30nA; 15keV acceleration); negative secondary ions; depth profile end at 1.6 $\mu$ m.

Figures 7 to 12 show a comparison of 4 depth profiles of samples B39, B41, S45 and S79 respectively. It shall clear the differences of PVD- and ECD-deposited samples and differences on the also displayed samples containing a chromium interlayer.

Each image displays the approach of a single mass in all 4 samples. The depth scale of the profiles is lightly adjusted (linear correction term to all cycle values of a depth profile) to match the interface position. This simplifies the comparison of ECD and PVD depth profiles (ECD copper layers are 1.2  $\mu$ m and 1.3  $\mu$ m thick, PVD copper layers are constant 1 $\mu$ m thick, see Table 2). Additionally also the signal heights are adjusted in order to roughly match the signal heights of <sup>63</sup>Cu<sup>-</sup> in the copper layer and <sup>12</sup>C<sup>-</sup> in the carbon layer respectively.

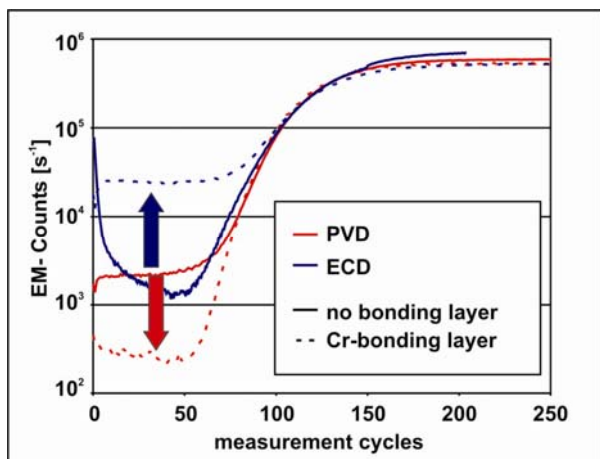


Figure 7: Mass 12 ( $^{12}\text{C}$ ) of depth profiles of samples B39, B41, S79, S45 (see also Table 2) with  $1\mu\text{m}$  Cu layer deposited onto vitreous carbon substrate; (Cr-bonding layer thickness 10nm);  
PVD=physical vapour deposition;  
ECD= electrochemical deposition.

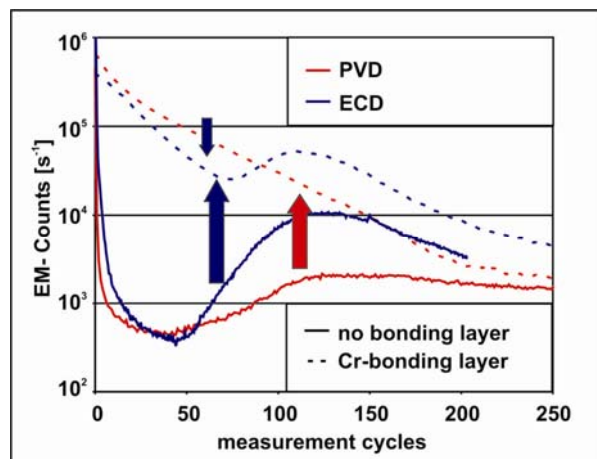


Figure 8: Mass 16 ( $^{16}\text{O}$ ) out of 4 depth profiles (see description of Figure 7).

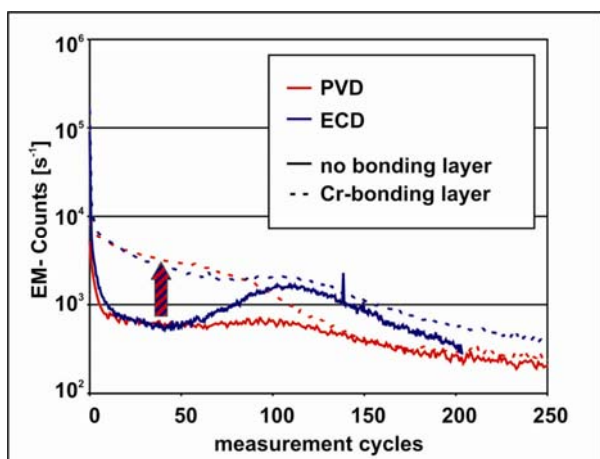


Figure 9: Mass 17 ( $\text{OH}$ ) out of 4 depth profiles (see description of Figure 7).

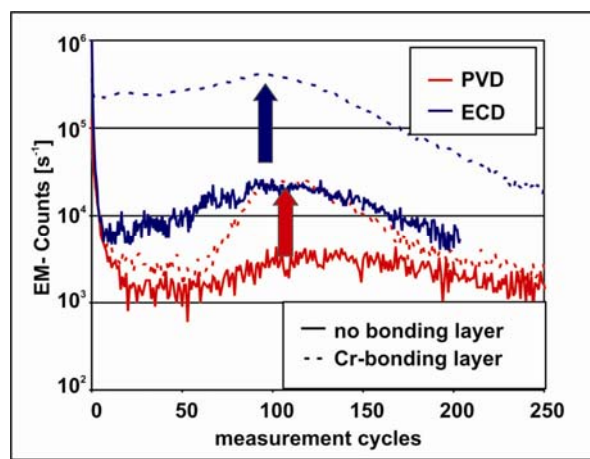


Figure 10: Mass 35 ( $^{35}\text{Cl}$ ) out of 4 depth profiles (see description of Figure 7).

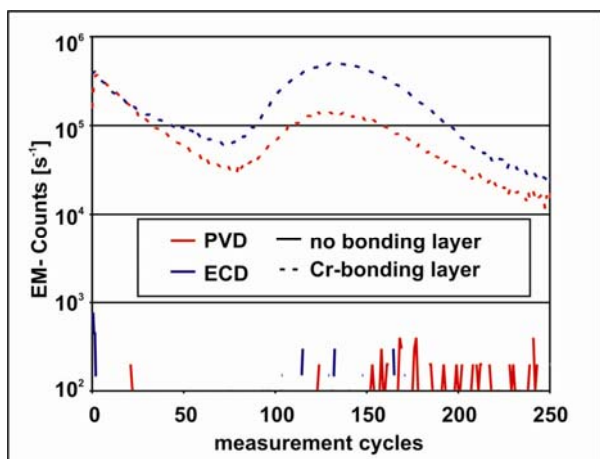


Figure 11: Mass 52 ( $^{52}\text{Cr}$ ) out of 4 depth profiles (see description of Figure 7).

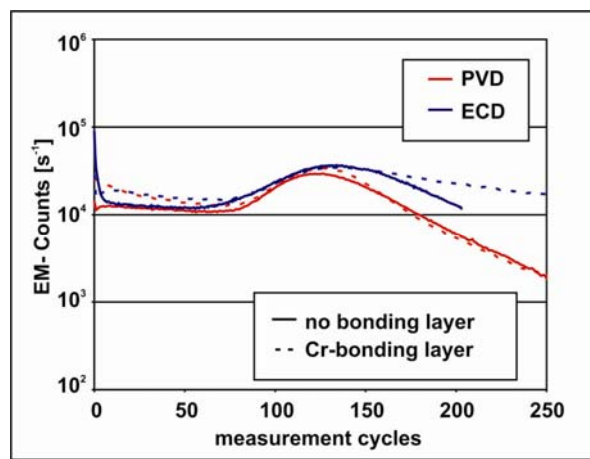


Figure 12: Mass 63 ( $^{63}\text{Cu}$ ) out of 4 depth profiles (see description of Figure 7).



Figure 7 shows the approach of mass 12, which belongs to  $^{12}\text{C}$ . In all samples the carbon signal levels in the carbon layer (right side of each image) due to referring the signal heights onto this mass. In the copper layer signals of this mass diverge. In samples without chromium interlayer (solid lines) it almost levels in the PVD sample whereas drops lightly down from the surface in the ECD-sample. This may point to a surface contamination during or after fabrication diffusing into the layer after temperature treatment when ECD deposited (compare with sample fabrication description in Table 2). Much more astonishing seems the difference of samples with chromium intermediate layer. In the PVD deposited sample it is one order of magnitude below the signal of both samples without chromium. But in the ECD-deposited sample it is one order of magnitude above both samples without chromium. Two circumstances may cause this result: A higher concentration of carbon in copper (only plausible in combination with the presence of other carbon fixing elements) or pinholes in the copper layer (due to the crusted surface morphology a very likely reason).

Figure 8 shows the distribution of oxygen. Yet the comparison of ECD and PVD-samples without chromium reveals an increase of oxygen in the interface region. Those samples with chromium interlayer contain much more oxygen. The signal starts very high and drops down more than two powers of magnitude within the copper layer. Interesting is the difference of both chromium consisting layers, almost mirroring the approach of the chromium-less layers onto the slope, meaning that in this samples as well is oxygen lightly enriched at the interface as seen without chromium.

Figure 9 shows signals of the molecule ion  $\text{OH}^-$ . Sometimes this signal figures out the hydrogen distribution, but due to the complex changes in the oxygen concentration itself, it is mostly mirroring the oxygen distribution seen in figure 8.

Figure 10 displays signals of mass 35 ( $^{35}\text{Cl}^-$ ). There is more chlorine in both ECD samples, especially in the chromium containing sample. Chlorine is a tracer for contamination both at the surface and the interface respectively. Therefore all displayed differences may occur also from grains situated at the surface. If these grains are bigger than the copper layer, they may feign a homogeneous chlorine contamination of the sample. Additionally there is a more or less significant enrichment of chlorine in the interface region.

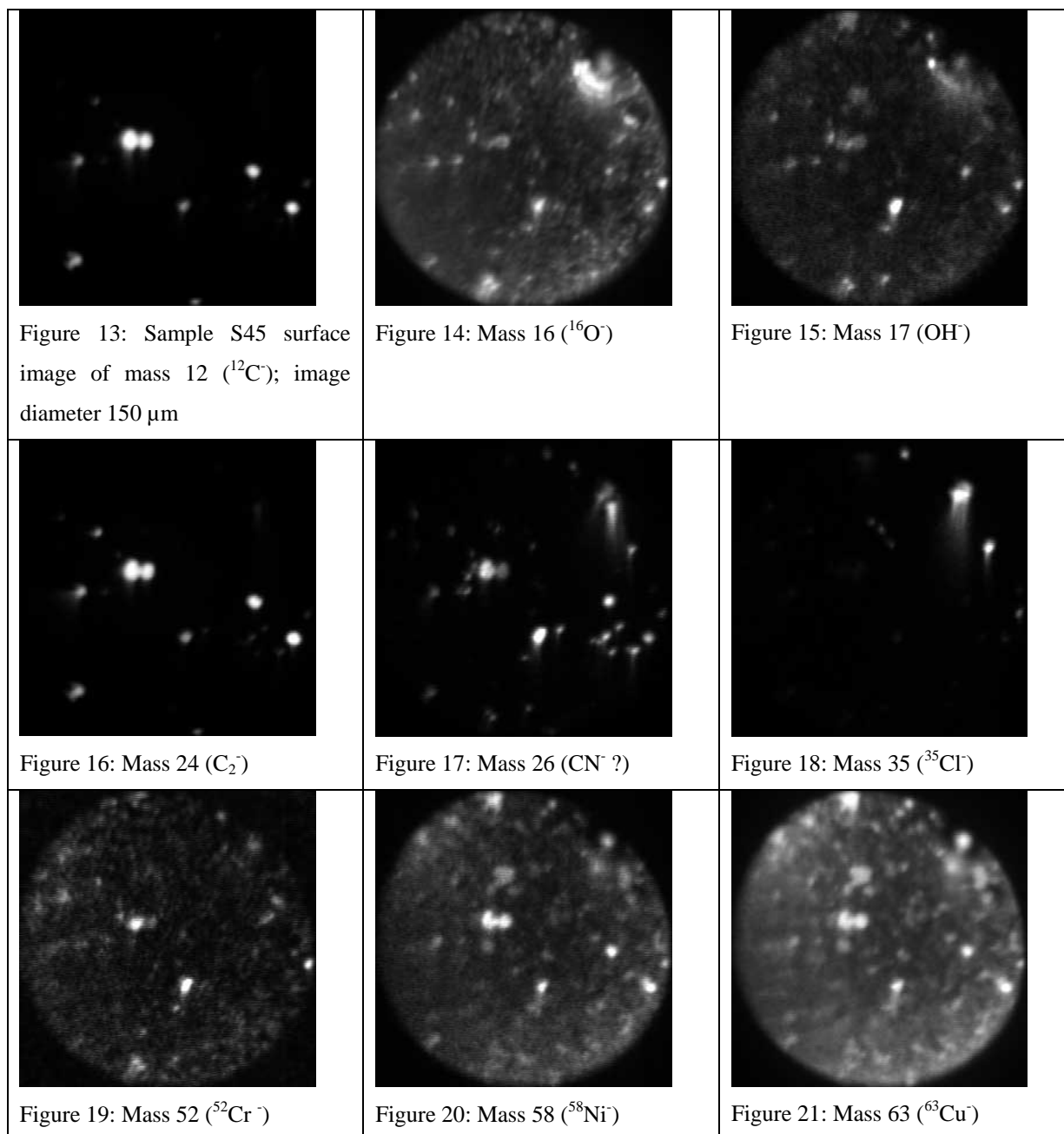
Figure 11 shows the chromium distribution. Due to only samples B41 and S45 contain chromium, it is only visible within this samples. But these two signals are indeed very interesting. The chromium layer thickness is about 10nm, this is at the limit of the depth resolution of the used SIMS device. Nevertheless, in both layers the chromium layer shows up broadened to approximate 1  $\mu\text{m}$  layer thickness. Additionally a major part of chromium has

gone to the surface region. Once more mentioning the oxygen distribution in figure 8, this may point to a diffusion of chromium onto the surface in combination with a fixation by oxidation. The signal height difference in the interface region may not only display a concentration difference there, this may also be caused by a matrix effect of the different oxygen concentration at the interface or by lightly different layer thicknesses.

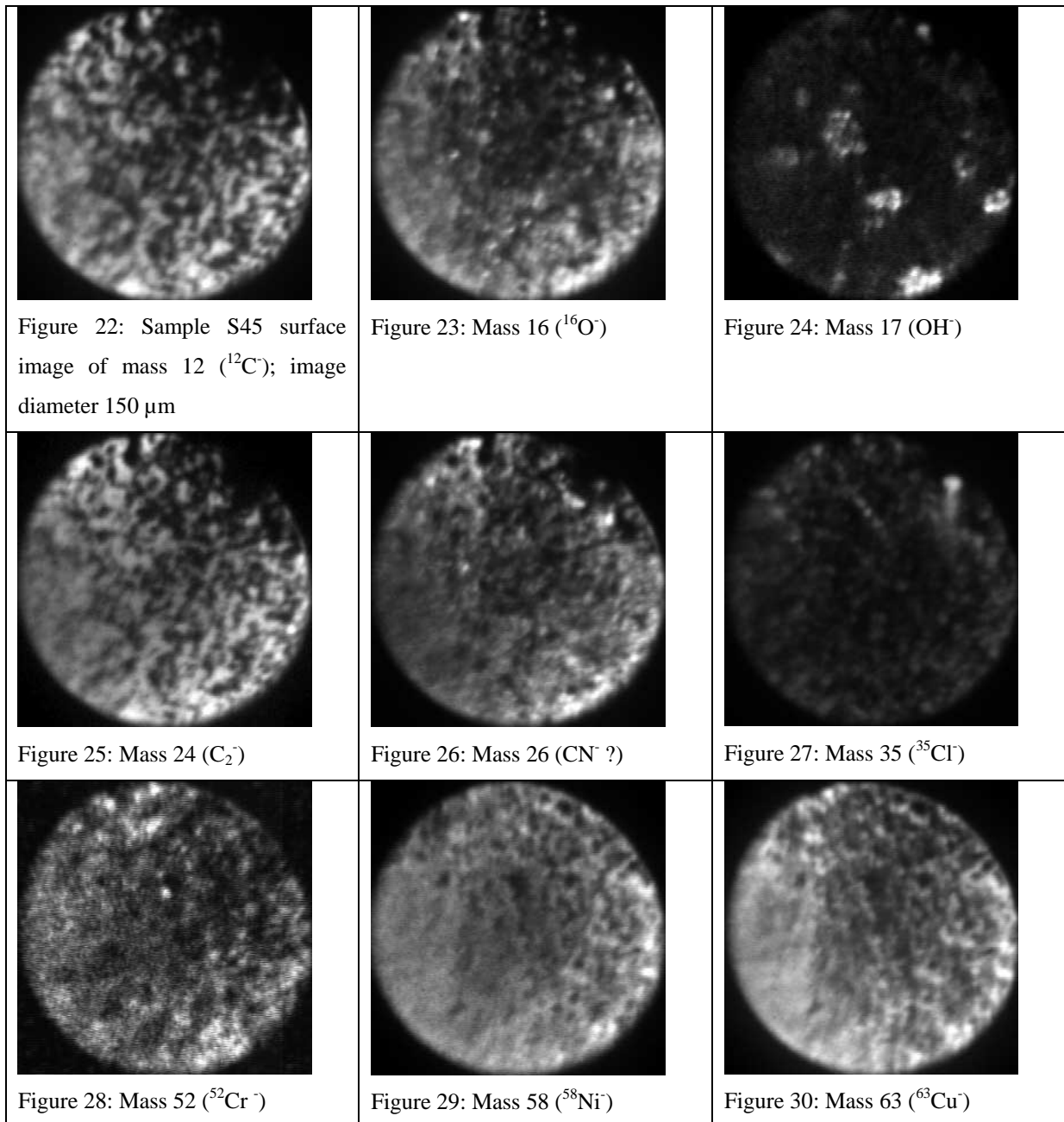
Remains figure 12. It shows the distribution of copper. As mentioned above, all signals may be influenced by a matrix effect at the interface. Nevertheless, all signals equal until reaching the carbon substrate. There signals of the PVD-samples drop visibly faster than those of ECD-layers. Sample S79 (without chromium) has a definitively broadened interface and in sample S45 (with chromium) also the slope of the signals is smoother. Both effects may also be caused by a surface roughening proceeding maintaining during sputtering. This manifests especially in sample S45, which also showed clues of surface roughening at other masses.

Figures 13 to 30 show channel plate images from sample 45 which were done on this behalf. There are 2 series displayed, first (figures 13 to 21) shows the lateral distribution at the surface, the other (figures 22 to 30) is are shots from the interface region of this sample.

At the surface several elements are spotty distributed. Particularly carbon (Figures 13 and 16), oxygen (figure 14) and chlorine (figure 18) are enriched at some spots at the surface and each element has its own distribution. Carbon ordinary can be tracked down to soot, chlorine to salty residues, oxygen normally to inorganic abrasion particles (silicates, carbonates...). Oxygen additionally shows a "homogeneous" background (perturbed due to topography and matrix effects), displaying the natural oxygenated surface layer. An as well spotty image shows (CN)<sup>-</sup> (figure 17), but its distribution is alike carbon with some additional spots at the right part of the picture. Whether this is a true mapping of nitrogen or not, is not clearly statable. Figure 15 shows an image of mass 17 (OH<sup>-</sup>). It merely displays the oxygen distribution, but with shifts in the intensity at some spots. The images of the metal ions Cr<sup>-</sup>, Ni<sup>-</sup> and Cu<sup>-</sup> are shown in figures 19 to 21. In all these images a dependency on the carbon and also oxygen distribution is visible. This shows the big influence of the matrix composition on the signals intensity, especially when recording images. Other than depth profiling are images ordinary captured without offset, thus allowing molecule ions to superpose atomic ions. Additionally the topography is influencing the signals lateral distribution enormously, especially when detecting negative ions.



On the following page images of the interface region of sample S45 are displayed. Most masses signals are even distributed (considering the topography influences on the signal distribution). Shaded areas especially in figures 22, 23, 25 and 26 are due to bad adjustment of the secondary magnet and are not linked up with the elemental distribution in this area. Only at mass 17 ( $\text{OH}^-$ ; figure 24) is differing from all others! Maybe this is a clue on water or just hydroxyl- inclusions at this area remaining from electrochemical deposition?



As a matter of fact, SIMS was able to show differences, but was not able to give hints enhancing the machining routines of the subjected material.

Besides SIMS measurements, simple adhesion tests, done at the Institute of Solid State Physics (data were not published), revealed the much better adhesion strength of sputter deposited samples in comparison to electrochemical deposition. Nevertheless after the heat treatment (simulating the later serial hot pressing step) the adhesion strength drops down a power of magnitude. A comparison of samples with and without thermal treatment was the next subsequently following task for SIMS.

#### 4.1.2. Comparison of samples as deposited and heat treated

In table 2 also samples can be found, giving the ability of a comparison of samples with and without heat treatment. Samples A39 and B39 were deposited in a single run; and only B39 was further processed by a heat treatment for 1 hour at 800°C. Similar there is a sample pair with the electrochemically deposited samples, samples S105 and S79. Unfortunately these samples were not measured one SIMS run. This complicates the compatibility of the samples.

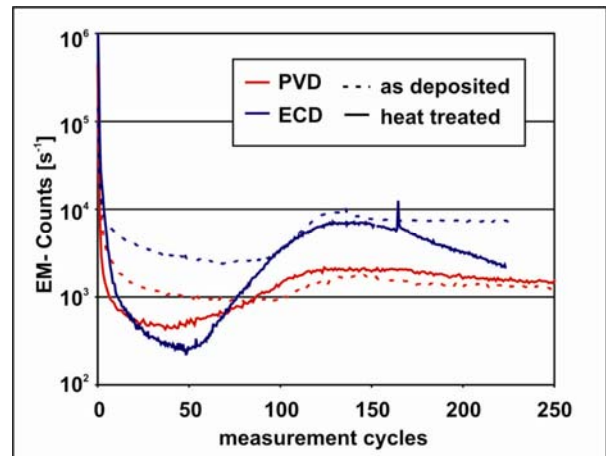
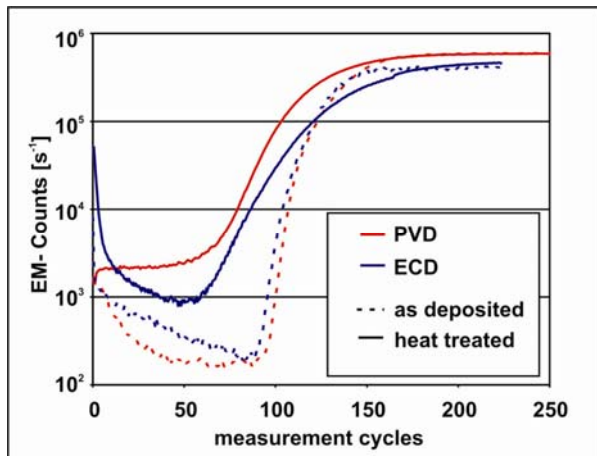


Figure 31: Mass 12 ( $^{12}\text{C}$ ) of depth profiles of samples A39, B39, S105, S79 (see also Table 2) with  $1\mu\text{m}$  Cu layer deposited onto vitreous carbon substrate; PVD=physical vapour deposition (vaporization); ECD= electrochemical deposition.

Figure 32: Mass 16 ( $^{16}\text{O}$ )

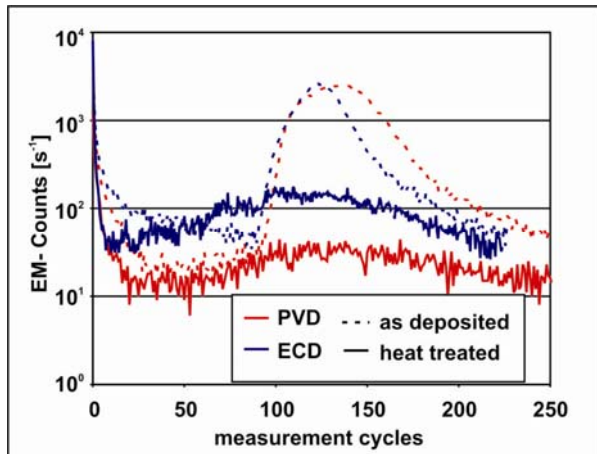


Figure 33: Mass 35 ( $^{35}\text{Cl}$ )

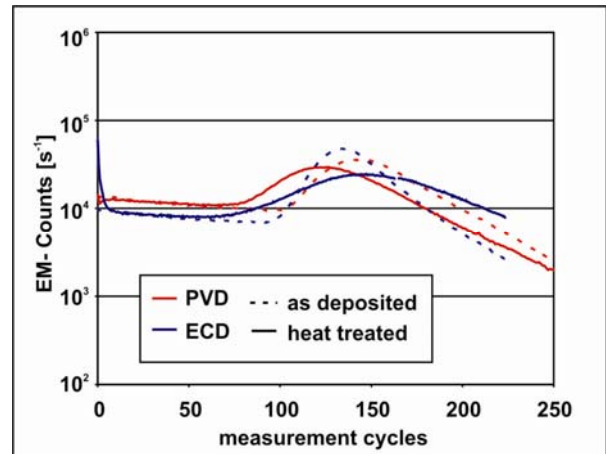


Figure 34: Mass 63 ( $^{63}\text{Cu}$ )

There are some interesting features in the compilation of figures 31 to 34. The **carbon** content in copper rises lightly, and in both samples “as deposited” declines from the surface visibly. Another feature is the **broadened interface** of both heat treated samples. It is a hint on a roughening both of the surface and the interface! **Oxygen** (figure 32) is increased at the interface as seen in the PVD-ECD comparison (figure 8); in copper it drops almost an order of magnitude after heat treatment! Interesting are the changes of **chlorine** (figure 33). In both samples “as deposited” a broad chlorine peak is positioned at the interface, which fades during heat treatment; maybe chlorine is outgassing in the form of HCl. **Copper** (figure 34) is not changing substantially, only the interface broadening seen with carbon is also visible with this signal.

#### 4.1.3. Hydrogen and nitrogen plasma pre-treated samples

Bonding copper onto glassy carbon substrates is a complex task. Due to the low wettability of pure copper onto glassy carbon substrates [33] an adhesion strengthening pre-treatment seems necessary. Additionally the task is complicated by the hot pressing step. A particularly improvement of the adhesion strength, achieved with plasma pre-treatment of the surface [38], is limited to not thermal treated samples. After heat treatment, the adhesion strength again drops to initial values comparable to non plasma treated samples. In [39] the effects of nitrogen plasma pre-treatment were investigated with means of SIMS. A non published work within this PhD thesis focused on the comparison of nitrogen and hydrogen pre-treatment.

**table 3:** sample description for plasma pre-treatment experiments; all samples were introduced with ethanol-cleaned surface, plasma etching took 30 seconds, subsequently 300 nm copper was deposited.

	SN	S3:1	S1:1	S1:3	SH
N <sub>2</sub> pressure	4 Pa	3 Pa	2 Pa	1 Pa	-
H <sub>2</sub> pressure	-	1 Pa	2 Pa	3 Pa	4 Pa

All samples consists of glassy carbon substrates (SIGRADUR G [35]), as used in previous studies. Surfaces were liquid cleaned (degreased by ultrasonic cleaning in acetone and ethanol followed by vapour phase cleaning in Ethanol vapour and then stored at 80°C until being inserted in the deposition chamber to guarantee a dry surface). After inserting the substrates into the sputter deposition device (ALCATEL SMC450 magnetron sputter device, device

parameters in [40]), they were evacuated to  $10^{-4}$  Pa. Argon with 4 Pa pressure was filled into the device and an arc plasma ignited.

To realize reactive plasma cleaning argon plasma was subsequently replaced by nitrogen (**sample SN**) or hydrogen (**sample SH**) or mixtures of these gases as described in table 3. Both gas streams were monitored by rotameters. The procedure from plasma ignition to steady sputter condition took only several seconds. After 60 seconds constant sputter cleaning all gas streams were turned off and the device pumped down to  $10^{-4}$  Pa and wait for 1 minute. Then the device polarity was reversed, argon was filled in again (4 Pa), plasma ignited and 300nm copper was deposited. At least one slice of each sample was heat treated for 1 hour at 800°C. Of some samples as deposited and heat treated respectively pull off tests were done, showing the adhesion strength of these layers (compare figure 35). Without heat treatment the pure nitrogen treated sample has the maximum adhesion, whereas with a heat treatment the maximum is at the sample S3:1 (Nitrogen / Hydrogen - 3:1).

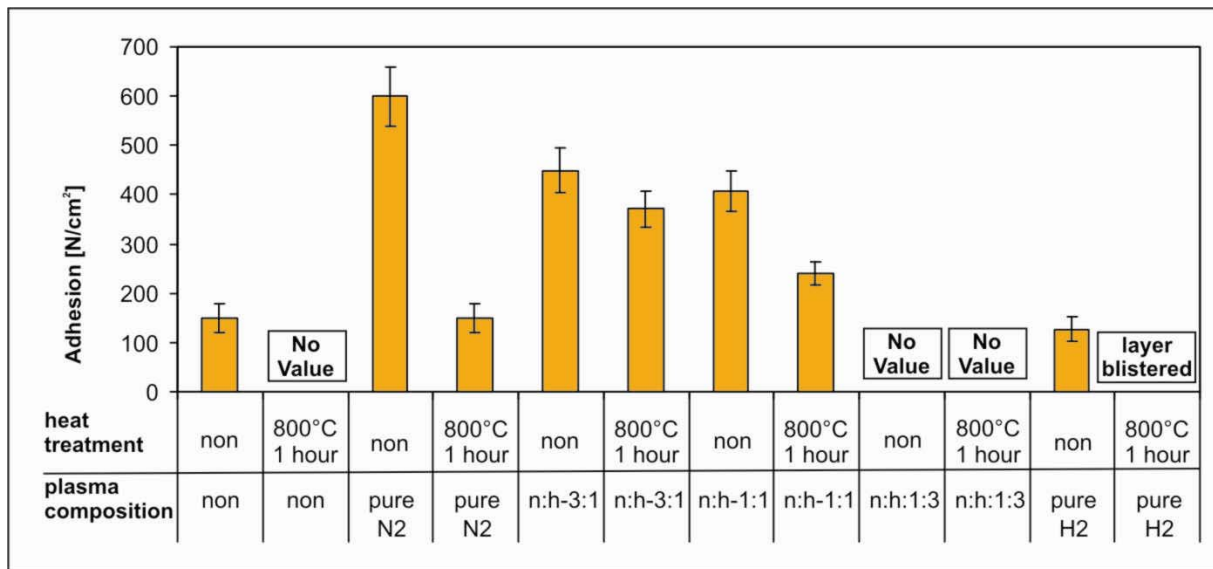


Figure 35: Results of adhesion tests of samples of the nitrogen/hydrogen sample batch.

With SIMS we wanted to take a look at changes in the chemical composition explaining such a result.

Monitoring nitrogen is a tough task for SIMS due to it is the least sensitive element. Only analyzing  $MCs^+$  ions allows a view on the distribution of this element. This method was already used in [39] from a college, but different from these studies data of this comparison were very ambiguous.

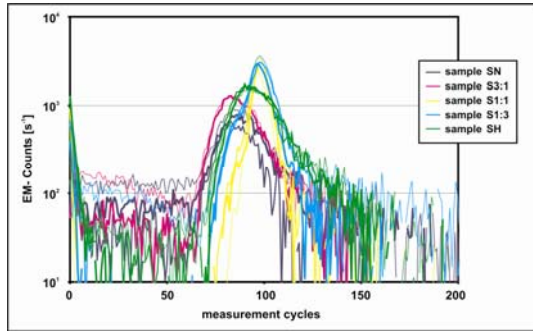


Figure 36: Hydrogen

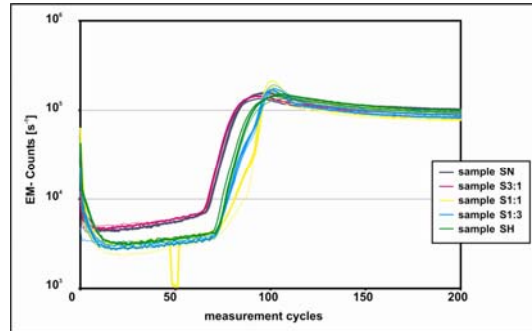


Figure 37: Carbon

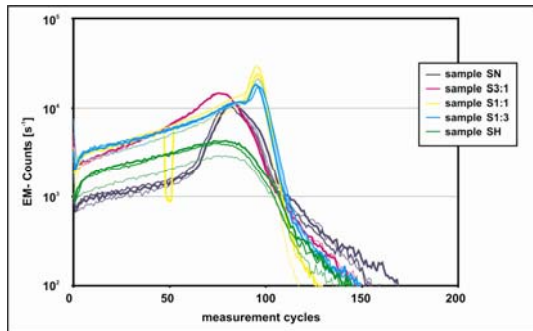


Figure 38: Nitrogen

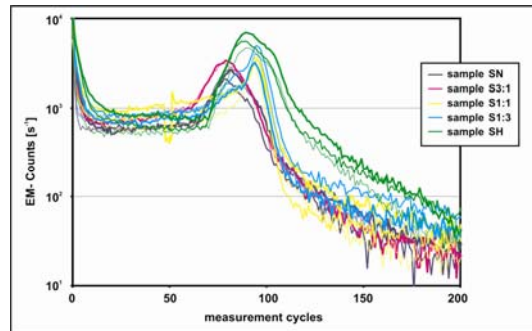


Figure 39: Oxygen

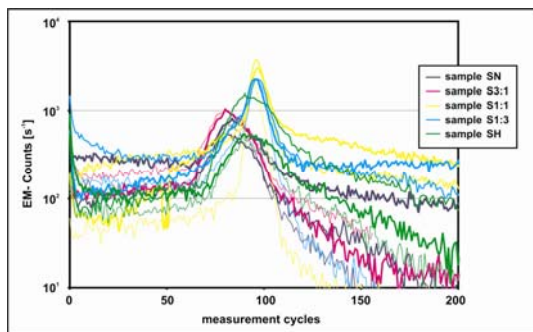


Figure 40: Aluminium

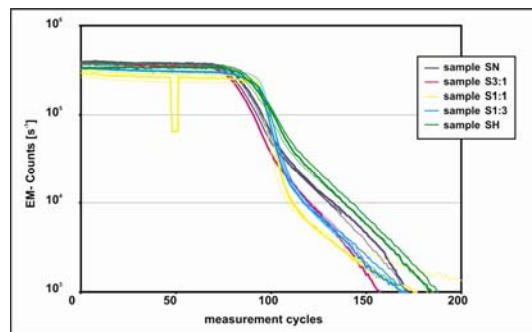


Figure 41: copper

Due to the curve shape of the signals 2 types of samples are distinguishable: The first group consists of samples SN, S3:1 and SH, a second group S1:1 and S1:3. The most striking difference is the peak breadth at the interface, in the first group very broadened, in group 2 narrow. Usually is a broad interface a clue for rough surface or interface, respectively. According to [41] the surface becomes rougher when the sample gets heat treated. This would mean that 3 samples of this research are heat treated, whereas the other 2 are not. This is not consistent with the sample description, but this uncertainty limits the value of this research. Nevertheless, edging samples SN and SH are easily comparable. As expected there is more hydrogen in sample SH and more nitrogen in sample SN. Additionally there is less carbon in the copper layer of sample SH. It is not definite weather this is a hydrogen influence or a simple measurement artefact, although all samples were measured at least 3 times and the



reproducibility seemed very good for technical samples. Another element showing differences is oxygen; the signal is in sample SH at the interface almost a power of magnitude above sample SN. As seen with the  $\text{CsAl}^+$  signal most trace element signals have a wider statistical spread in their concentration.

#### 4.1.4. Chromium intermediate layers

Another chance strengthening the Cu-C adhesion is alloying copper with trace elements. From literature especially chromium, vanadium [41] and titanium [42] respectively are suggested. In our research project sputter deposition was the preferred method of choice. One of its advantages is the capability of depositing thin films in a wide range of thickness; from several nanometers up to several tens of micrometers. So besides co-depositing alloys, we had the chance to deposit intermediate layers. It was intended to enhance the adhesion strength in this way and make it able for enduring a heat treatment. In this behalf samples with chromium, titanium, vanadium and also molybdenum intermediate layers were prepared. Our research at first focused chromium, due to in prior investigations [41, 42] best results were achieved this element.

Basis for SIMS investigations was sample B41 from the batch described in table 2 (chapter 4.1.1). Besides a layer of 1  $\mu\text{m}$  copper it consisted of a layer of 10 nm chromium beforehand deposited onto vitreous carbon. Figure 6 shows a first depth profile of this sample. Interesting was the decline of the chromium signal in this sample. Much more prominent was the decline in samples with thinner chromium layers and also when using  $\text{O}_2^+$  primary ions instead of  $\text{Cs}^+$  together with detecting positive secondary ions.

This was also reported in a publication (see also **Chapter 5.1: Characterization of Cr intermediate layers in Cu-C-system with SIMS method**)!

This study first revealed the problem of correlating a depth measure to the SIMS depth profiles. Yet in sputter simulations (in this publication TRIM [43] was used) carbon and copper diverge massively in their sputter rate. These simulations are not able to consider the lower density of vitreous carbon sufficiently, and only allow input of estimated values of the surface composition. Especially the primary ion input (concentration of Cs or oxygen respectively) and the surface amorphization by the milling primary ion beam is not considered well. A second possible way is the estimation by measuring the crater depth of pure element depth profiles. These measurements revealed a much lower sputter rate in carbon compared

with copper (the sputter rate of chromium was not considered due to the low layer thickness); in copper 0.36 nm/second and for carbon 0.16 nm/second respectively were found for the chosen measurement parameters. The sputter rate at the interface was adjusted by comparing the SIMS signals ( $\text{Cu}^+$  vs.  $\text{C}^+$ ) and calculating a transition zone.

This investigation revealed the chromium diffusion to the surface. The samples were also investigated with 3D-depth profiles, where Chromium at the surface was even distributed, whereas at the interface enriched at some spots. Latter impression was intensified by the rough surface/interface (not well detectable with SIMS) visible with copper.

This is leading to a second publication more detailed focusing on the chromium diffusion. Samples without, with 2 nm, 10 nm, 25 nm and 50 nm chromium interlayer respectively were investigated (additionally some samples from chapter 4.1.1 were described). The core part of this paper was a comparison of the chromium at the surface and the interface. It was done by summing up the chromium signals from the surface to a signal minimum between those two layers ( $r_{\min}$ ) respectively from this minimum until the measurement end ( $r_{\max}$ ). Shifting these margins only causes minimal error due to the logarithmic scale of the depth profiles signals. This analysis firstly was originally a poster presentation at the “International Conference On Metallurgical Coatings And Thin Films” San Diego, USA (30.4. - 4.5. 2001), later also paper published (see **Chapter 5.2: Adhesion promotion of Cu on C by Cr intermediate layers investigated by the SIMS method**). This investigation revealed a dependency of the initial chromium layer thickness on the diffusion. There was a minimum of the diffusion at the 10 nm and the 25 nm layers, where the distribution of chromium at the interface and the surface was almost 2.5:1. This matches almost with pull off tests of these samples showing a maximum adhesion after heat treatment at the 10nm sample. With lower layer thickness the chromium diffusion rises probably due to the lowered oxide layer enhancing the diffusion whereas with raising layer thickness the interface layer destabilizes and therefore diffusion is enhanced.

A parallel investigation [41] focuses the surface situation using means of Atomic Force Microscopy and Auger Electron Spectroscopy. AFM was able to observe characteristic roughening of the surface during heat treatment in the micrometer range (in later papers this effect was reported to be independent on the chromium concentration and also occurring without chromium). AES investigated the element distribution at the surface and within a depth profile of the first few nm (about 25 nm  $\text{Ar}^+$  sputter abrasion), which revealed a distribution similar to SIMS investigations. More evident than SIMS analysis it shows

chromium to form oxides at the surface rather than carbides. Unfortunately the depth profile did not reach the interface; no statement on this region was possible.

#### 4.1.5. Molybdenum intermediate layers

The weak adhesion and the diffusion tendency of chromium suggested the use of different elements as adhesion promoters. In [44] titanium was tested, [41] and [45] investigated molybdenum interlayer, not published yet are investigations with vanadium.

Best results were achieved with molybdenum, which maintained the adhesion enhancement of a factor 7 also after heat treatment compared with samples without further surface pre-treatment.

Two studies also contain SIMS results. In both studies  $MCs^+$  ions were analyzed, which turned out to be less influenced by the matrix effect than measuring atomic positive or negative secondary ions as used in previous studies. This was necessary to compare signals of several elements in the copper- molybdenum and carbon layer respectively. Additionally in this mode nitrogen is most sensitive and also oxygen is sufficiently detectable.

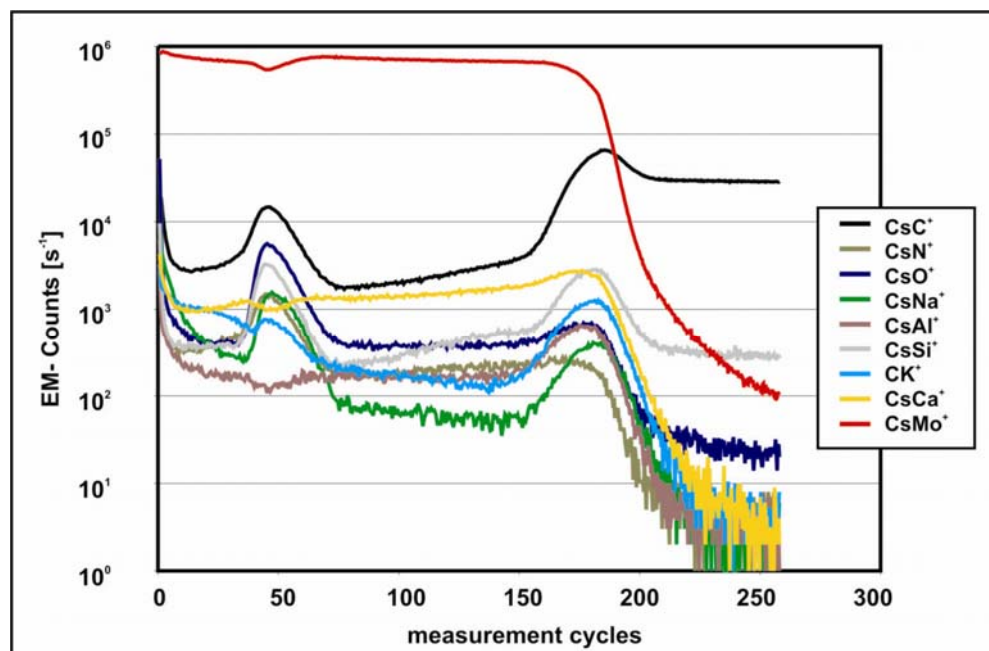
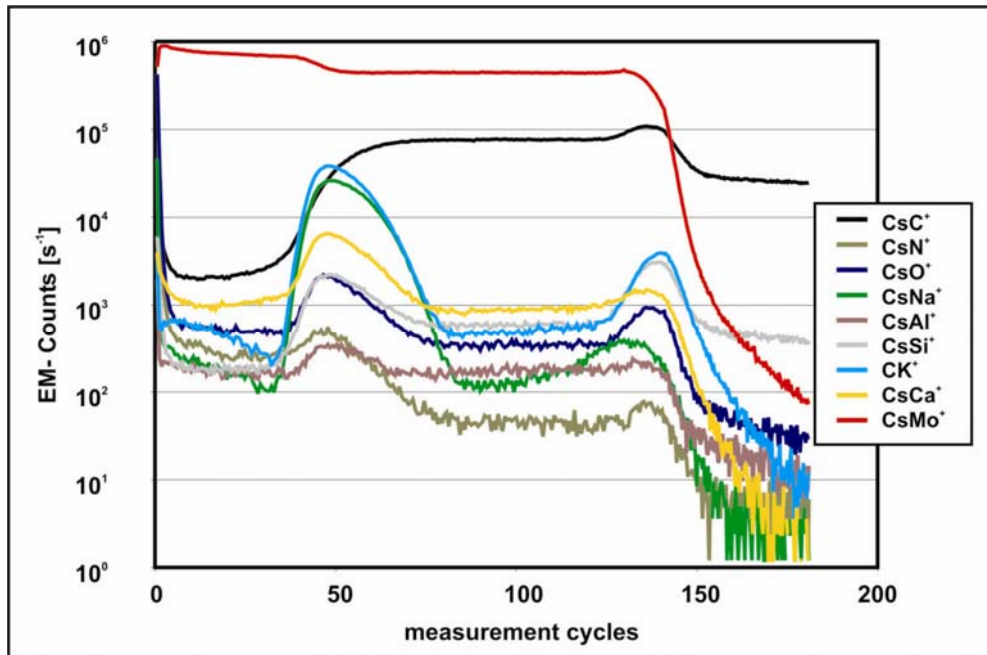


Figure 42: Depth profile of a Mo/MoC/C sample (layer sequence seen from right to left in order of sputter ablation); 500 nm Mo sputter deposited onto carbon, after a few weeks again 300 nm Mo sputter deposited; SIMS measurements with  $Cs^+$  primary ions (30 nA), analyzed 150  $\mu m$  circular area, positive secondary ions.



**Figure 43:** Depth profile of a Mo/MoC/C sample (layer sequence seen from right to left in order of sputter ablation); 300 nm Mo sputter deposited onto carbon, then heat treated at 800°C for 1 hour, then again 300 nm Mo sputter deposited; SIMS measurements with Cs<sup>+</sup> primary ions (30 nA), analyzed 150 μm circular area, positive secondary ions.

The first SIMS study (see **chapter 5.4, Characterization of molybdenum intermediate layers in Cu-C system with SIMS method**) focuses on a comparison of samples with and without heat treatment. Compared with chromium samples the molybdenum layer was much thicker. This was done to ease SIMS depth profile analysis; doing this with chromium was not possible because thicker chromium layer (>50nm) always tended to blister.

Like chromium huge changes in the composition and distribution of the elements were found with molybdenum. Most important is the formation of Molybdenum carbide during heat treatment. Although the formation of a chemical bond is not verifiable with SIMS, but two major clues suggest it: The presence of the two named elements in the new formed layer and studies [46,47] at similar systems verified with XPS, which investigate the diffusion velocity from carbon in molybdenum at 800° - 1000° and resulted in a much higher velocity than necessary for our system. Especially for SIMS measurements manufactured samples with a molybdenum cap layer instead of copper, which was deposited after heat treatment, showed best the changes within the heat treated molybdenum layer. Due to the lower cap layer thickness, it was possible to reduce the sputter velocity and resolve lower molybdenum layer before and after heat treatment. The use of molybdenum as cap layer also reduced the interface effect like seen with copper-molybdenum interfaces.

In the sample “as deposited” there is a minor increase of carbon towards the carbon substrate visible, it may point to a diffusion during the deposition (the surface heats during sputter deposition, also simple mixing effects may be important). Still the signal is obviously connected with a huge matrix effect; the  $\text{CsC}^+$  signal in the MoC-layer exceeds the signal in the carbon layer (here probably also the different sputter coefficient is important for this effect).

The signal  $\text{CsN}^+$  drops in the MoC-layer of heat treated sample. An equal effect as seen in older measurements with chlorine, purifying the layer by outgassing, may effect this (compare with figure 33).

Differences are also visible with the alkaline and earth alkaline elements (most prominent sodium and calcium) at the Mo/MoC interface. This is mainly caused by the sample handling between first and second molybdenum deposition (including the heat treatment).

A last remarkable point was the interface broadening in depth profiles of the copper/molybdenum sample after heat treatment seen most prominent with the molybdenum signal. This can be attributed to the surface roughening effect, seen with AFM (compare with [41]).

The second publication subjecting molybdenum interlayer (**Influence of thermal treatment on the adhesion of copper coatings on carbon substrates**, see **chapter 5.3**) is a summary on all recent investigations including a SIMS comparison of two samples. Other than previous described samples, they were additionally  $\text{N}_2$ -plasma pre-treated, one sample as deposited, on after heat treatment. The results were comparable to the first molybdenum publication.

## 4.2. Investigations on Corrosion of golden coins and medals

This task is done in cooperation with the “Kunsthistorisches Museum Vienna” [48]. Origin of this project was a restructuring of the exhibition of the coin cabinet [49] in 1998, a museum sub-collection including over 100.000 objects, mostly coins, medals and orders from over 3.000 years. Together with this rearrangement parts of the collection were newly sifted and inventoried.

Also the state of the preservation was detected on all these objects. Due to the multitude of samples and the complex task, this took several years. During this procedure several hundred gold coins were found with partly corroded surface. Corrosion is a widely known phenomenon in numismatic, affecting all materials – except gold!

About the same time the “Austrian mint” [50] started a research project on a similar task. Sometimes the minted gold coins (ducats, guldens ...) were covered with tiny black spots in the sub-millimeter range. Although the computer-aided quality control rejects most of these coins, the fact that there are failing products initialized a research project, quickly merging with the “Kunsthistorisches Museum Vienna” task to a museum-industry cooperation.

A first research with electron microscopy [51] revealed residuals of foreign metals at the surface, mostly silver and copper. In the Austrian mint they were mostly coming from dust from other machines (although the production line of each metal is strictly separated), whereas the corrosion on coins of the Kunsthistorisches Museum mostly were results of using same tools for different metals (e.g. minting copper, silver, and gold medals with same dies). Additional Auger electron images of the surface, presented in [52], revealed also the presence of sulphur at these spots.

In cooperation with the Austrian mint, a few test coins were fabricated. Previous to their minting they were dredged with fillings from copper or copper/silver alloys respectively. Some of these test coins were then treated with potassium-polysulphide (saturated  $K_2S_x$  for 8 hours at room temperature). This should model a long lasting exposure to  $H_2S$  and other organic sulphur compounds, maybe responsible for such corrosion. Other coins were stored together with ancient coins to monitor the corrosion process under real conditions.

First measurements of  $K_2S_x$  treated coins were done with voltammetry and electron microscopy. Results are published together with results of SIMS investigations accomplished

during this PhD-thesis (see **chapter 5.10: Brown spot corrosion on historic gold coins and medals**).

A second paper focuses these SIMS investigations (see **chapter 5.9: Investigations of corrosion phenomena of gold coins with SIMS**).

#### 4.2.1. Investigations with dynamic SIMS



**Figure 44:** left side: front side of ducat Ag before SIMS measurements; suitable sites for SIMS investigations are labelled;

Right side: enlarged area of ducat Ag after SIMS investigations; sputter corroded areas are visible.

The SIMS measurements itself lasted more than 3 weeks. As seen in figure 44, several measurements were necessary to accomplish an overall characterization of the corrosions. There were two samples dedicated for this research, one with pure silver grains (“Ducat Ag”), and one with grains consisting of a copper-silver alloy (“Ducat Ag/Cu”). Main task for SIMS was examining the corrosion forming elements at the surface and at the corrosion stain in the depth: oxygen, sulphur, chlorine. That’s why most measurements were accomplished in negative mode using  $\text{Cs}^+$  primary ions.

Adjusting the ion beam at the samples always was pretty difficult. The stigmatic optics of the CAMECA IMS3f has a very narrow focus plane of about 100  $\mu\text{m}$ . Ordinary sample holder are ideally adjusted to gain optimal focus conditions to flat samples, unfortunately these sample holders were too small for our measurements. In the finally used sample holder the coin was out of the ideal focus plane, just about 200  $\mu\text{m}$  nearer to the extraction lens. Additionally it was not flat enough for ideal measurement conditions. This causes two problems: Images of the samples are difficult to focus, especially when high resolution is needed (every time the measurement site was shifted more than 2 mm the whole optics had to be refocused, taking at least half an hour). The second problem touches depth profile recording; the sample position nearer the extraction lens results in a drifting apart of the imaged area with and without offset and also when the sample surface is charging. If not compensated, it won't be sure whether the measured signals with and without offset are from the equal position! Most complicated is the situation in a combination of imaging and depth profiling, the 3D-depth profile mode, where both effects are influencing the measurement. Although most times a compensation of these effects was possible, previous to every measurement the primary- and especially the secondary part had to be adjusted substantially.

Previous to the SIMS measurements microscopy pictures were taken of each sample spot on both decided coins and also overall images (see the overall image of "Ducat Ag" in figure 44). Spots interesting for SIMS measurements were decided and numbered. They were chosen in a way to be sided in flat regions (at the heads relief as well as in the flat region between relief and sideways labels) and be of proper size for at least one measurement consuming a region of about 0.5 x 0.5  $\text{mm}^2$ .

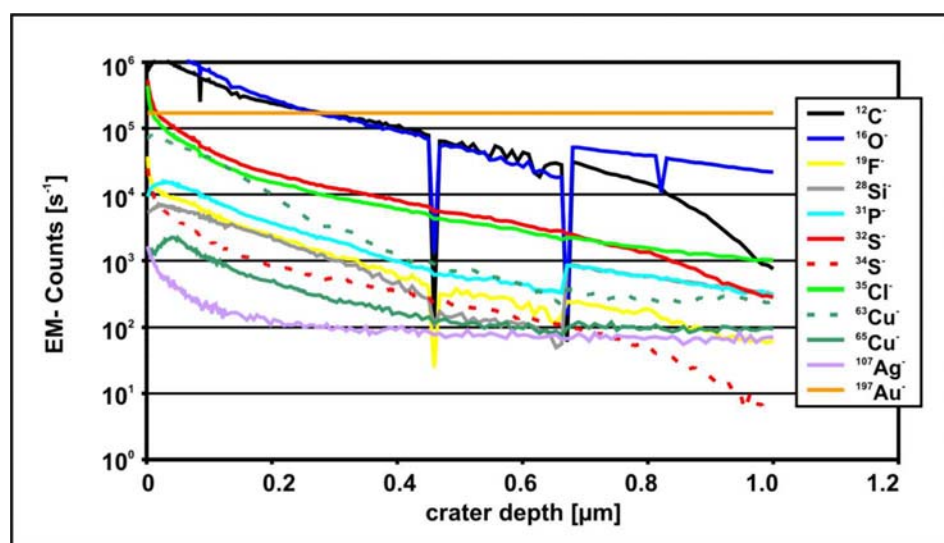


**Figure 45:** "Ducat Ag": first depth profile of a not corroded area

Primary ions: 10nA  $\text{Cs}^+$ , negative secondary ions



First depth profiles at “Ducat Ag” revealed a huge carbon containing layer at the surface, probably resembling from dust particles at the surface. At mass 63 an interference of the copper isotope  $^{63}\text{Cu}$  with some other molecule ions is observable. We guess it was  $\text{PO}_2^-$ . Due to the low sensitivity of copper a detaching of this molecule ion is not feasible; fortunately it does not interfere with copper isotope  $^{65}\text{Cu}$ , that’s why this was used for later data interpretation. Another possible interference is at mass 32, where  $^{32}\text{S}$  and  $(^{16}\text{O})_2$  are detectable. Both elements have an additional isotope at  $^{18}\text{O}$  (0.2 %) and  $^{34}\text{S}$  (4.5 %) respectively (abundance of  $^{16}\text{O}^{18}\text{O}$ : 0.4 %; all abundances from “isotopic pattern” of the “Sheffield Chemputer” [53]). The isotopic proportion of  $\text{O}_2^-$  and  $\text{S}^-$  differ by an order of magnitude; in our investigation almost all signals at mass 32 rely to sulphur, interpretation was done with  $^{34}\text{S}$  due to possible detector saturation with higher  $^{32}\text{S}$ .

After doing a few depth profiles and some images of the surface, the coin was removed from the SIMS device and the surface was cautiously cleaned with ethanol drenched Q-tips. Afterwards the coin was once more investigated. This time there was a power of magnitude less carbon (and oxygen) at the surface.

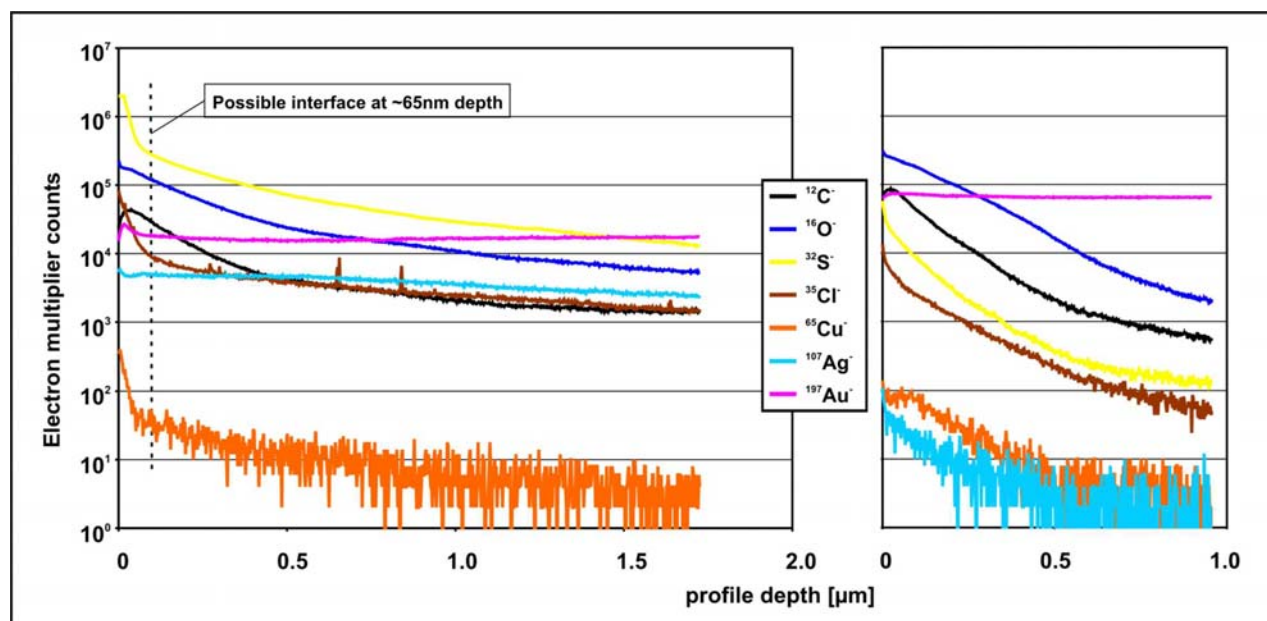


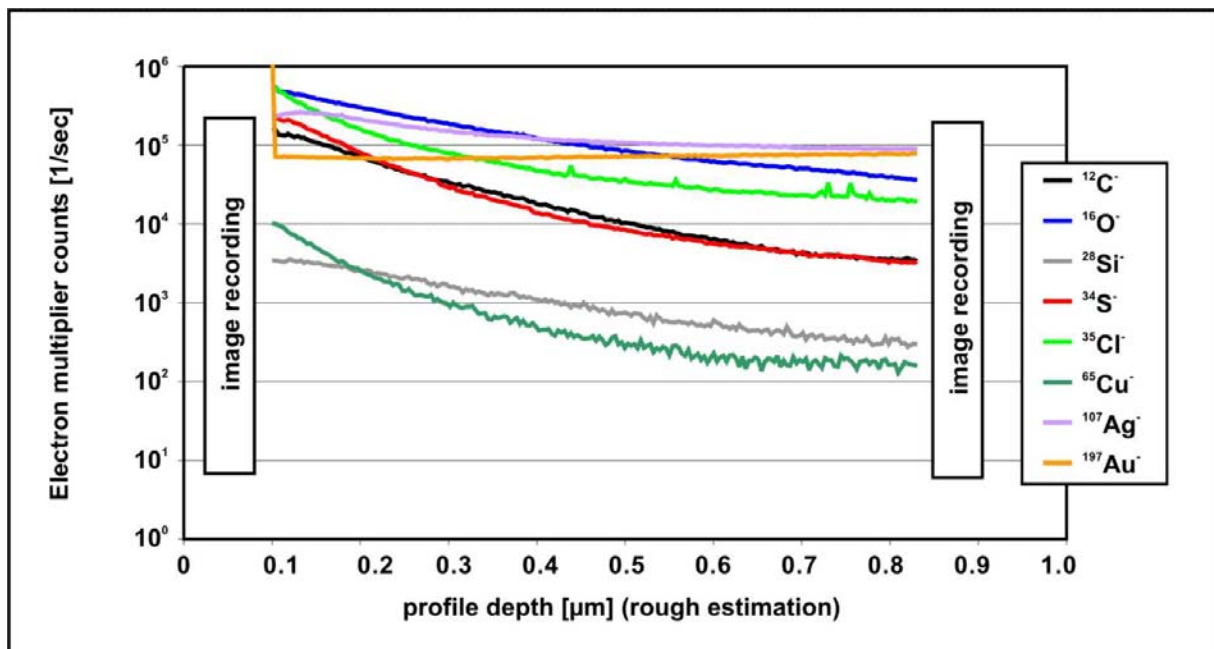
**Figure 46:** depth profiles of “Ducat Ag”; left side at a corrosion stain, right side a not corroded area;

Primary ions: 10nA Cs<sup>+</sup>, negative secondary ions

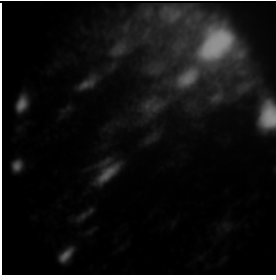
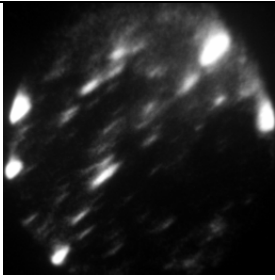
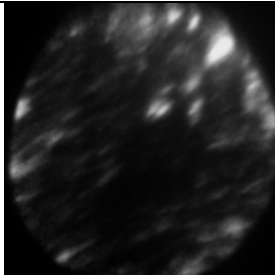
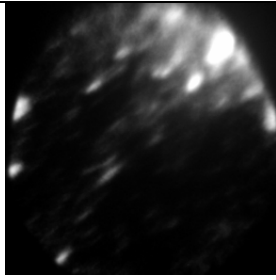
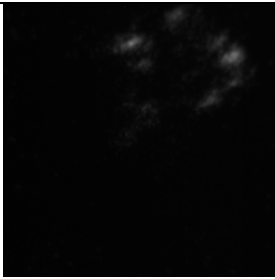
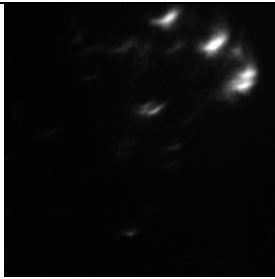
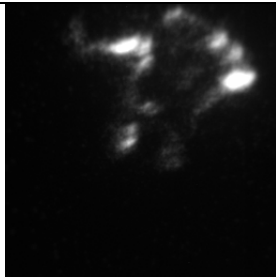
Figure 46 shows depth profiles of a stain and a region without visible corrosion. On the left side, the graph of  $^{197}\text{Au}$  is lower than on the right one; silver displaces it. After 1.6  $\mu\text{m}$  measurement the silver splint is still present, as well as most other monitored elements like carbon, oxygen and sulphur. There are only differences directly at the surface, where these

trace elements are much quicker fading at a spot without stain. Still there might be differences in the lateral distribution of the elements, not visible with depth profiles. Interesting is that all signals, even  $^{65}\text{Cu}$ , are not background signals, checked by a change of raster size at the end of both depth profiles (cut in Figure 46).

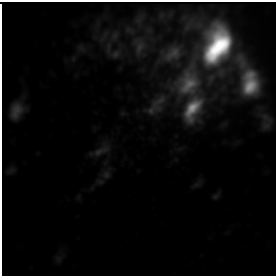
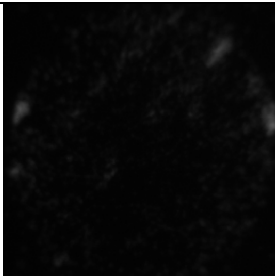
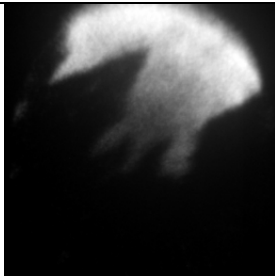
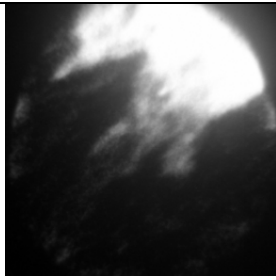
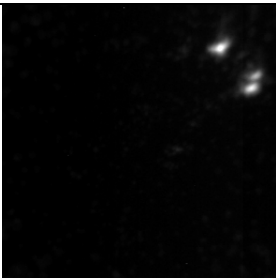
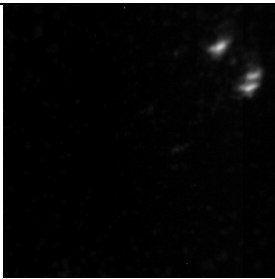
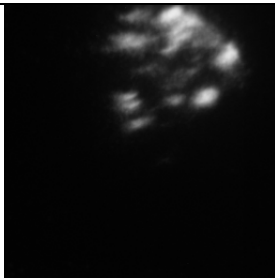
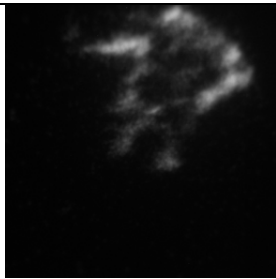
A chance getting lateral information is in the imaging mode. At first we tried to capture mass images separated from depth profiles. Later one depth profile was recorded between two series at the same spot (see Figure 47 and images 48 to 59). At this spot a silver stain has been profiled together with a corroded extension.



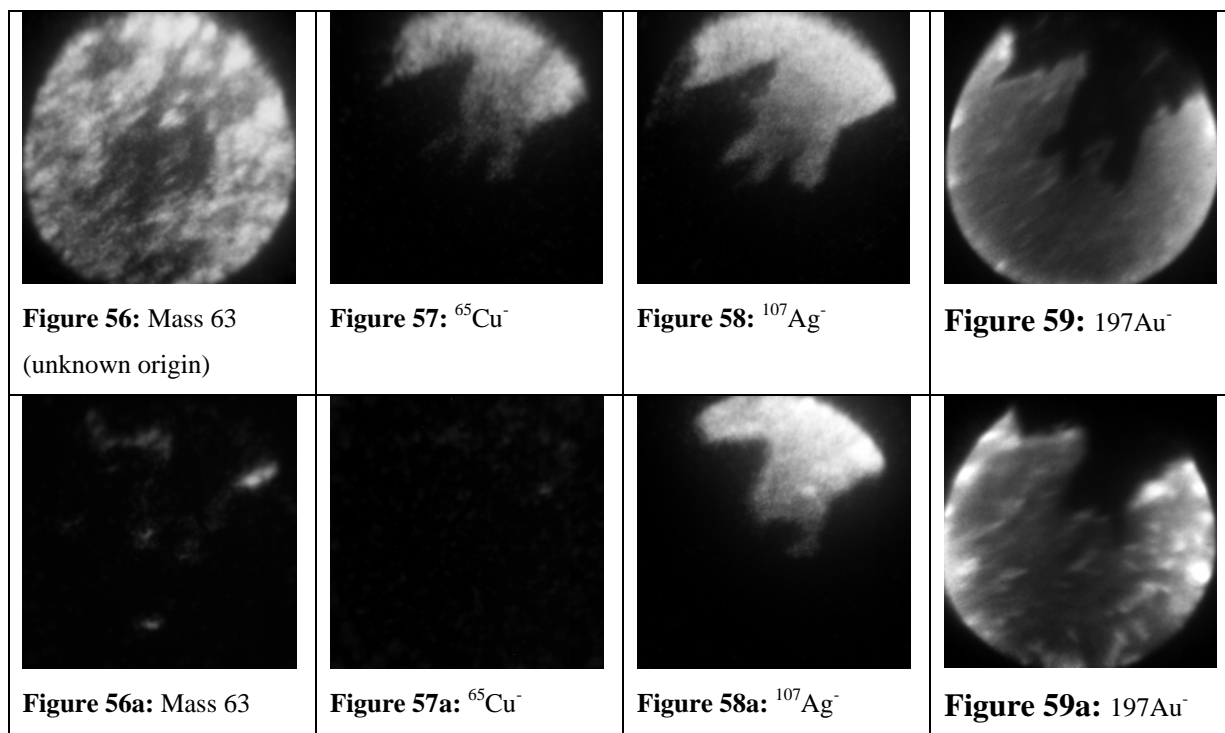
**Figure 47:** “Dukat Ag” at a contaminated spot, the depth profile was recorded between two image series shown in figures 48 to 59 (beforehand) and 48a to 59a (after depth profile) , respectively; primary ions: 10nA Cs<sup>+</sup>, negative secondary ions

			
<b>Figure 48:</b> $^1\text{H}$	<b>Figure 49:</b> $^{12}\text{C}^-$	<b>Figure 50:</b> $^{16}\text{O}^-$	<b>Figure 51:</b> $^{26}\text{CN}^- (?)$
no image of mass 1 after depth profile available			
	<b>Figure 49a:</b> $^{12}\text{C}^-$	<b>Figure 50a:</b> $^{16}\text{O}^-$	<b>Figure 51a:</b> $^{26}\text{CN}^- (?)$

**Images 48 to 51a:** show channelplate image captures displaying the lateral distribution of some elements ranking among the depth profile in figure 47; imaged sample size is 150 $\mu\text{m}$  in diameter; top row shows images before- bottom row images after the depth profile.

			
<b>Figure 52:</b> $^{28}\text{Si}^-$	<b>Figure 53:</b> $^{31}\text{P}^-$	<b>Figure 54:</b> $^{32}\text{S}^-$	<b>Figure 55:</b> $^{37}\text{Cl}^-$
			
<b>Figure 52a:</b> $^{28}\text{Si}^-$	<b>Figure 53a:</b> $^{31}\text{P}^-$	<b>Figure 54a:</b> $^{32}\text{S}^-$	<b>Figure 55a:</b> $^{37}\text{Cl}^-$

**Images 52 to 55a:** show channelplate image captures displaying the lateral distribution of some elements ranking among the depth profile in figure 47; imaged sample size is 150 $\mu\text{m}$  in diameter; top row shows images before- bottom row images after the depth profile.



**Images 56 to 59a:** show channelplate image captures displaying the lateral distribution of some elements ranking among the depth profile in figure 47; imaged sample size is 150 $\mu\text{m}$  in diameter; top row shows images before- bottom row images after the depth profile.

The depth profile in figure 47 looks similar to 46. More interesting is the comparison with the lateral images before and after the depth profile. All images shown in figures 48 to 59 are captures from the channel plate, the image acquisition time was adjusted to the signal intensity, the lower the intensity, the longer it was. Focus readjustment and mass adjusting took another time, so it is impossible to specify the beam-on time during image capturing.

In the series of figures 48 to 59 each mass (except for hydrogen) is shown twice; upper image is beforehand the depth profile, lower image (labelled with an “a”) after the depth profile.

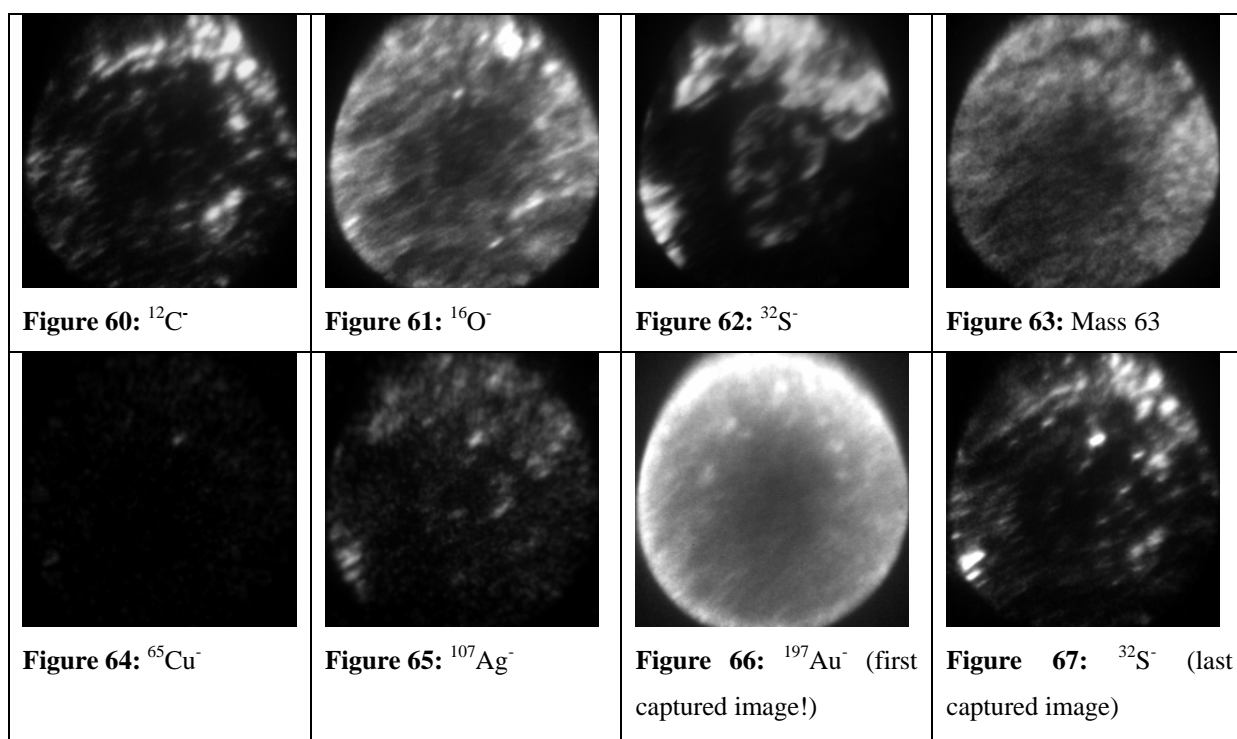
From the signals of silver and gold the stain shape is clearly visible. It looks like the stain surface mostly consists of  $\text{Ag}_2\text{S}$  together with impurities of chlorine and probably also copper (only visible with mass 65. At mass 63 there is an interference probably with the molecule ion  $\text{PO}_2^-$ ; although both oxygen and phosphorus are distributed unlike mass 63).

The elements carbon, oxygen, hydrogen and silicon show no correlation with the stain. More probably they come from surface contaminants. The signal of mass 26 (often an indicator for nitrogen in form of  $\text{CN}^-$ ) is a mixture of the carbon distribution with a heightened signal part

shaped like the stain. There was almost no signal at mass 31 (phosphorus), the theory of  $\text{PO}_2^-$  at mass 63 seems unlikely.

After the depth profile has ablated approximately  $1\ \mu\text{m}$  the stain shrank a little bit, tailings in the image centre faded away; visible in figures of silver (Figure 58a) and gold (Figure 59a). Sulphur is still covering the stain, but no more homogeneously (Figure 54a). Interesting is chlorine, enriched at the silver splint edges (Figure 55a). Most other trace elements are faded.

Another image series was done at a stains edge with no splint in the visible image area.



**Images 60 to 67:** show channelplate image captures displaying the lateral distribution of some elements captured sideways of a silver stain at coin “Ducat Ag”; imaged sample size is  $150\ \mu\text{m}$  in diameter.

Here gold is homogeneous while sulphur as well as silver is enriched at the stain. After capturing 10 images, mass 32 (sulphur) was investigated once again, this time sulphur is only visible at some spots. Once again, oxygen is spotty but even distributed, and carbon is enriched within some grains, here enriched a little bit in the stain area (polluting grains situated here due to a rougher surface?).

Most complex is a 3D-depth profile. We did only one at a silver splint. The measurement included eight masses ( $^{12}\text{C}$ ,  $^{16}\text{O}$ ,  $^{28}\text{Si}$ ,  $^{32}\text{S}$ ,  $^{34}\text{S}$ ,  $^{35}\text{Cl}$ ,  $^{65}\text{Cu}$ ,  $^{107}\text{Ag}$ ,  $^{197}\text{Au}$ ) and was recorded down to a depth of  $1,9\ \mu\text{m}$  (taking 5 hours in 2 measurement runs, each with 200 cycles). The mass table was reduced to gain stable measurement conditions.

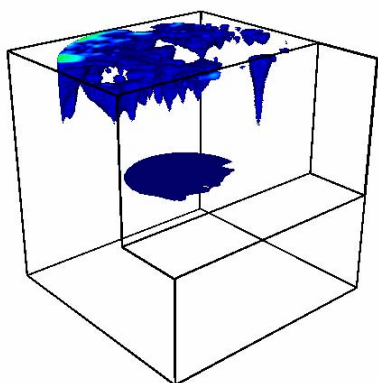


**Figure 68:**  $^{12}\text{C}^-$

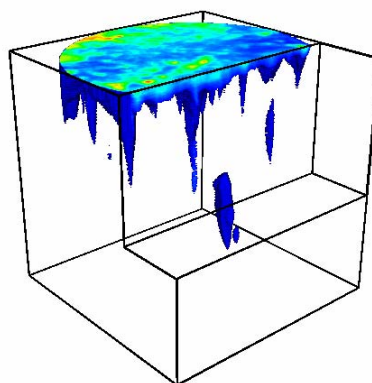


**Figure 69:**  $^{16}\text{O}^-$

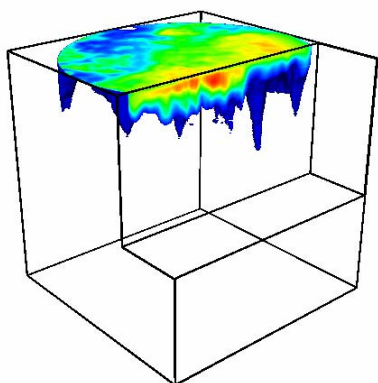


**Figure 70:**  $^{32}\text{S}^-$

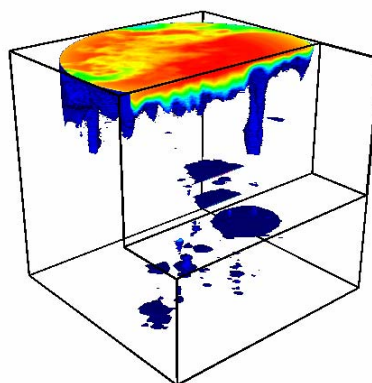


**Figure 71:**  $^{35}\text{Cl}^-$

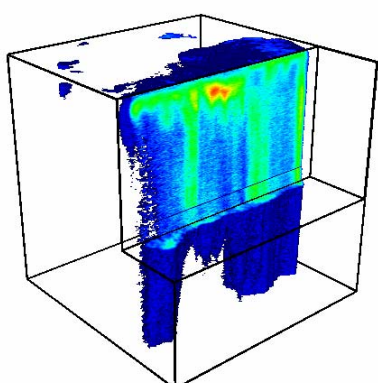


**Figure 72:**  $^{107}\text{Ag}^-$

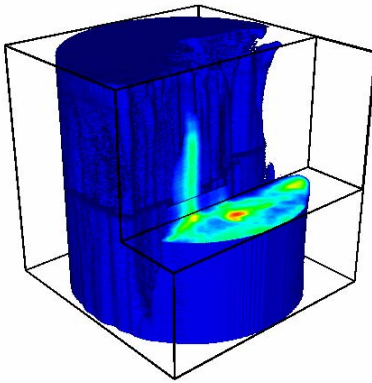


**Figure 73:**  $^{197}\text{Au}^-$

**Figures 68 to 73:** 3D images from coin “Ducat Ag” size of all cubes is  $150\mu\text{m} \times 150 \mu\text{m}$  into x- and y-direction and  $1.9 \mu\text{m}$  in z-direction; Data stems from 2 depth profiles recorded subsequently, in some images (Ag and Au) the gap is visible.

Figures 68 to 73 show 3D cubes of the elements carbon, oxygen, sulphur, chlorine, silver and gold. Here clearly the surface covering distribution of sulphur and chlorine can be seen. It almost fades down to the splints shape after about 100 nm (10 cycles). Chlorine is longer present, but only at the splint edges.

#### 4.2.2. Investigations on historic coins with TOF-SIMS

Although the summary of the dynamic SIMS investigations show some exciting, new results, time and afford getting these was very high and the destruction of the sample surface wider than assumed afore. Therefore, we decided to do the measurements of ancient coins at a TOF-SIMS device. With this method, we are able to gather more information out of less sample material. The drawback of a lower detection limit of all elements should do no harm, due to the most elements of interest were well detectable in former dynamic SIMS measurements. Especially omnipresent elements gold, sulphur, chlorine, carbon and oxygen are at high level, only silver and copper, in dynamic SIMS measurements near detection limit, could be a problem. It was hoped that signals of these elements will get a boost due to fact, that there is no offset necessary in TOF-SIMS measurement due to its increased mass resolution.

Another reason is the chance of measuring organic compounds at the surface. TOF SIMS opens the field of organic surface analytics. The storage environment of the coins in question is suspected to have big influence on the surface constitution.

Both ancient coins are in museum possession since their coining. Over the years they were treated countless times e.g. polished, or simply handled. They were stored in wooden bins (oak wood) as ancient as the coins itself. Studies from the Kunsthistorisches Museum [54] show, that they are outgassing a mixture of sulphur containing organic compounds (thionyles, thioethres,...). Due to the oak bins are seclude air well, these compounds get enriched and may harm coin surfaces significantly. That's why coins are treated with a waxy polish, to get an inert coverage protecting the surface from harmful substances.

Although this treatment was carried out with all coins, still there seems to be corrosion damage on some coins, best visible on gold coins, where only punctiform changes happened. In order to find origin substances, therefore a TOF-SIMS was preferred to the dynamic SIMS device from first investigations.

Measurements were done by courtesy of the "Kernforschungszentrum Jülich, Germany" in within 3 days (compare 3 necessary for dynamic SIMS measurements) with an ION-TOF IV device [1,55]. Profiles were done using Bi<sup>+</sup> analysing primary ions (1.6pA; 25kV, 200x200 points equals 189.9 µm edge length) and a Cs<sup>+</sup> sputter gun (106.9nA; 2kV; 350x350 µm<sup>2</sup> abrasion size; beam on time after every 10<sup>th</sup> cycle was 1 or 10 seconds, respectively).



4 coins were taken for measurements, 2 originals from 1820 (figure 74) and 1874 (figure 75) respectively, and 2 test ducats with similar history to those used in the former study. All coins were not especially pre-treated in order to get additional information from the organic surface.



**Figure 74:** Coin 3252ac  
1 Sovrano, Wien 1820



**Figure 75:** Coin 129073  
8 Gulden, Wien 1874

Due to first tests of the measurement conditions at one of the test coins didn't evince charging of the sample surface from ion bombardment, we decided not to use the electron gun for charge compensation. Unfortunately with changing to ancient coins, situation changed as well. The first depth profile at coin 129073 revealed minor charging of the surface. It effected a wild mass shifting of several 100s of ppm. Figures 77 and 76 show sections of mass spectra from this first depth profile (scan 60117) and the first profile with electron gun assistance (scan 60119), respectively.

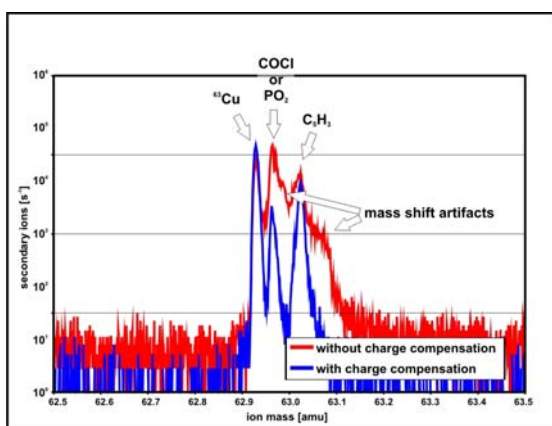


**Figure 76:** Section of two mass spectra (scan 60117, 60119); besides some other peaks copper is detected here.

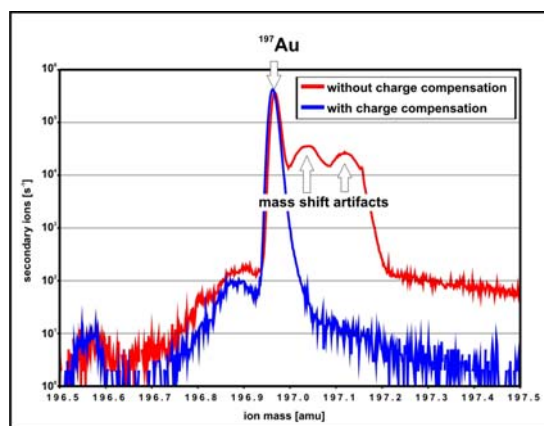


**Figure 77:** Section of two mass spectra (scan 60117, 60119); the strong signal of  $^{197}\text{Au}$  dominates.

This mass shifting caused errors in the signal projection in this depth profile (see figure 78). Signals of each mass became instable due to permanent shifting of the mass range. A compensation routine implemented in the data processing software [56] was not able to compensate these shifts. Indeed, all inputs into this routine so far worsened the problem. Also you can see spikes downward in figure 78 every 10<sup>th</sup> cycle. This is caused by the huge charge load from the Cs<sup>+</sup> sputter gun, not at once well compensated. Still after activating the electron gun, still the signal remained saw tooth like. This is probably caused by a matrix effect from the dropping caesium concentration within the 10 cycle's measurement. By calculating average values of the signals of 10 cycles each, it was possible to plain this artefact.

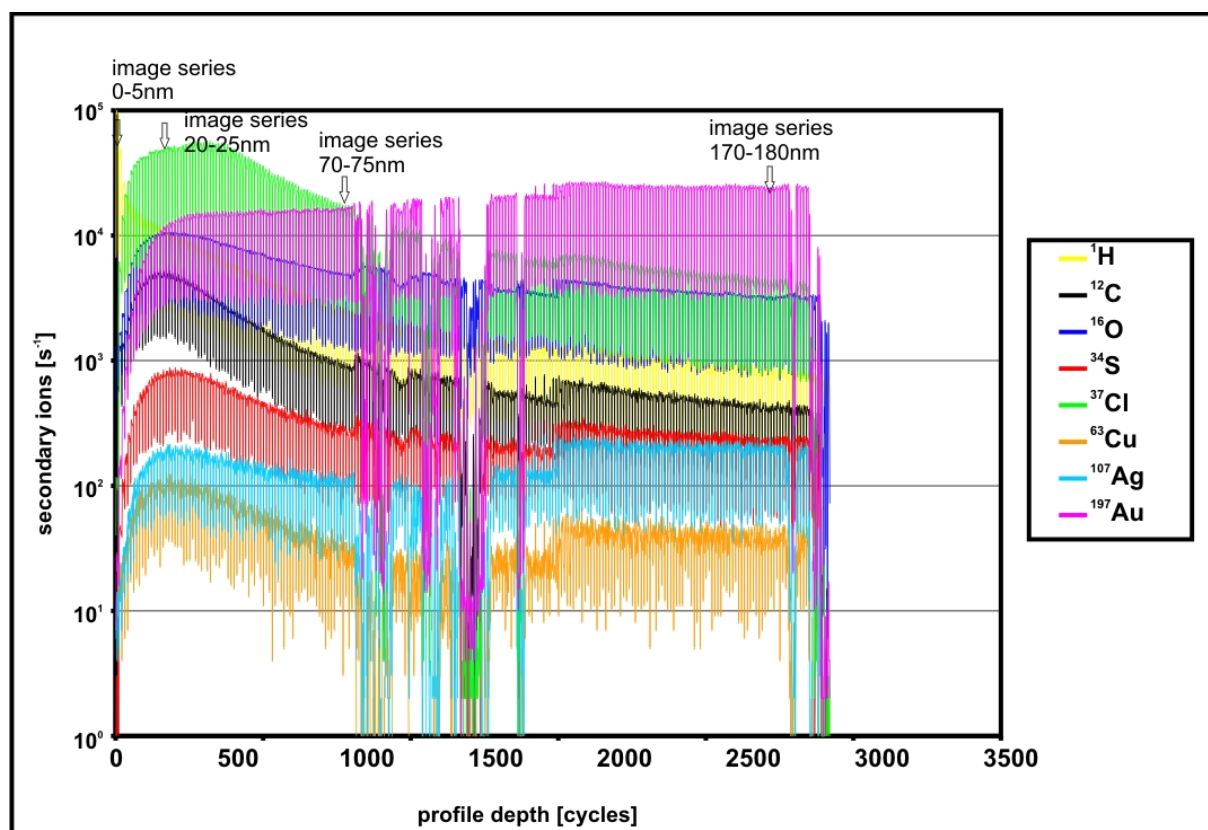


**Figure 78:** Raw data depth profile of coin 129073 (scan 60117); no charge compensation from the electron gun was used, due to sample charging this causes shifting of the mass table.

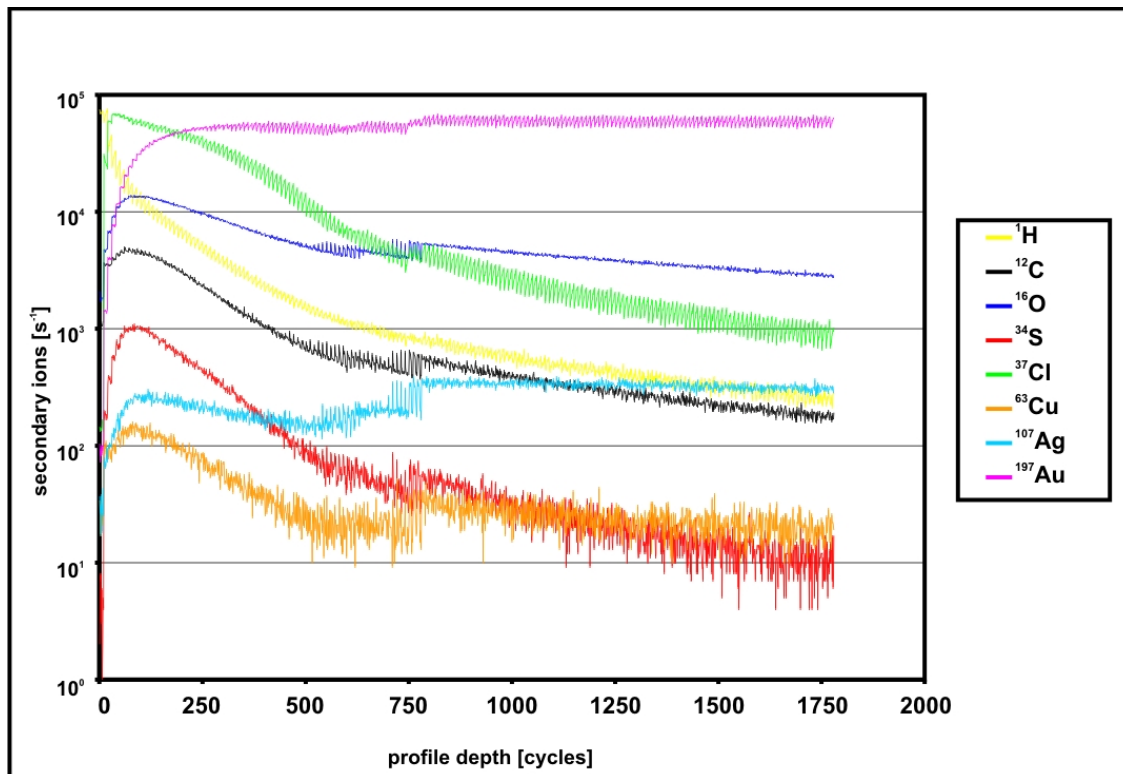


**Figure 79:** Raw data depth profile of coin 129073 (scan 60123); although the electron gun was on, there is still a saw tooth pattern in the signals, probably caused by a matrix effect from the changing caesium concentration at the surface

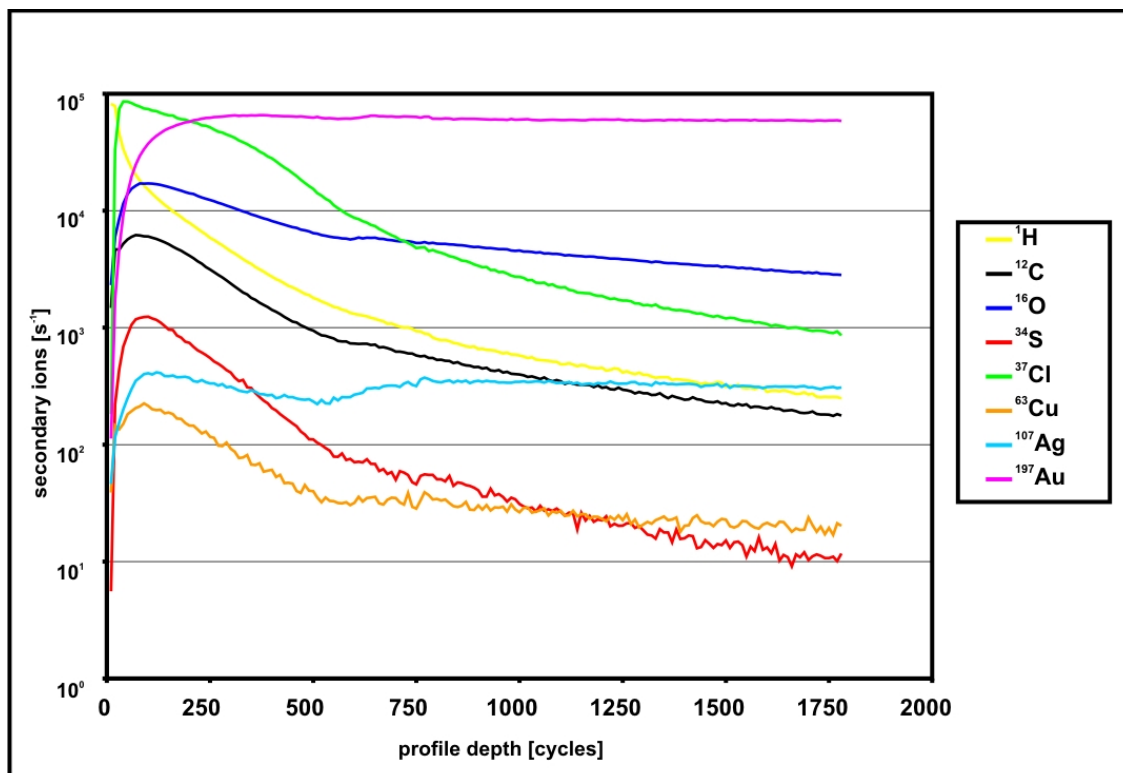


**Figure 80:** corrected depth profile of scan 60123 (compare with figure 79). Data noise was suppressed by averaging each 10 cycles, fluctuations from the primary beam were corrected manually or by multiplying with a constant.

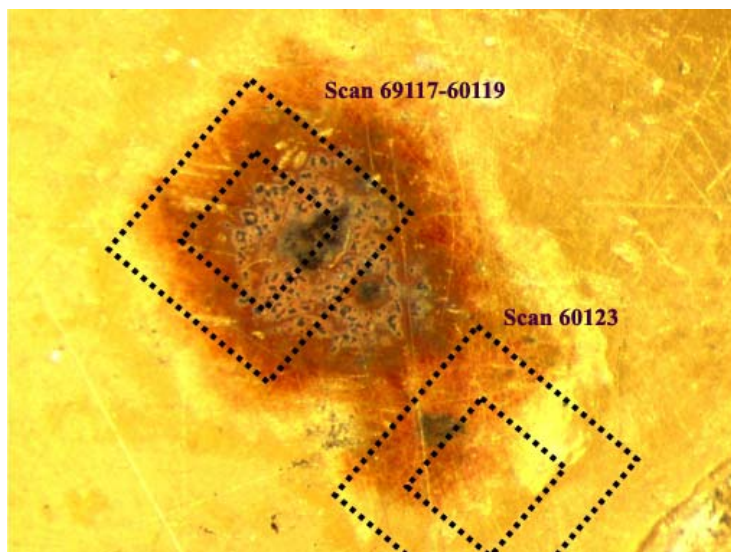


**Figure 81:** Measurement spots on coin 129073 (see figure 75) outer line represents the full ablated area, inner line the imaged area. The left spot is situated atop an Ag/Cu grain; the right spot investigates branches of the neighbouring splint.

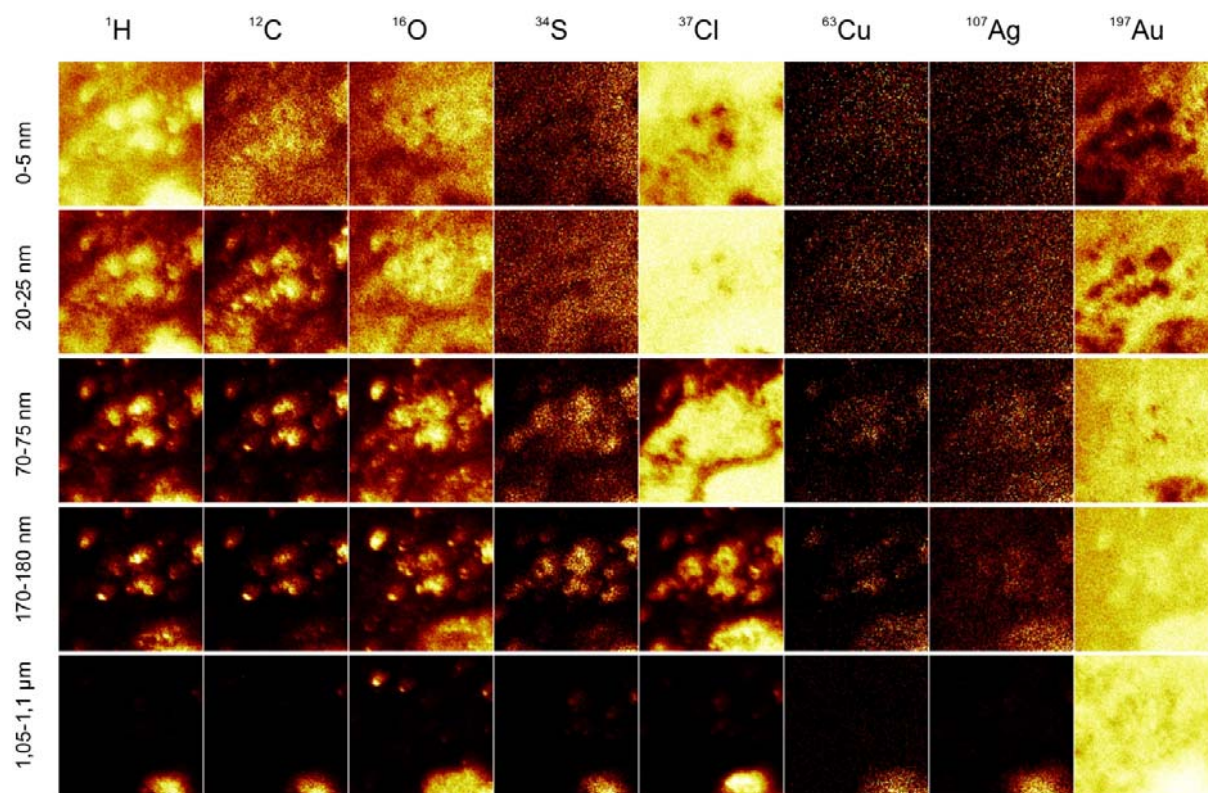


**Figure 82:** Image series of coin 129073, from top to bottom depth is rising; images of row 1-4 are taken from the depth profile presented in figure 78 (scan 60117; labelled with marks), last row images are taken from an additional measurement at the same position with raised ablation velocity; visible image area is 189.1x189.1 μm<sup>2</sup>; each image is a sum of 100 measurement cycles (each point has an information depth of 100 bit)

### **Scan 60117 – 60119 at Coin 129073**

At Coin 129073 (ducat from 1874; see figure 75) two depth profiles were recorded. An image of the spots is shown in figure 81. At this coin only a few corroded spots were visible, the sampled one was by far the biggest, so we were able to record two depth profiles side by side. The first profile consists of 3 scans (60117, 60118, 60119), which were recorded subsequently. Parting the profile was necessary because of changing the measurement conditions. First scan (60117; 2420 cycles) was recorded with 1 second Cs<sup>+</sup> sputter beam on each 10<sup>th</sup> cycle, in the second scan (60118, 850 cycles) the sputter time was increased to 10 seconds each 10<sup>th</sup> cycle and for the third scan (60119; 350 cycles) the electron gun turned on. This profile was the first one with heavy charging effects. In figure 79a raw data depth profile of some chosen masses is shown. It can be seen, that there is no chance of a correct data interpretation of the depth profile. The mass table is shifting several 100 ppm in some cycles. But there are some regions with more stable signals. These were at least good enough for lateral images. Figure 82 shows images of 8 masses at specified depth. First 4 rows are taken from scan 60117 (see labels in figure 78), last row from the end of scan 60119. In these images a silver/copper splint is visible in the bottom right edge, some additional grains with a size of about 10-20 µm are beyond it. In the first two rows the coverage of the elements is almost closing, whereas gold has a very weak signal and some holes. These holes are similar distributed to the later distribution of the contaminant elements. In the third row, the contaminant elements are more and more concentrated at the splints itself, whereas gold is successive becoming homogeneous. In row 4 all elements except for gold are only visible at the splints, and gold is now homogeneous, the signal boost at the big splint probably arises from a matrix effect. The simple fact, that there is gold visible means, that these splints either contain gold or have pinholes looking through the splints to the gold (latter is not very likely). In row 5 (at approximately 1 µm depth) the grains have fade away, only the splint is still visible. Within the grain, all masses are homogeneous distributed. This points out a complete corrosion of the splint.

### Scan 60123 at Coin 129073

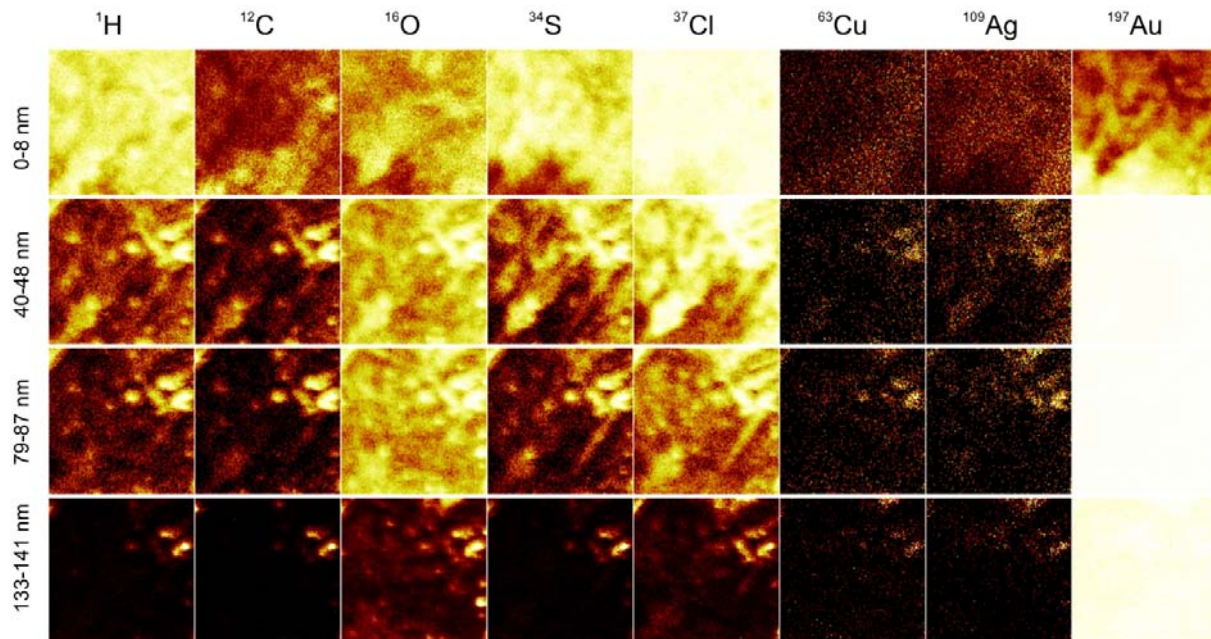
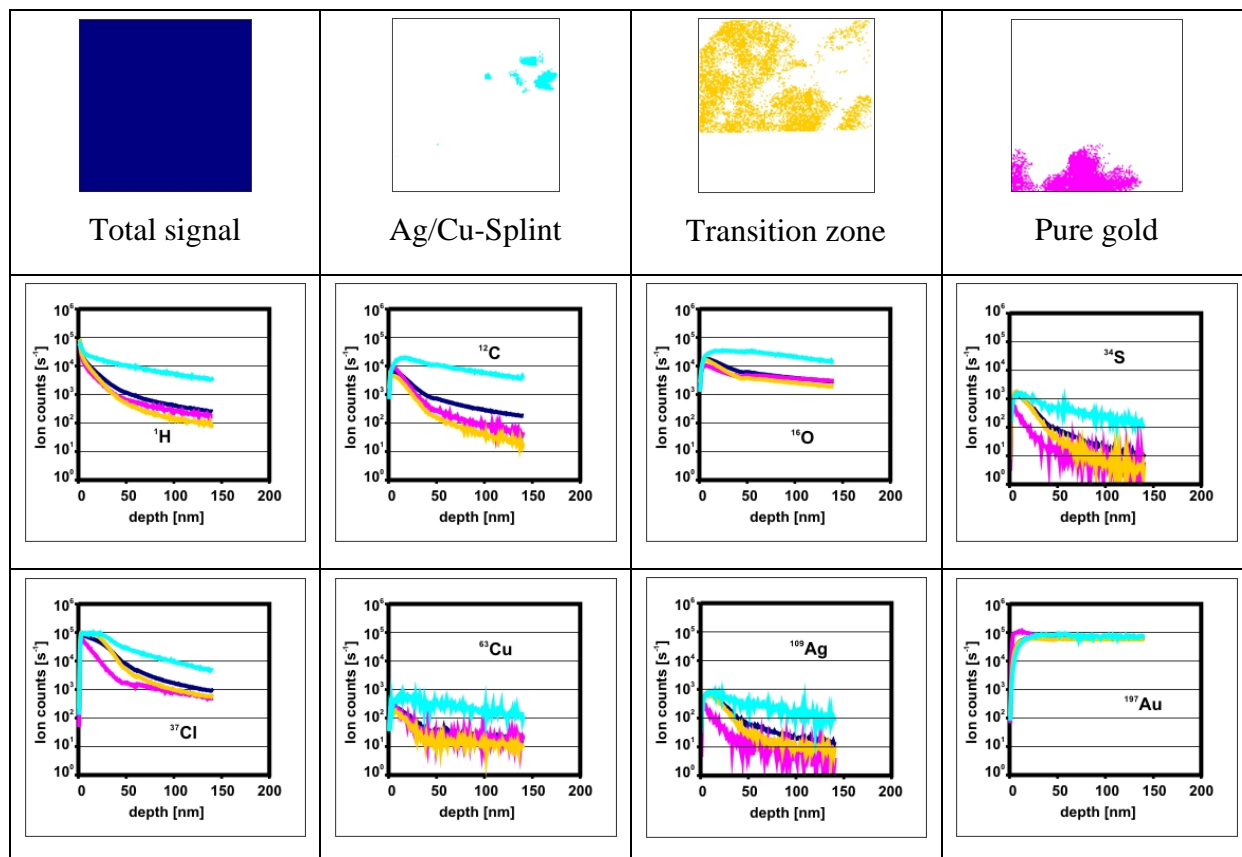


**Figure 83:** Image series of coin 129073, from top to bottom depth is rising; images are taken from scan 60123; visible image area is  $189.1 \times 189.1 \mu\text{m}^2$ ; each image is a sum of 100 measurement cycles (each point has an information depth of 100 bit)

This depth profile is taken from an area nearby the beforehand described profile (see figure 81). Figure 83 shows a series of images from 8 masses from several depths. This time the splint is out of view at the top side of the image area. Still there are contaminants visible both in the photo, as well as in the images showing the mass distribution of some masses. Most contaminant elements (here represented by the images of hydrogen, carbon, oxygen, sulphur and chlorine) are enriched alongside some scratches (the deepest is also visible in the photo taken before the measurements, see figure 81). Copper and silver are almost homogeneous distributed at the surface, in deeper regions enriched within some grains at the top right side of the images. Interesting is oxygen, which is also in deeper regions visible besides these enrichments, whereas hydrogen, carbon and sulphur are only visible within the grains. How far this is influenced by a matrix effect is not estimable. Except from the first cycles gold is homogeneous distributed; none of the grains is very extensive.

Depth profiles (table 4) are quite similar; contaminants are concentrated at the silver/copper grains; at the free surface they fade away quickly, at the pure gold (in the images the area at the bottom) quicker (only a few nm), in the transition zone approximately 50 nm.

**Table 4:** processed data of scan 60123; images in the first row show the areas where the depth profile data is excerpted from (colours are chosen according to the colour of the graphs in the depth profiles below). Each depth profile represents the approach of a single mass signal at these different spots. All depth profiles are normalized to counts per second of the whole area.



**Scan 60120 at Coin 3252aα**

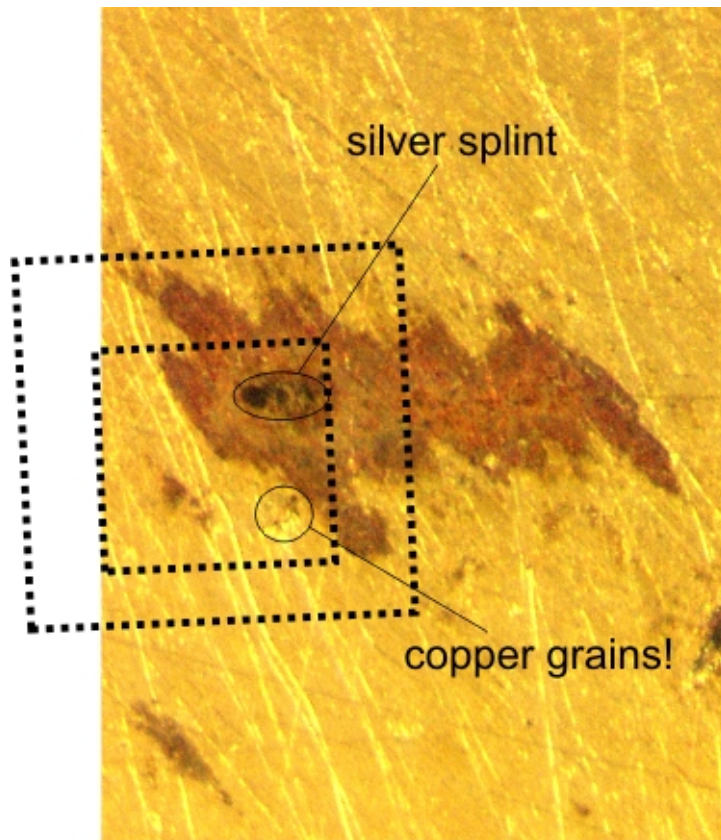


**Figure 84:** Measurement spot on coin 3252aα (total image of this coin in figure 74). Outer line represents the full ablated area, inner line the imaged area. Marked spots are sites where metallic grains are situated, which have been found in mass images (figure 85) and depth profiles (Table 5).

This spot was very interesting. Here 3 zones are represented by large areas: A visually clean surface, a corroded transition zone and a splint in the upper right corner. But the allocation of some elements at the surface (images of the first row in figure 85) does not fit with the microscope image of the corrosion. The small corrosion spot in the lower left part of the microscope image seems quite bigger than visible. Especially gold is not visible at a wide part of the surface. On the other hand, carbon, hydrogen and especially remarkable copper are situated right here. It seems there is a pure copper grain, whose corrosion is not visible in the microscope image! After 30 nm sputtering the distribution is much more like the microscope image. Silver is together with sulphur and chlorine prominent in the corroded area similar to the microscope image, copper has reduced its extension to a small area in the lower right part of the image, where also the signals of carbon, hydrogen and oxygen are very prominent (matrix effect?). After 60 nm sputtering, the transition zone clearly separates from the silver splint and a weak signal of copper is visible in the silver splint (most likely a copper-silver



alloy). Similar situation can be found at approximately 150 nm, the transition zone slowly fades away, copper and silver grain are still visible, remarkably is the allocation of hydrogen, carbon and sulphur near the copper grain: Their distribution is much more widespread than copper itself. It is likely, that copper is similar distributed, but due to much lower sensitivity, it is only visible in a small area. Gold has already closed around the copper grains, whereas the silhouette of the silver splint is still visible.

After about 130 nm the caesium beam has been intensified (see the data gap in the depth profiles in Table 5), the depletion has sped up. The last image series in figure 85 shows the elemental distribution at the end of the depth profile: Copper and silver grains are still visible, hydrogen, carbon and sulphur are situated at the same spot, also oxygen and chlorine, but latter elements are also visible in the area beneath these two grains. Gold is now almost homogeneous distributed except from the spot of the silver grain.

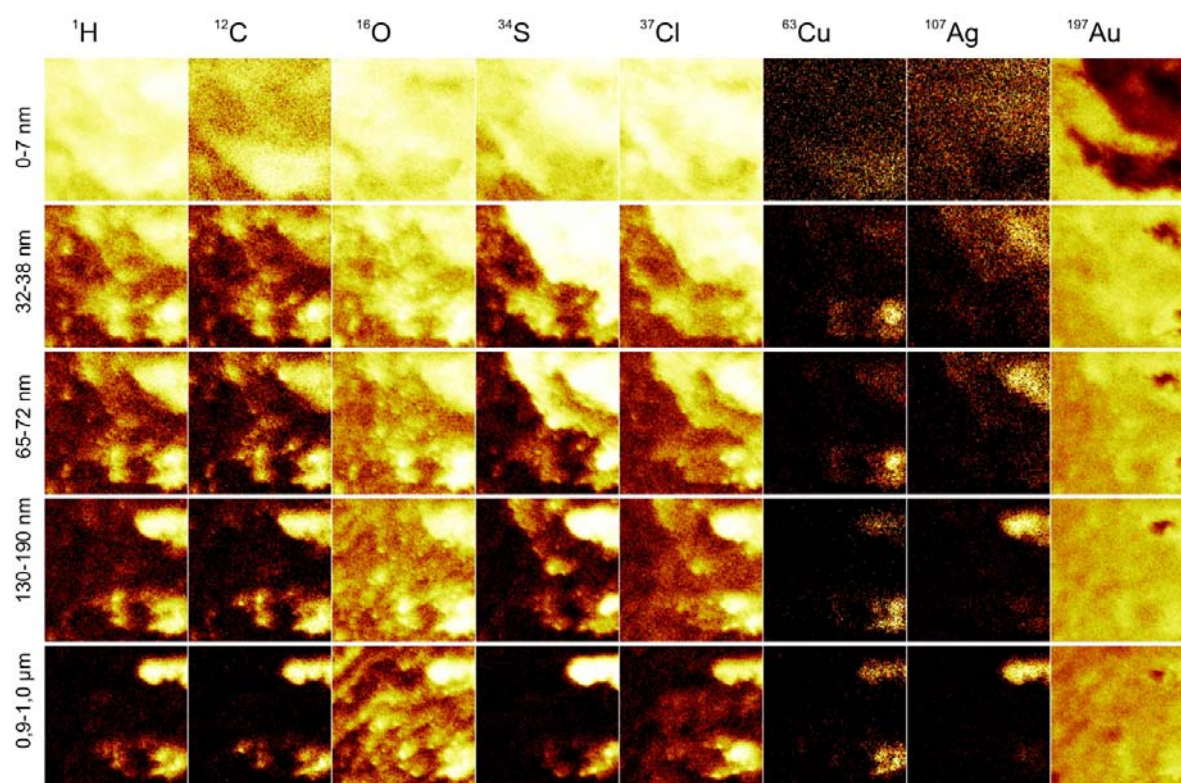
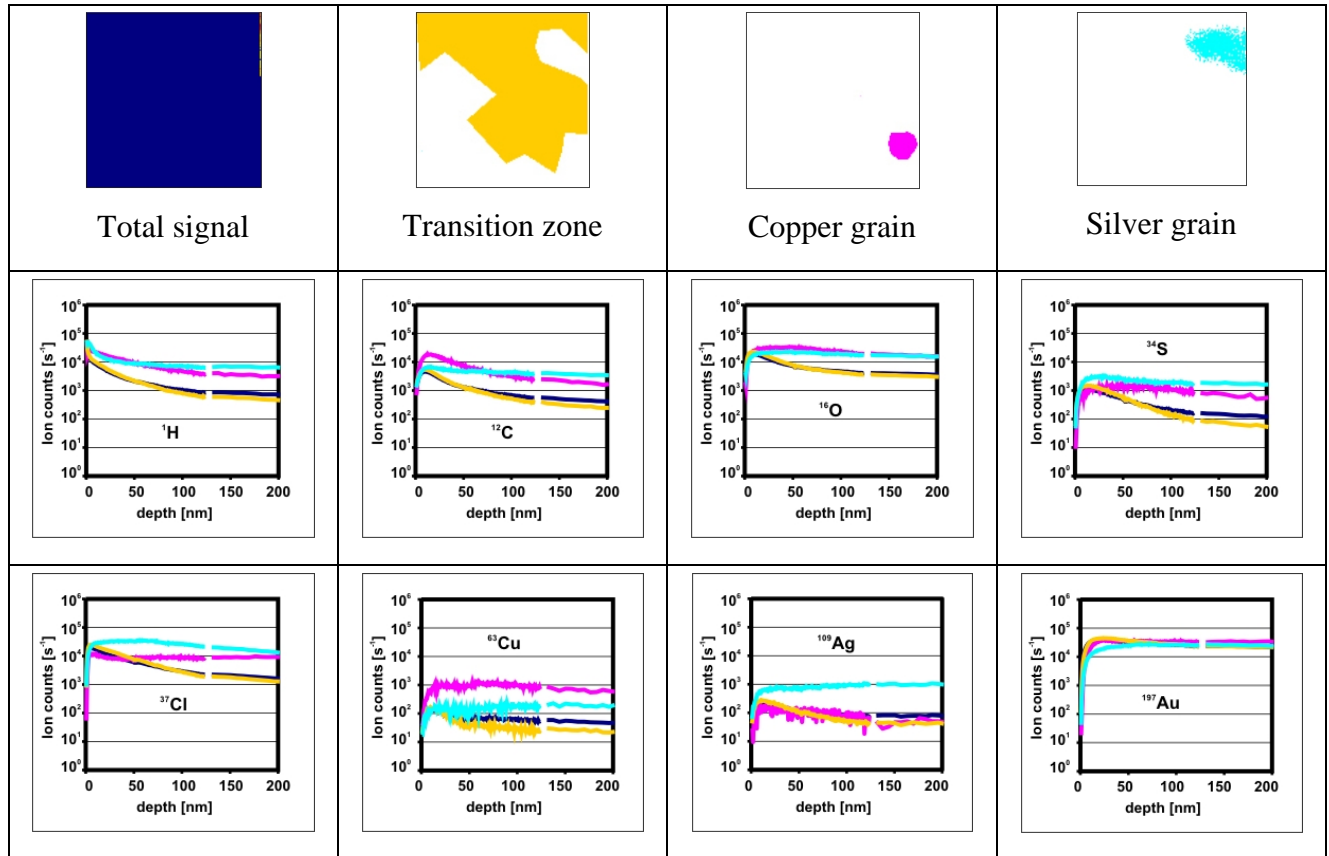


**Figure 85:** Image series of coin 3252α, from top to bottom depth is rising; images of row 1-3 are taken from scan 60120, images of row 4 and 5 are from scan 60121; visible image area is 189.1x189.1μm<sup>2</sup>; each image is a sum of 100 measurement cycles (each point has an information depth of 100 bit)

Depth profiles approve the statements of the image interpretation. There is copper in the silver splint, but no silver in the copper splint. Most contaminant elements are enriched at the splints, whereas at the residual area they fade away after about 50 - 100 nm

**Table 5:** processed data of scan 60120; images in the first row show the areas where the depth profile data is excerpted from (colours are chosen according to the colour of the graphs in the depth profiles below. Each depth profile represents the approach of a single mass signal at these different spots. All depth profiles are normalized to counts per second of the whole area.



## Scan 60116 at Coin Ag1

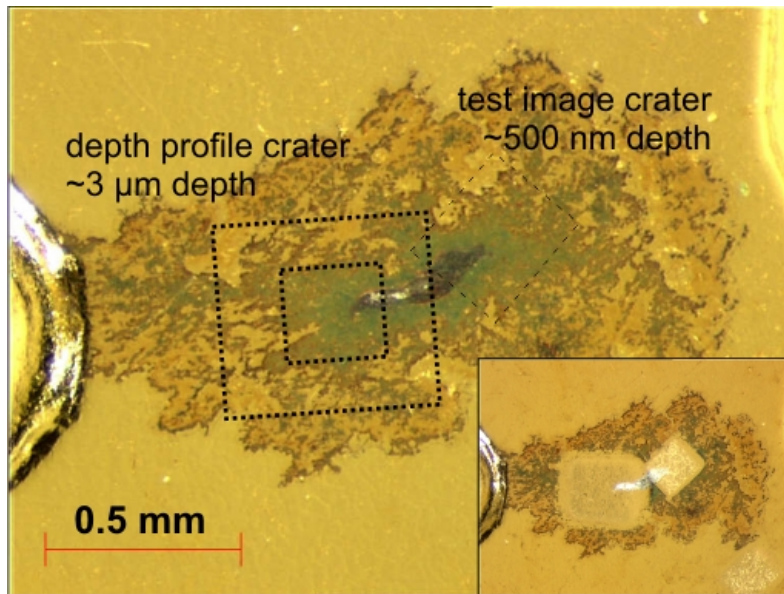


**Figure 86:** Measurement spot on test-coin Ag1. Outer line represents the full ablated area, inner line the imaged area. An adumbrated square to the right indicates a measurement spot of the test series (visible in the small image below, where the situation after SIMS measurements is documented).

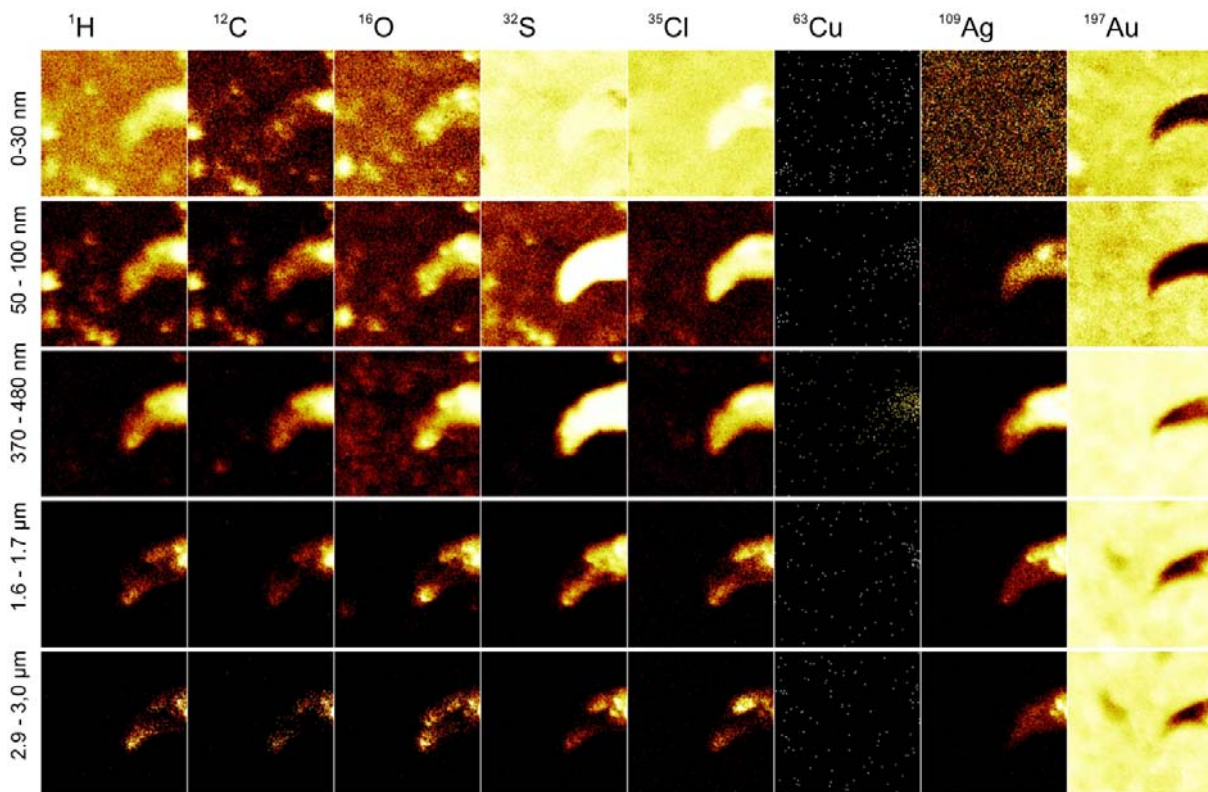


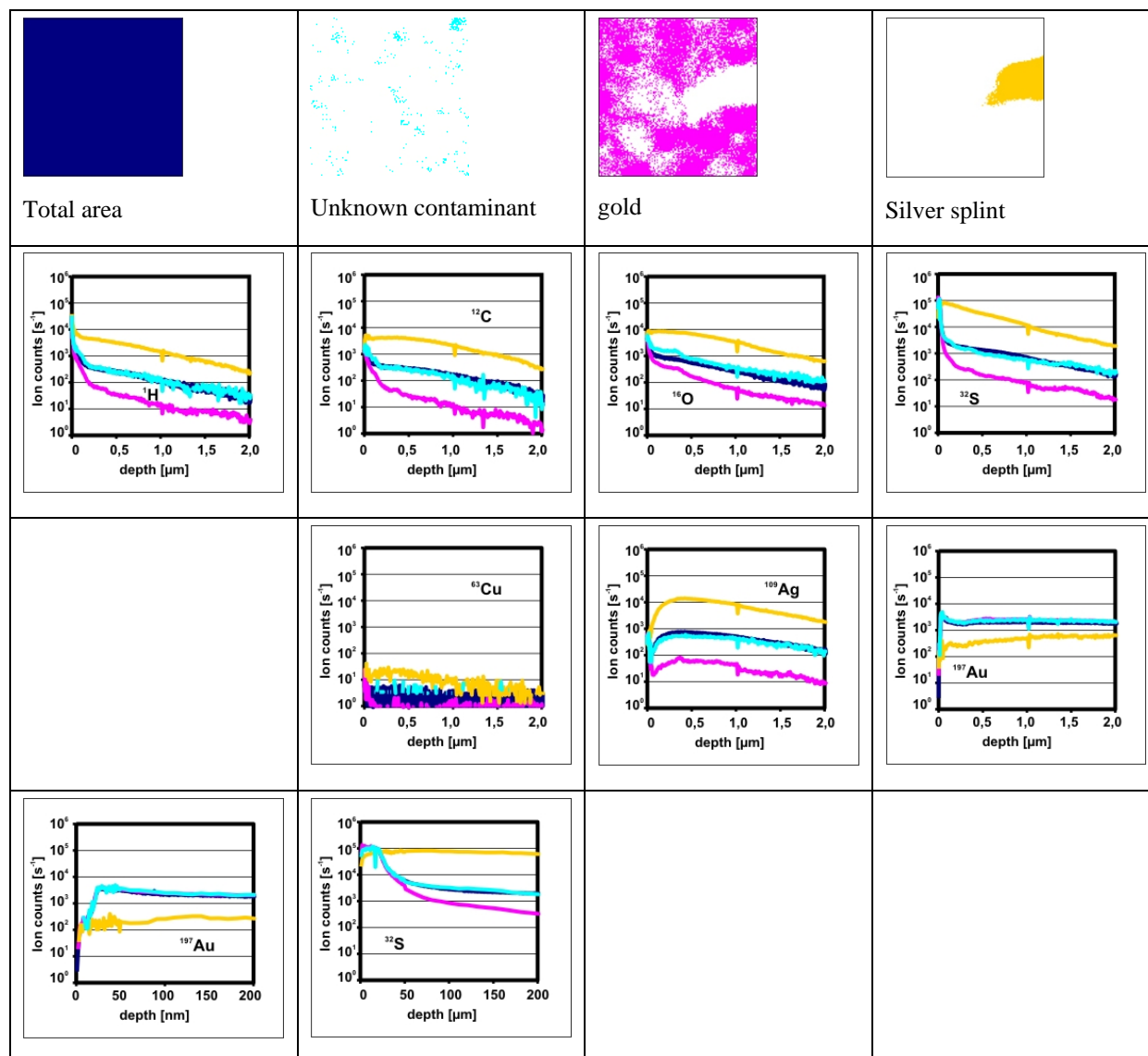
**Figure 87:** Image series of test-coin Ag1, from top to bottom depth is rising; all images are taken from scan 60116; visible image area is  $189.1 \times 189.1 \mu\text{m}^2$ ; each image is a sum of 100 measurement cycles (each point has an information depth of 100 bit); this was the first depth profile of the measurement campaign, sputter depletion velocity was much higher than in all other profiles, there was no electron gun in use.

This is one of the sampled test-coins. At this very coin, splints are made up of pure silver. The coin was treated with  $K_2S_x$  for an hour similar to those coins of the first SIMS measurements (see chapter 4.2.1 Investigations with dynamic SIMS).

There are not as much remarkable things in this depth profile. At the surface there are some impurities visible besides the silver splint. Silver itself is not visible in the top layers. This may be caused by a matrix effect at the beginning of the depth profile (no caesium is at the surface, although the information is taken from the first 100 cycles, where caesium has bombarded the 9 times) or the contaminant elements are covering the silver splint itself. In the homogeneous areas the contaminant elements quickly fade away and concentrate at the silver splint. At the end of the profile the contaminant elements are lightly enriched at the edges of the splint (?), probably there is a non-corroded silver core within the splint. In the last two images of gold there is a weird shade in the upper left part of the image. Both from images and from depth profiles, there is no clue, what this shade has been brought on by.

In the depth profiles the contaminants concentrate within the silver grain again. Their fading lasts much longer than in the previous discussed depth profiles. As expected, there is no copper in this coin. Remarkable are the signals of sulphur and gold near the surface. In the gold, sulphur is dropping quickly (within 50 nm) for about 2 powers of magnitude. This seems to be the sulphur coverage discovered in the first measurement series with dynamic SIMS (see chapter 4.2.1 Investigations with dynamic SIMS).

**Table 6:** processed data of scan 60116; images in the first row show the areas where the depth profile data is excerpted from (colours are chosen according to the colour of the graphs in the depth profiles below. Each depth profile represents the approach of a single mass signal at these different spots. All depth profiles are normalized to counts per second of the whole area. Two additional depth profiles at the bottom show the distribution of gold and sulphur in a smaller depth range.



## Scan 60124 - 60125 at Coin AgCu2

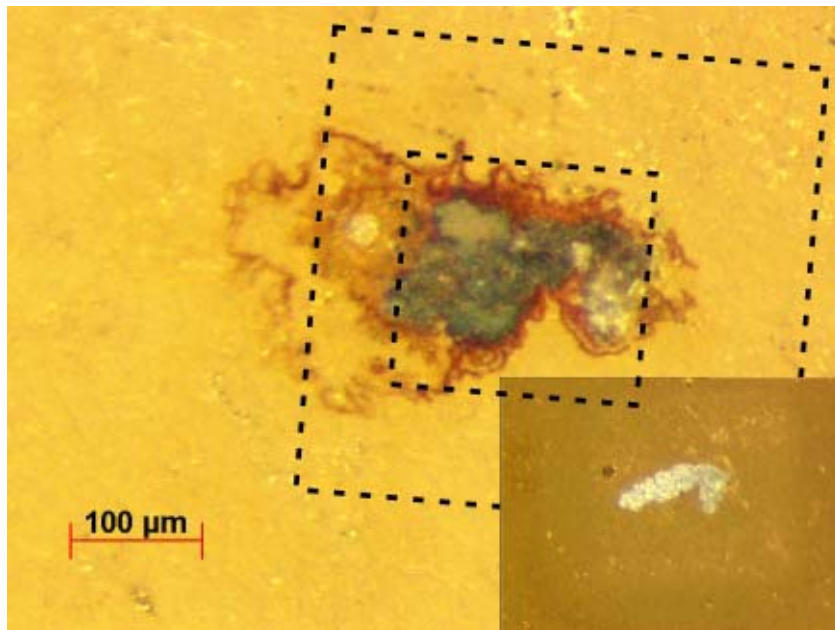


**Figure 88** Measurement spot on test-coin AgCu2. Outer line represents the full ablated area, inner line the imaged area. In the lower right corner a microscope image of the situation after SIMS measurement).

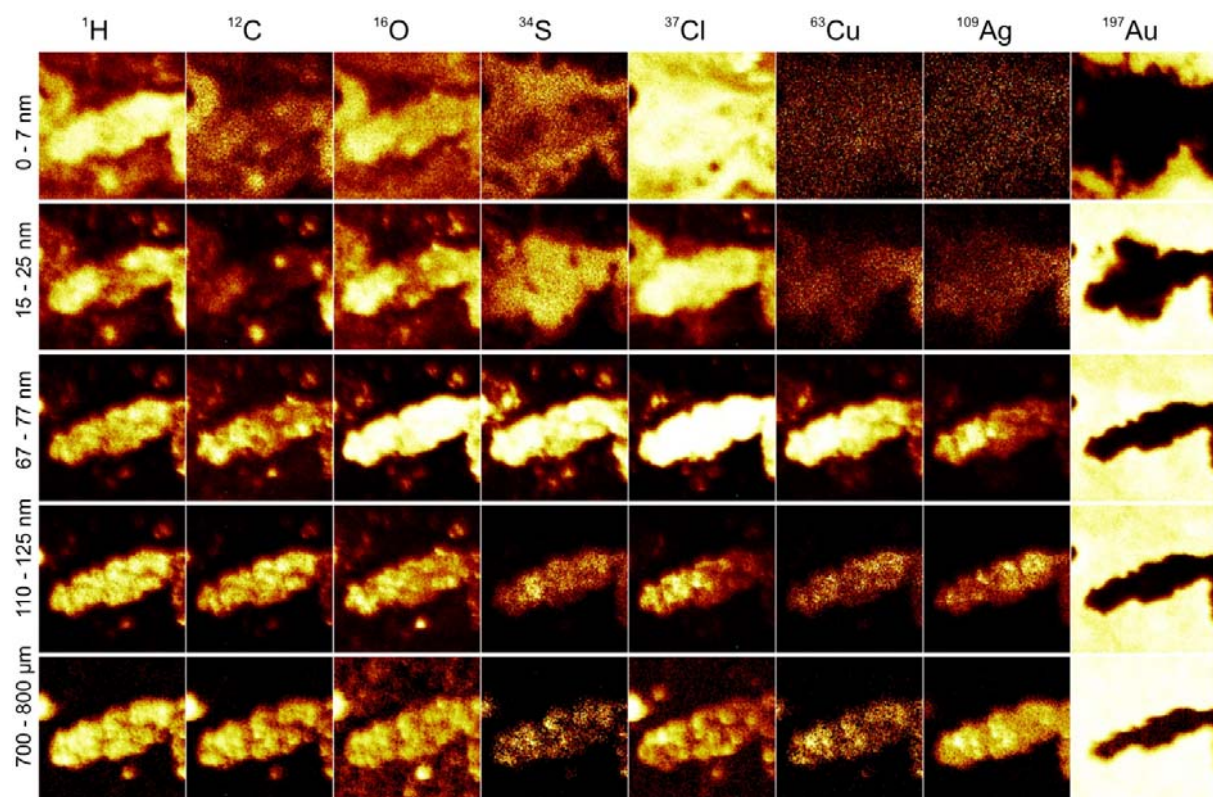
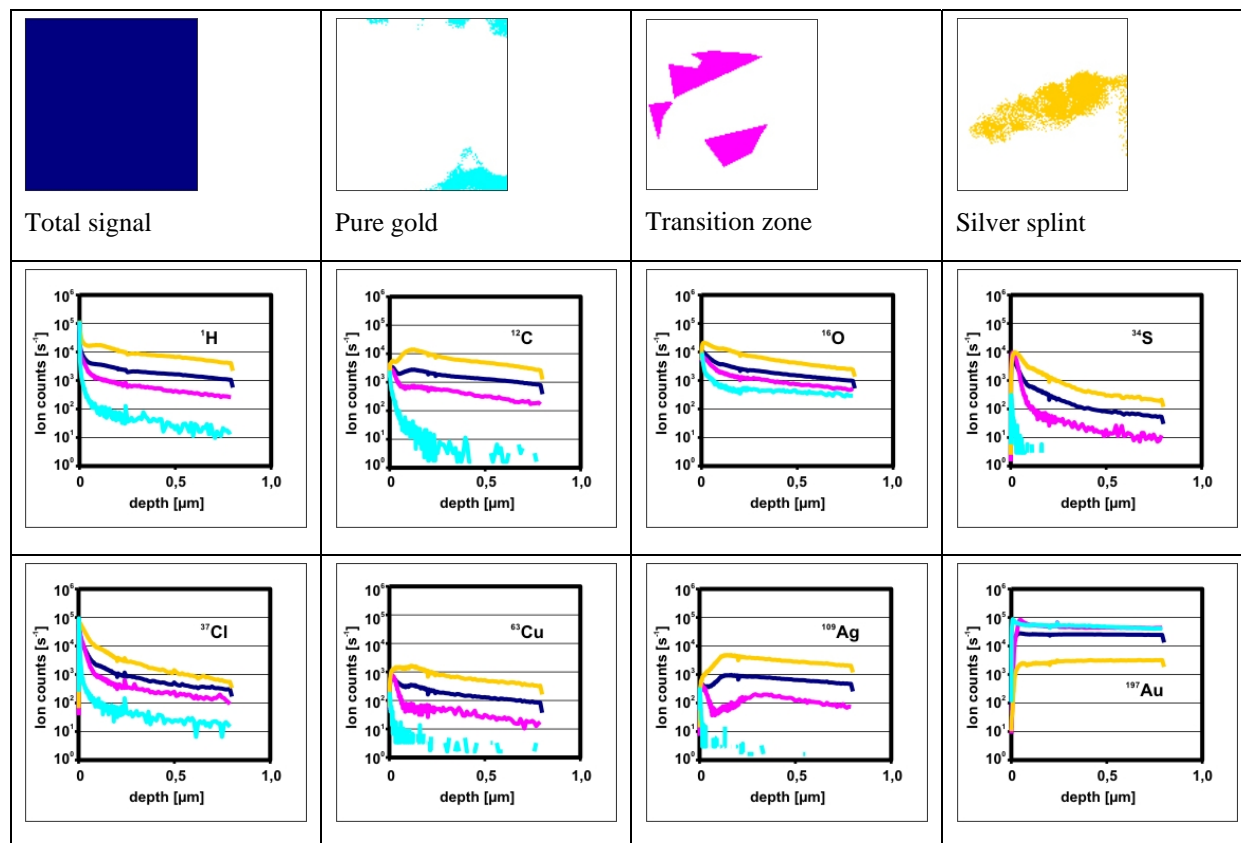


**Figure 89:** Image series of test-coin AgCu2, from top to bottom depth is rising; all images except the last row are taken from scan 60124, last row is from 60125; visible image area is  $189.1 \times 189.1 \mu\text{m}^2$ ; each image is a sum of 100 measurement cycles (each point has an information depth of 100 bit).

**Table 7** processed data of scan 60124 and 60125); images in the first row show the areas where the depth profile data is excerpted from (colours are chosen according to the colour of the graphs in the depth profiles below). Each depth profile represents the approach of a single mass signal at these different spots. All depth profiles are normalized to counts per second of the whole area.



This is a measurement of the second test coin, AgCu2. As the name implies, its splints are made up of a silver copper alloy. Similar to Ag1 it was treated with  $K_2S_x$  for an hour to generate corrosion. Splints on this coin were much smaller than on coins seen before. So we were able to sample a whole corroded area.

In the mass resolved images (see figure 89) the centred splint is clearly visible. In the images of the surface some elements (especially carbon, sulphur, chlorine and the silhouette of gold) picture the corrosion distribution visible in the microscope image (figure 88). Although the corroded transition zone is very dark in the microscope images, most signals are fading away after about 50 nm. This and the fact, that there is a wide clearance in the gold signals, points out a compact coverage of  $Ag_2S$ . The distribution of silver in the uppermost layers supports this theory. Copper and silver are uniformly distributed at the surface and still visible in the second image series (15 - 25 nm). In deeper regions most contaminant elements are concentrated within the splint. The distribution within the splint is more uniformly than in the previous scan of coin Ag1. Probably this splint is due to its size more crannied and thus more corroded.

Again in the depth profiles is a surface coverage of gold by sulphur visible (especially in the zone of pure gold, but also in parts of the transition zone).

### Scan 60126 - 60127 at Coin AgCu2

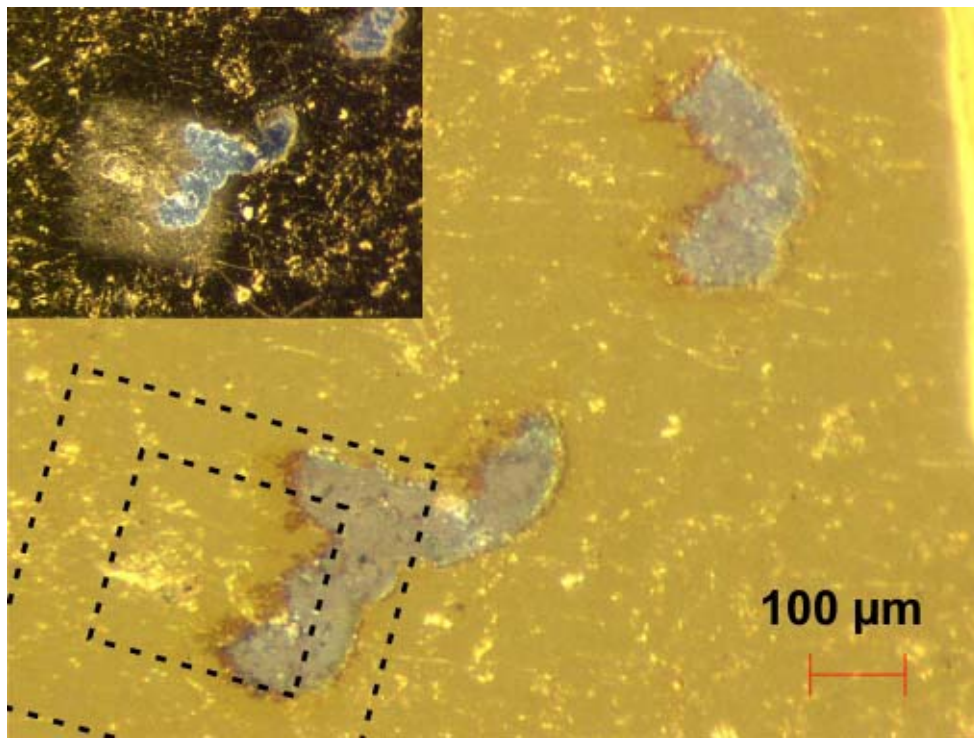


**Figure 90** Measurement spot on test-coin AgCu2. Outer line represents the full ablated area, inner line the imaged area. In the upper left corner a microscope image of the situation after SIMS measurement).

A second measurement at test-coin AgCu2. This spot is chosen due to its lack of a visible corrosion patina. Mass images (figure 91) confirm this. The splint is visible in deeper regions at the silver image (and the negative of the gold image). The transition zone therefore consists of a small band in the centre of the image. It can be seen best in the distribution images of chlorine at the surface, where it is emphasized against the splint border to the right and the gold surface to the left. In this area are also remarkable amounts of hydrogen, carbon and last but not least copper! Contrary is the distribution of oxygen, which is concentrated at a spot within the gold area and also at the silver splint, in deeper regions it becomes more allocated. There seems to be an impurity containing mostly hydrogen, carbon and oxygen, pointing to an organic pollutant at the surface. Copper is other than silver also located within the transition



zone. One prominent copper splint was investigated in the depth profiles (see Table 8). Chlorine is more distributed like carbon and hydrogen in the deeper regions, also a hint to organic compounds. Sulphur is mostly covering the silver splint. Also at the copper particle in the depth profile is sulphur detectable. This particle is fading away with the transition zone as can be seen in the depth profiles. At the end of the depth profile (see last row of images) wider parts of the silver splint are free of any trace element. Sulphur is situated at some edges, chlorine is still more similar distributed to hydrogen and carbon, and oxygen still covers the surface in an uneven distribution. The silver splint core must be free of corrosion.

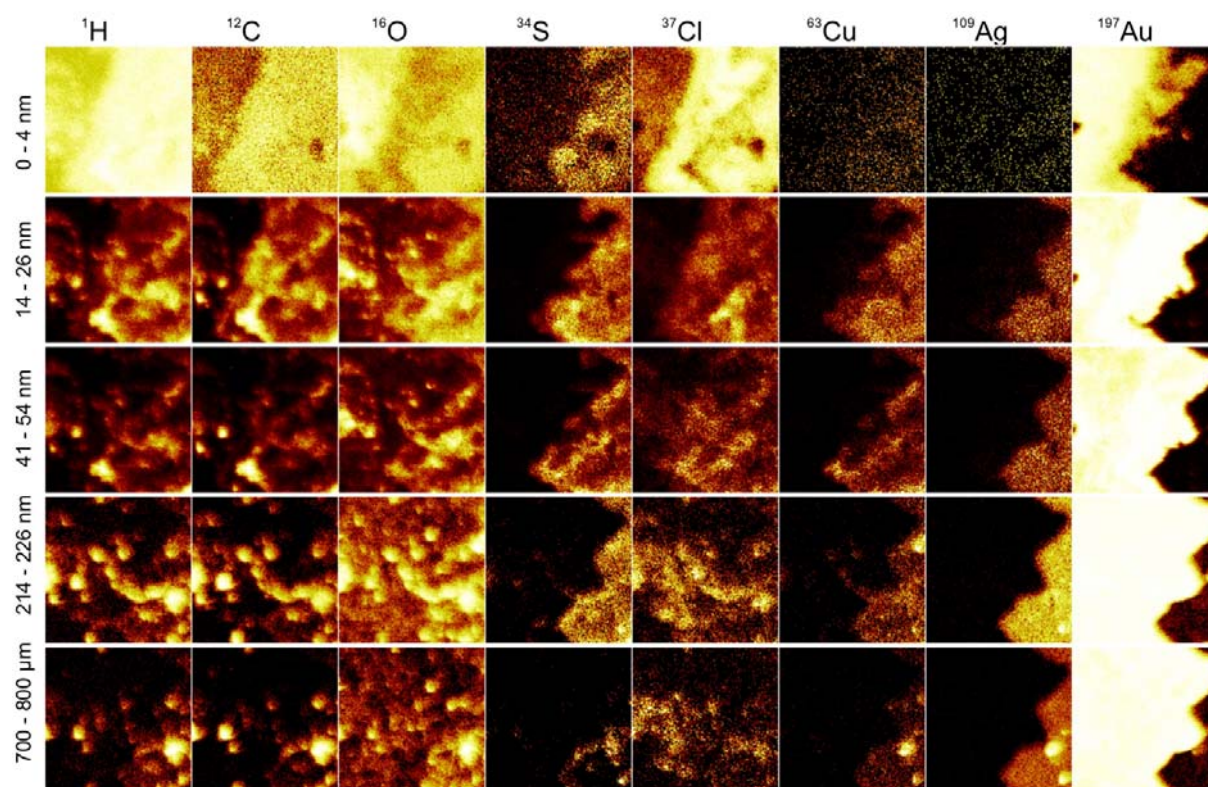
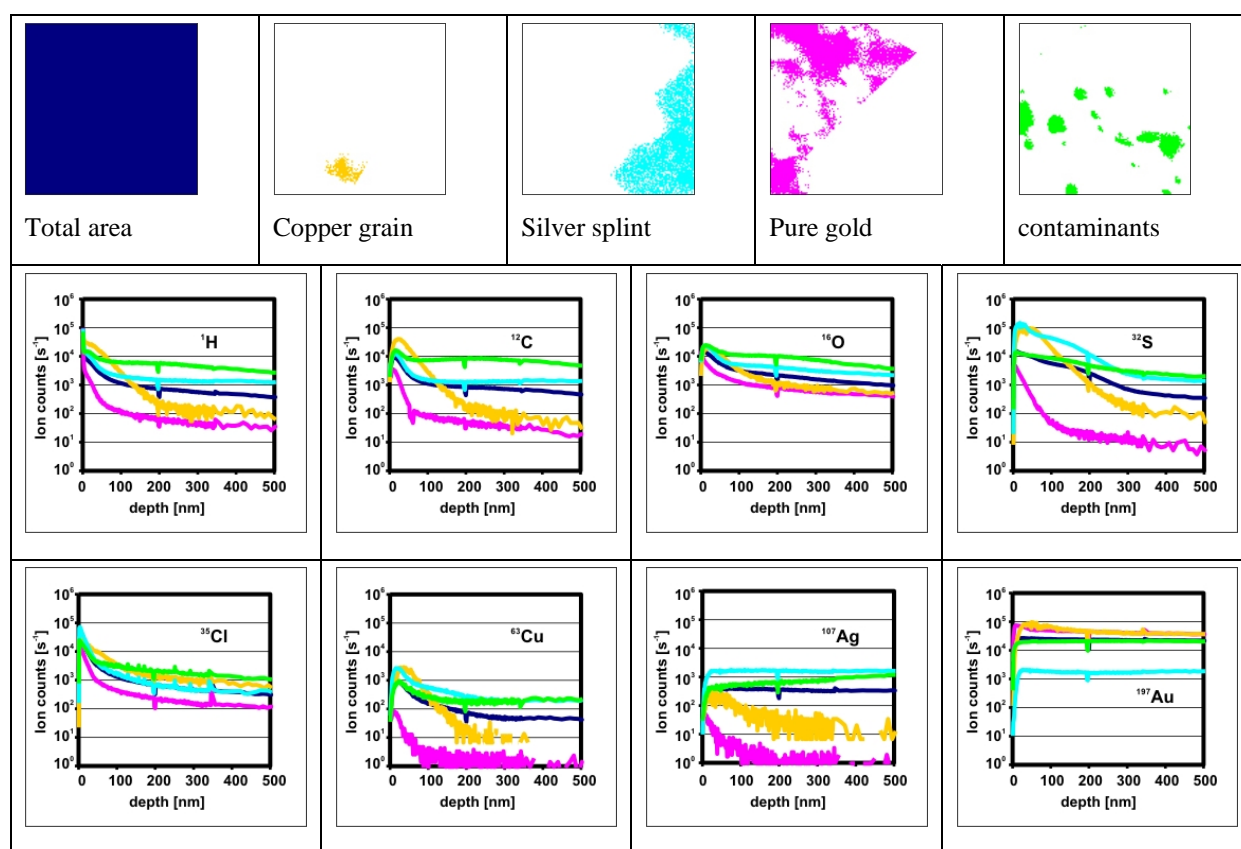


**Figure 91:** Image series of test-coin AgCu<sub>2</sub>, from top to bottom depth is rising; all images except the last row are taken from scan 60126, last row is from 60127; visible image area is 189.1x189.1 μm<sup>2</sup>; each image is a sum of 100 measurement cycles (each point has an information depth of 100 bit).

In the depth profiles these areas are as well documented. In the pure gold, most trace elements drop down within 100 nm. In the transition zone, represented by the copper grain, this drop down lasts over 200 nm, but as well reaches a lower limit (probably this limit is higher due to the nearness to the silver splint). In the silver splint itself, most signals drop within about 200 nm and then reach a level much higher than in the transition zone or in the copper grain. Maybe this is caused by the pollutant grain residing within the silver area. The drop of sulphur last a little bit longer, only after 300 nm it reaches a temporary level, but drops further, but

much slower now. Interesting is the “contaminant” area signal. Most contaminant elements are extremely high, and start to drop after about 300 nm, but silver behaves completely contrary. It starts rising after 300 nm! This is due to the beginning depletion of the pollutant grain residing within the silver grain. It has covered the silver, which now, after 300 nm sputtering, rises, when the pollutant grain starts fading.

**Table 8:** processed data of scan 60126 and 60127); images in the first row show the areas where the depth profile data is excerpted from (colours are chosen according to the colour of the graphs in the depth profiles below. Each depth profile represents the approach of a single mass signal at these different spots. All depth profiles are normalized to counts per second of the whole area.



### 4.2.3. Conclusion on the gold research

Both dynamic and static SIMS were able to show the distribution of the most interesting elements sulphur, oxygen, copper, silver and gold as well as carbon and hydrogen. With the better depth resolution of static SIMS, we were able to outline layers of down to 5 nm at the surface. Comprehensive raw data enabled the interpretation and visualisation also of certain spots of the surface. Other than expected the lateral resolution was almost similar, in TOF SIMS only about a factor 2 better (approximately 1  $\mu\text{m}$  in respect to 2  $\mu\text{m}$  in dynamic SIMS depth profiles). Although the mass resolution is much better with static SIMS, there were still some interferences at important masses (most prominent was an unknown interference at mass 107 with  $\text{Ag}^{107}$ , that's why mostly  $\text{Ag}^{109}$  was investigated). But much more disadvantageous is inability of changing the energy distribution of the detected secondary ions. Only ions with approximately zero kinetic energy (at their origin) were detected. Such ions are effected by a high matrix effect. In dynamic SIMS, it is possible to shift the ion energy (offset) when recording depth profiles, which will weaken the signal, but due to the higher sensitivity of dynamic SIMS, most signals are still higher than TOF SIMS.

Concluding, the TOF SIMS measurements were better due to time management (similar information is gathered in fractional amount of time. The high mass resolution is a big plus for TOF-SIMS but is balanced by the lower matrix effect and the higher sensitivity in dynamic SIMS, when measuring depth profiles. In imaging mode, TOF SIMS really beats the pants off of dynamic SIMS. The high safety of the compound identity due to the high mass resolution and the ability of qualitative information at each pixel is only damped by the low sensitivity (copper for instance was in TOF SIMS at the limit of detection, when dynamic SIMS still had a power of magnitude signal, but it was not safe whether this is 100% copper or an interference. Besides the higher sensitivity, one more advantage of dynamic SIMS is mentionable: the data analysis with TOF SIMS takes much longer than with dynamic SIMS. Therefore TOF SIMS is, in my opinion the future technology, but nevertheless, dynamic SIMS will still have its area of application.

For the Coin analysis, both studies have revealed that sulphur as well as chlorine is most prominent in the corrosion. It is also shown in some examples that the visible corroded area is mostly caused by silver (XPS studies have shown  $\text{Ag}_2\text{S}$  at the surface). In the test coins this corrosion sometimes includes the whole splint, sometimes only a few 100 nm are effected by corrosion and the rest of the splint is still metallic. Once only weak corrosion was visible, at

this splint, very much organic material has been found. Probably a closed organic film prevented this area from corrosion. In the ancient coins all investigated splints were completely corroded. The sulphur layer at the pure gold surface is much smaller than in the ancient ones, but there are much more grain-sized impurities at the surface containing hydrogen, carbon, chlorine and also sulphur. These grains are bigger than those seen at the test-coins. In depth profiles, the signal drop of these signals lasts very long (similar to dynamic SIMS depth profiles, where only an average signal of the whole area was detectable).

Results of this topic have been published twice (only concluding dynamic SIMS results).

See Chapter **5.9 Investigations of corrosion phenomena of gold coins with SIMS** and **5.10 Brown spot corrosion on historic gold coins and medals**. Further publications are in progress.

### **4.3. SIMS profile analytics attending research on implantation simulation**

When secondary ion mass spectrometry became a widely used technique in the 70s, the most important field of application was in the semiconductor research and development, here especially implantation analysis.

Implantation is one of the most important tools in the field of semiconductor fabrication. It enables the introduction of trace elements in a wide range of concentration from ppb to the percentage level [57].

In implantation ions are accelerated onto the surface material (usually a semiconductor like silicon or gallium-arsenide). The implantation depth is set by the ion acceleration voltage. Voltages of about 10 keV (~5nm!) up to several MeV (~1  $\mu\text{m}$ ) are usual. For highest implantation energies complex ion accelerators are necessary, thus in industrial field the upper limit is lower. Additionally most implanters allow a mass separation during acceleration, which enables the implantation of single isotopes.

The implantation profile shape is commonly a twisted gauss distribution curve [58]. When implanting the ions in direction of a lattice plane of the substrate material, the mean implantation depth becomes deeper, caused by channelling of the ions along the lattice planes. Out of plane implantation normally uses a 7° implantation angle, avoiding channelling planes. Nevertheless channelling implantation is interesting when implantation into deeper regions with lower energies is required or when a broadened profile should be implanted within one step combining implantation in and out of plane.

The mechanism of implantation is very similar to secondary ion mass spectrometry. Thus when secondary ion mass spectrometry first came up, it was the method of choice for semiconductor application. With a depth resolution of down to 10nm (later on reduced further) it was able to resolve implantation profiles with highest accuracy at low detection limit. The highly defined systems in semiconductor field also easily allowed the fabrication of quantification standards (mostly also using ion implantation).

With the advancing ability of data processing and increasing knowledge of the implantation process nowadays most analytics is replaced by process simulation. The widest distributed simulation program, SRIM (“stopping and range of ions in matter”) [43], bases on a Monte Carlo algorithm. It allows the calculation of the distribution of implanted elements of the

whole periodic system into substrates of widely changeable composition. Several parameters like acceleration voltage, angle, ion mass (isotopes!), substrate composition and density are idle. This program provides not only information on parameters of the implantation shape, but also things like particle recoil, surface sputtering yield, phononic energy and more. Disadvantage is the steady state of the substrate, not considering deposited or ablated atoms. As well it always calculates out of lattice plane implantation; it is not able to consider channelling (nevertheless, there are more complex applications available, considering channelling).

Most commonly used simulation routines bases on models of Ziegler et al [59,60]

### 4.3.1. Research on Erbium implantations

The distribution of implanted elements can be characterized by 4 forming factors describing the curve shape:

$$R_p \text{ (mean ion range): } R_p = \int_{-\infty}^{\infty} x f(x) dx \quad \text{(equation 8) [57]}$$

$$\Delta R_p \text{ (straggle): } \Delta R_p = \sqrt{\int_{-\infty}^{\infty} (x - R_p)^2 f(x) dx} \quad \text{(equation 9) [57]}$$

$$\gamma \text{ (skewness): } \gamma = \frac{\int_{-\infty}^{\infty} (x - R_p)^3 f(x) dx}{\Delta R_p^3} \quad \text{(equation 10) [57]}$$

$$\beta \text{ (kurtosis): } \beta = \frac{\int_{-\infty}^{\infty} (x - R_p)^4 f(x) dx}{\Delta R_p^4} \quad \text{(equation 11) [57]}$$

As described in this chapter's introduction, this curve shape is dependent on the dopant element, the substrate composition, the implantation energy and angle. Computer programs are able to simulate the implantation process well. Most simulations base on implantations of light elements (hydrogen, helium, lithium) into silicon. Heavier elements are calculated similar using a correction term considering the changed properties of these elements. This correction term has been established with only a few elements (e.g. Au in Si). Our study

concentrated on the element erbium, a rare lanthanide earth element. Erbium doped semiconductors are approved light emitter in the range of 1.54  $\mu\text{m}$ , suitable for laser- and diode applications.

Investigations in our group in 2000 [61] revealed a mismatch of common simulations and measured implantation of up to 20% although SRIM guarantees a precision of better than 10% for heavy ions. A new sample series was manufactured in 2001. It contained 6 samples consisting of a SIMOX substrate with a defined Si/SiO<sub>2</sub> interface depth of 217.7 nm (specified with ellipsometry). Erbium has been implanted with energies of 100 keV, 200 keV, 300 keV, 400 keV, 500 keV and 600 keV respectively and an overall dose of  $3 \times 10^{14}$  atoms/cm<sup>2</sup>. The well defined interface should be used as a depth calibration, thus avoiding incorrect profilometer depth evaluation.

First SIMS measurements of these samples were rejected by the manufacturer. The results had a bad mismatch with former studies and also with their internal, self developed simulation program [62].

In 2003 a second measurement run was started, this time with special attention on the stability and reproducibility of the measurement. This time the analysis was concentrated on the part of the implantation in the upper silicon layer (217.7 nm). All samples were measured three times and were stopped at the interface. Additionally the number of data points was raised in the depth profiles, to enable a better fitting of the line shape and setting of the depth scale.

Actually the depth scale was the most important topic of discussion afterwards. This discussion is also described in the paper “**Range evaluation in SIMS depth profiles of Er-implantations in silicon**” (see chapter 5.6).

It describes the application of correction terms in the evaluation of the interface position in the depth profile and the correction of the sputter velocity at the beginning of the depth profile. Latter was most important, the mismatch of a linearly applied depth scale to the results from simulations were up to 7 nm near the surface. The mismatch is caused by a none-equilibrium state of the sputter process within the first nanometers. Similar to implantation also sputtering primary ions get implanted into the sample several nanometers (used O<sub>2</sub><sup>+</sup> ions for instance approximately 7 nm). The sputter equilibrium is reached, when the number of primary ions penetrating the surface and primary ions getting ablated equals. Our simulations stated the equilibrium state at about 20 nm with a maximum depth scale mismatch at this point of 7 nm. Regarding this results, SIMS depth profiles match simulation results better than those results from the first investigation described in [61]. Still there is a mismatch of about 5%, which has by now not been published. A RBS-study with the same samples was done afterwards, the

results were together with the SIMS results introduced for publish, but rejected. By now the project coordinators are planning new tests, which are able to proof our results.

### **4.3.2. Simulation of boron channelling**

As described in the previous chapter is the angle of penetration essential for the implantation profile and depth. Ordinary implantations are done out of crystalline plane of the used substrate. Implanting ions in direction of a crystalline plane causes an effect called channelling, where implanted atoms are gliding along the crystalline planes much deeper than expected. Formerly common industrial applications try to avoid this effect due to this effect was not well predictable. Besides common implantation parameters, channelling is strongly dependent on the crystalline damage. So during implanting ions, the channelling ability of a substrate will change drastically. Modern simulation routines like IMSIL [62] try to consider this effect in order to enable a correct simulation profile of channelling implantations.

In order to verify results from such a simulation, SIMS measurements were initialized. More precisely the influence of the damage of a previous nitrogen implantation on a subsequently done boron channelling implantation should be investigated.

Samples consisted of (110)-Si substrates. They were predamaged with 30 keV N<sup>+</sup> ions with a tilt angle of 10° and a total dose of 3x10<sup>14</sup>cm<sup>2</sup>. The implantations were done at room temperature with ion currents between 1.6 and 800 nA/cm<sup>2</sup>. One sample was bombarded at liquid nitrogen temperature with an ion current of 160 nA/cm<sup>2</sup>. The temperature rise during implantation was estimated to be less than 6° C using a thermocouple on a reference sample. Only one half of each sample was predamaged, the other half was covered by a thin steel sheet during bombardment and kept undamaged. All samples were then implanted at room temperature with 30keV B<sup>+</sup> at a dose of 10<sup>13</sup>cm<sup>2</sup> in [110] channelling direction.

In image 92 an exemplary depth profile of a sample with a N-implantation with 160 nA/cm<sup>2</sup> ion current. In figure



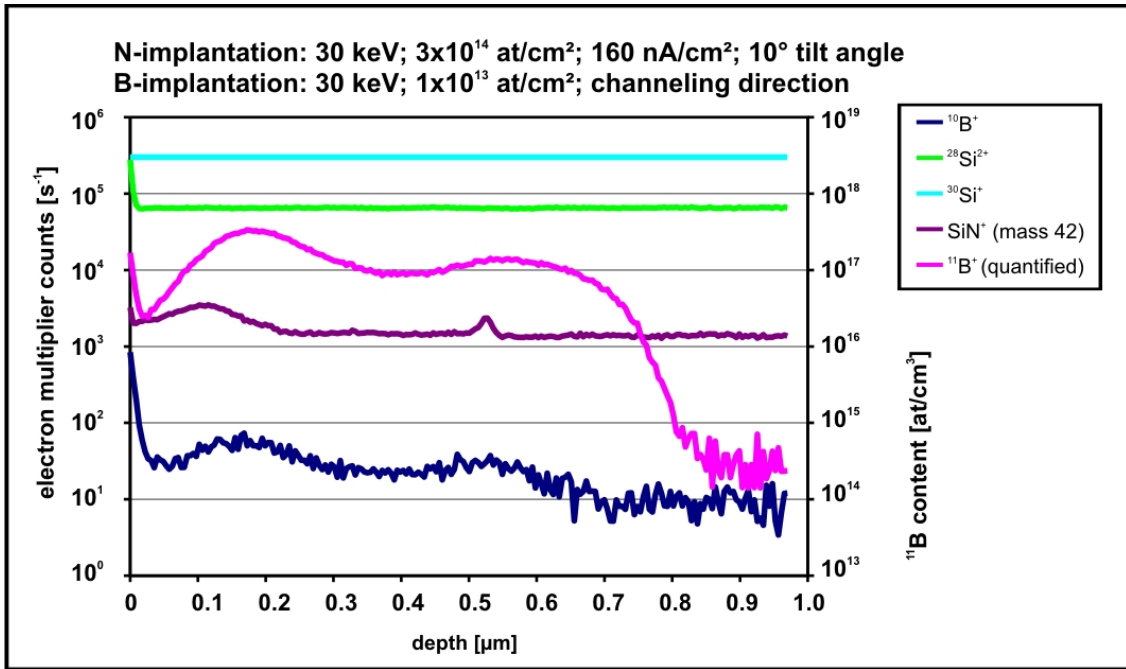


**Figure 92:** Example for a boron implantation profile of this investigation series; used device settings:  $O_2^+$  primary ions; 5.5 kV energy, 450 nA beam dose, 150  $\mu\text{m}$  analyzed area diameter, 350  $\mu\text{m}$  scan diameter.  $^{30}\text{Si}^+$  and  $^{28}\text{Si}^{2+}$  are matrix reference signals for primary ion dose adjustment;  $^{10}\text{B}^+$  was additionally measured to testify the implantation quality,  $\text{SiN}^+$  (measured at mass 42) is an indicator for the nitrogen implantation, the  $^{11}\text{B}^+$  signal is quantified with an homogeneous B-standard.

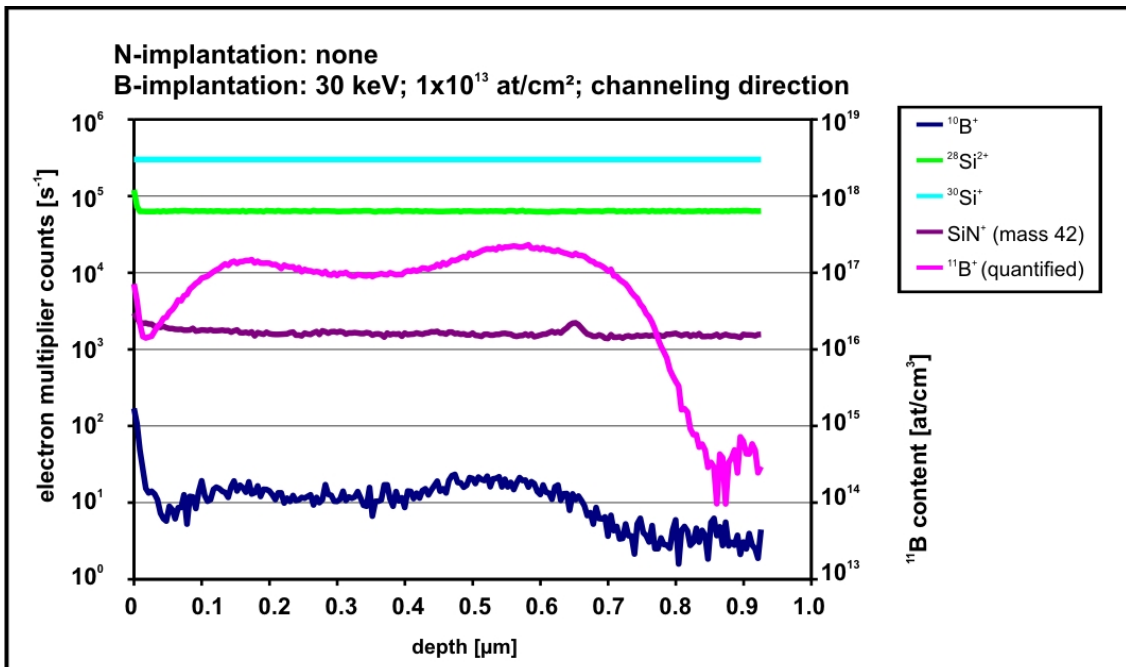
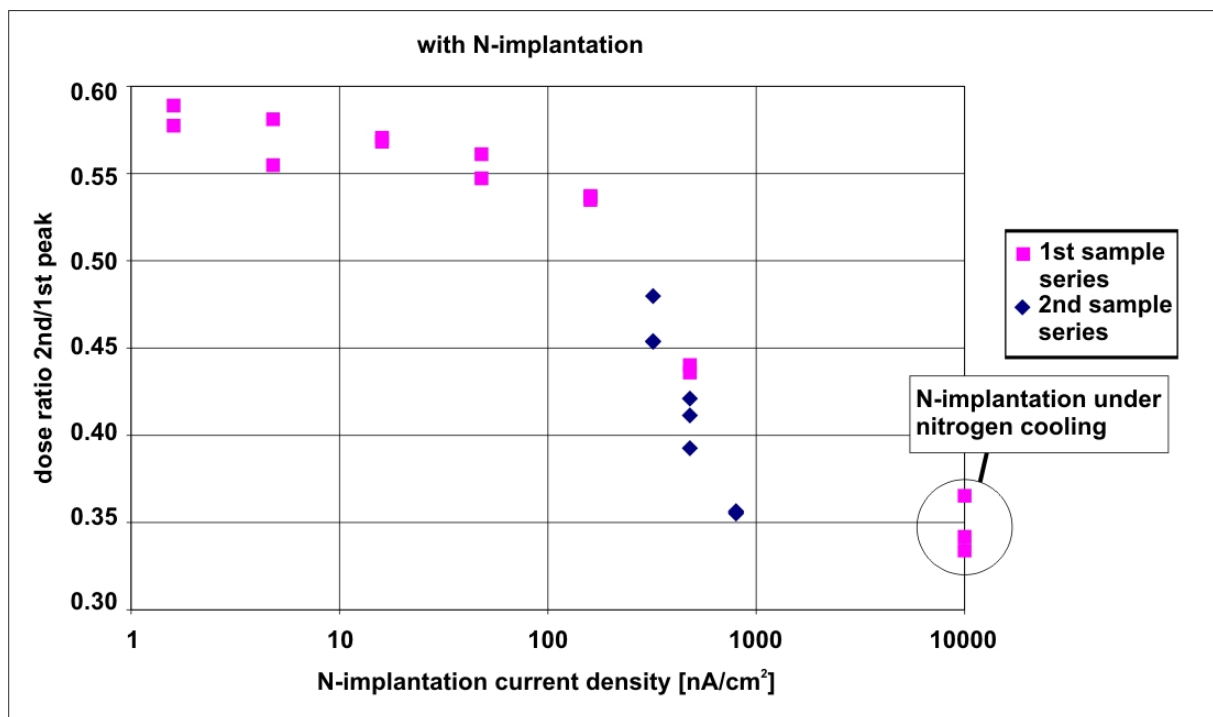


**Figure 93:** Same sample as shown in figure 92, at this spot no nitrogen has been implemented. Used device settings:  $O_2^+$  primary ions; 5.5 kV energy, 450 nA beam dose, 150  $\mu\text{m}$  analyzed area diameter, 350  $\mu\text{m}$  scan diameter.  $^{30}\text{Si}^+$  and  $^{28}\text{Si}^{2+}$  are matrix reference signals for primary ion dose adjustment;  $^{10}\text{B}^+$  was additionally measured to testify the implantation quality,  $\text{SiN}^+$  (measured at mass 42) is an indicator for the nitrogen implantation, the  $^{11}\text{B}^+$  signal is quantified with an homogeneous B-standard.

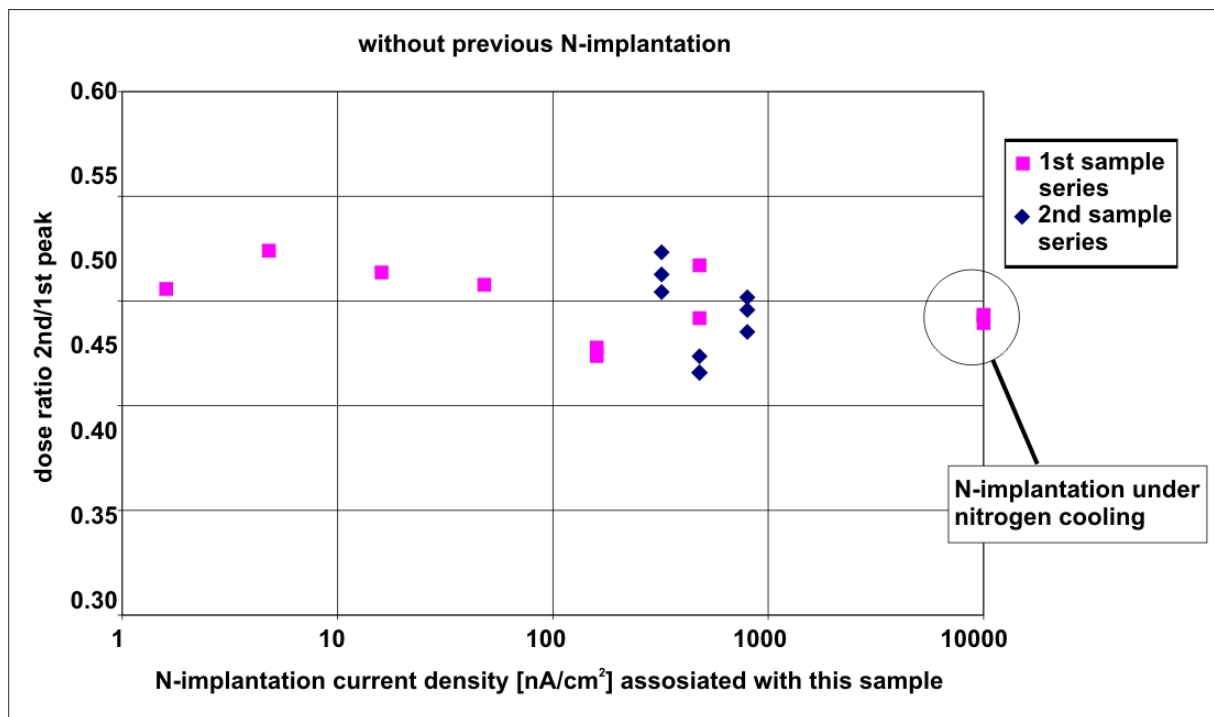
Most important task of this study was the ratio of material deposited in the front part and the deeper channelling region. Samples were measured in two series, in the first one the maximum implantation current of nitrogen was only 480 nA/cm<sup>2</sup>; in a second run also additionally samples with 800 nA/cm<sup>2</sup> were added. Due to the minimal differences in the samples, each sample was measured several times.

Image 94 shows the ratios of the peak integrals of the depth profiles with nitrogen implantation. As predicted from simulation, there is a maximum ratio at low implantation dose with approximately 0.75, then a drop down area above 100 nA/cm<sup>2</sup> and (not confirmed with this investigation) a minimum ratio at approximately 0.35. Latter value is testified by the additional sample implanted under nitrogen cooling. At this temperature all relaxing mechanisms are blocked. Image 94 shows the ratios of the same samples, this time the very side without implantation. Although, all samples should equal, the ratio varies for about 10%. But this is still sufficient for the interpretation of figure 94.

Simulation failed in one important point: It underestimates the channelling peak, i.e. it overestimates the implant damage. The position of the transition area was predicted to be shifted to much lower values. Reasonable interpretations for this mismatch have not been found yet.



**Figure 94:** Ratios of peaks of the boron curve in the depth profiles of samples with nitrogen implantation. The 1<sup>st</sup> peak is the normal implantation peak; the 2<sup>nd</sup> one is the channelling peak (the stronger the channelling, the higher the ratio!). Relative variation of the ratio is about 10% (concluded from the variation of values in figure 95).



**Figure 95** Ratios of peaks of the boron curve in the depth profiles of samples without nitrogen implantation. The 1<sup>st</sup> peak is the normal implantation peak; the 2<sup>nd</sup> one is the channelling peak (the stronger the channelling, the higher the ratio!). All depth profiles should equal, but due to differences in the implantation and the measurement there is a variation of these values of approximately +/- 10%.

A detailed discussion and interpretation can be found in those two publications on this topic, written in cooperation with this thesis:

Chapter 5.5: **Dose-rate dependence of damage formation in Si by N implantation as determined from channelling profile measurements** and chapter 5.7 **Multiscale approach for the analysis of channelling profile measurements of ion implantation damage.**

#### 4.4. Quantification of oxynitride layers by evaluation of $\text{MCs}^+$ secondary ions

Quantification always is a very complex task for SIMS. The dependence on standards with as close composition to the sample as possible inhibits wider application. Only alternative is the reduction of the matrix effect by using  $\text{MCs}^+$  molecular secondary ions (where M is the analyte and Cs stems from the primary ions). The use of these ions was first suggested in the early 90s [63,64]. This technique was then seized in a PhD Thesis by Sabine Dreer at our institute [65] for the quantification of oxynitride layers of the elements silicon and aluminium. In a first series of investigations using NRA (nuclear reaction analysis) and RBS (Rutherford Backscattering Spectrometry) a batch of some PVD deposited standard layers was created [66]. Thereafter these standards were characterized with EPMA (Electron Probe Micro Analysis), SIMS, hf-SNMS (Secondary Neutral Mass Spectrometry), hf-GD-OES (Glow Discharge Optical Emission Spectrometry) and FT-IR (Fourier Transform – Infrared Spectroscopy) [67,68]. SIMS investigations revealed an exponential dependency of the RSF values only of the oxygen content of the sample (therefore independent on the nitrogen content), see also figure 96.

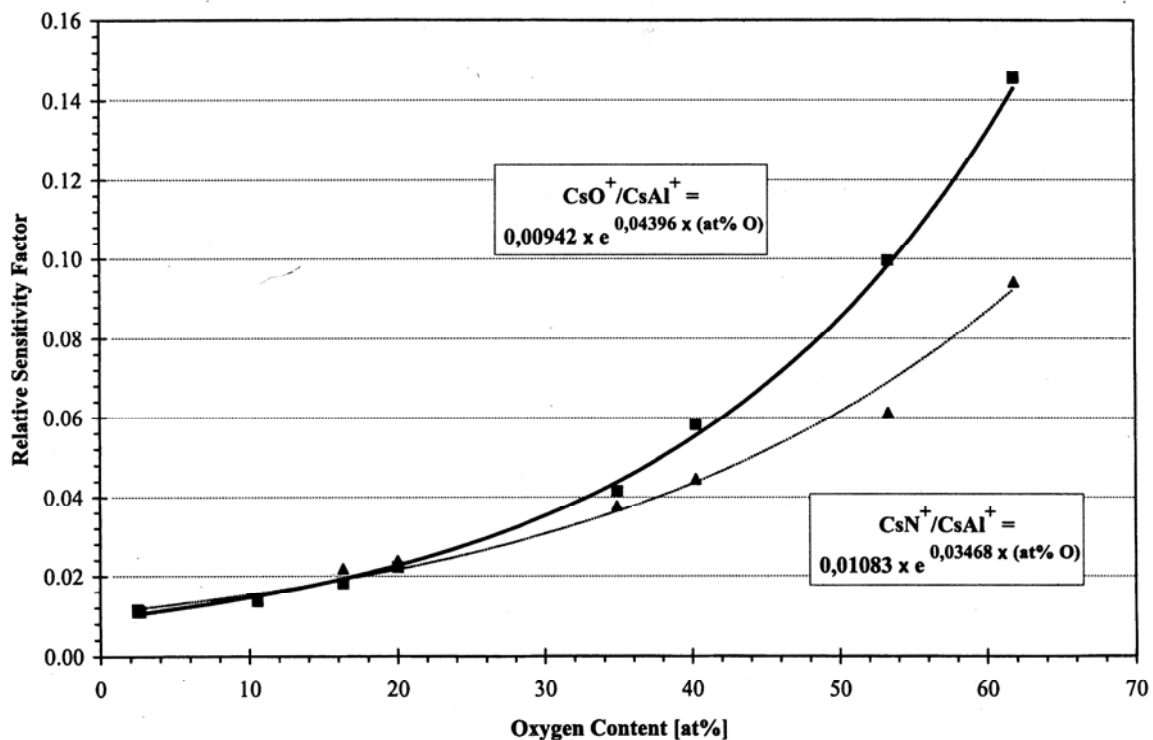


Figure 96: Exponential dependency of some RSF-values on the oxygen content in aluminium samples

Due to these results are all acquired with the SIMS device at hand, they enable further SIMS investigations without any standard in high defined metal/nitrogen/oxygen systems (metal was at first silicon and aluminium, later on also chromium, tantalum and molybdenum were tested, these results are still restricted for publishing).

One of these tasks completed during this PhD thesis was the analysis of the aging of TFT-LCD panels. The investigated TFT-LCDs consisted of a gate electrode multilayer structure starting with a glass substrate, followed by molybdenum-tungsten or molybdenum capped aluminium-neodymium,  $\text{SiO}_2$ ,  $\text{SiO}_x\text{N}_y$ ,  $\text{Si}_3\text{N}_4$  layers. This near stoichiometric oxynitride system tends to charging during measurement. A charge compensation routine unique for our instrument enabled the measurement without electron flood gun. It uses data of an energy distribution screening previous to each cycle and shifts the sample high voltage accordingly. The relative standard deviation of the results of this study was within 0.2% for silicon, oxygen and nitrogen, and 1-2% for hydrogen. At a total of 9 samples, it was possible to show a minor gradient of the oxygen content from the edge to the centre of the panel. Additionally the distribution of the metallic components (gate electrode material, glass substrate as possible) was investigated. This revealed an additional problem in the homogeneity of the molybdenum gate electrode. Pinholes in this layer enabled sodium to diffuse from the glass substrate into the gate electrode. These pinholes were not directly detectable with SIMS. Subsequent TEM (Transmitted Electron Microscopy) investigations showed these pinholes in the range of a few 100 nm.

An abstract of the detailed study is presented in chapter **5.8 Quantitative SIMS depth profiling of diffusion barrier gate-oxynitride structures in TFT-LCDs.**

## **5. Publications**

All SIMS measurements described in the following publications are accomplished by the author personally.

## **5.1. Characterization of Cr intermediate layers in Cu-C-system with SIMS method**

Mayerhofer, K. E.; Neubauer, E.; Eisenmenger-Sittner, C.; Hutter, H.  
Applied Surface Science (2001), 179(1-4), 275-280.

### Abstract

In the design of new high speed chip generations, the greatest problem is to bleed off process heat during their operation. The installation of heat sinks onto such chips is necessary. A copper-carbon (Cu-C) composite is one possible material. It combines high thermal cond. with low d. and tailorable coeff. of thermal expansion (CTE). Because of low wettability of carbon by copper, a thin layer of chromium (Cr) has to be deposited 1st to contact copper with the carbon fibers. The optimization of processing parameters was done on vitreous carbon substrates (Sigradur G) as a model for carbon fibers. Onto these substrates, 2 nm chromium and 1  $\mu\text{m}$  copper were deposited. In the later serial fabrication of the composite, a hot pressing step will follow the deposition, which is simulated with a heat treatment of the compd. Secondary ion mass spectrometry (SIMS) studies were done to obtain information on the depth distribution of the main elements copper, chromium and carbon. Two samples, one as deposited and one subjected to a heat treatment after deposition are compared.

### Citations

- 1) Mortimer, D; J Mater Sci 1970, 5, 149
- 2) DeVincent, S; J Mat Eng Perform 1993, 2, 323
- 3) Korab, J; Composites: Part A 1999, 30, 1023
- 4) Korab, J; PhD thesis, TU Wien 1999
- 5) Eisenmenger-Sittner, C; Microchim Acta 2000, 133, 267
- 6) Hutter, H; Mikrochim Acta 1992, 107, 137
- 7) Wolkenstein, M; Fresenius J Anal Chem 1998, 361, 722

## **5.2. Adhesion promotion of Cu on C by Cr intermediate layers investigated by the SIMS method**

Mayerhofer, Karl E.; Neubauer, Erich; Eisenmenger-Sittner, Christoph; Hutter, Herbert. Analytical and Bioanalytical Chemistry (2002), 374(4), 602-607.

### Abstract

Copper-carbon composites are candidate materials for heat sinks for high speed/high-performance electronic components. They combine high thermal cond. with low d. and a tailorable coeff. of thermal expansion (CTE). Because of the low wettability of carbon by copper, a thin layer of chromium can be deposited to promote both the adhesion and the thermal contact of copper with the carbon fibers. Therefore, in a first step layers of Cr and Cu were deposited by magnetron sputtering on plane vitreous carbon substrates (Sigradur G), which serve as a model for carbon fibers. From pull-off-adhesion measurements an interlayer thickness of Cr in the range of 2-10 nm was found to provide the optimal adhesion for 1  $\mu\text{m}$  thick copper overlayers. To model the later serial fabrication of the composite that involves a hot pressing step following the deposition, the C/Cr/Cu samples were heat treated at 800 °C under vacuum for 1 h. Adhesion on the heat-treated samples was superior in comparison to the untreated ones. To obtain information about the adhesion mechanism secondary ion mass spectrometry (SIMS) investigations were done on the depth distribution of the main elements copper, chromium, and carbon. Two samples, one as deposited and one subjected to heat treatment after deposition, were compared in this investigation. We found that heat treatment mainly modifies the distribution of Cr in the C/Cr/Cu system.

### Citations

- 1) Mortimer, D; J Mat Sci 1970, 5, 149
- 2) Mortimer, D; J Mat Sci 1973, 8, 640
- 3) Voitovitch, R; Acta Materialia 1999, 47, 1117
- 4) Anon; Numerical data and fundamental relationships in science and technology, 6th run 1999, IV/2b, 686
- 5) Abel, P; J Mat Res 1994, 9, 617
- 6) Anon; <http://www.srim.org> 2002
- 7) Eisenmenger-Sitner, C; Microchim Acta 2000, 133, 267
- 8) Mayerhofer, K; Appl Surf Sci 2001, 179, 275



### 5.3. Influence of thermal treatment on the adhesion of copper coatings on carbon substrates

Schrank, C.; Schwarz, B.; Eisenmenger-Sittner, C.; Mayerhofer, K.; Neubauer, E. Vacuum (2005), 80(1-3), 122-127.

#### Abstract

Sputter-deposited copper (Cu) coatings on plane glassy carbon (C) substrates serve as a model for the interface between Cu- and C-fibers in Cu-C metal matrix composites (MMCs). This interface is of crucial importance for the mech. and thermal properties of copper-carbon MMCs. If the Cu-coating is deposited on a nitrogen(N)-rf-plasma treated C-substrate at room temp. (RT), the adhesion of Cu to C is excellent. In a further step the Cu-coated C-samples are subjected to a thermal treatment at 800° under high vacuum conditions for 1 h to partially mimic the hot pressing step involved in the prodn. of real MMCs. This thermal treatment generates a recrystn.-induced dewetting process of the Cu coating from the C substrate, which drastically reduces the adhesion of Cu to C. If a molybdenum-intermediate layer is deposited, no dewetting of the Cu-film takes place, although recrystn. occurs. Addnl. the adhesion of the Cu-film is, depending on a min. thickness of the molybdenum layer, low in the as-deposited state and is strongly increased after the annealing step. SIMS measurements indicate that this increase is caused by the formation of molybdenum carbides during the heat treatment.

#### Citations

- 1) Parkasan, K; Composites Part A 1997, 28, 1019
- 2) Korab, J; Composites Part A 1999, 30, 1023
- 3) Mayerhofer, K; Appl Surf Sci 2001, 179, 275
- 4) Zhu, Z; J Mater Sci 1997, 32, 1061
- 5) Wan, Y; Mater Sci Eng A 2000, 288, 26
- 6) Korb, G; Composites Part A 1998, 29, 1563
- 7) Liu, H; ISIJ Int 1989, 29, 568
- 8) Dubgen, R; Glasartiger Kohlenstoff SIGRA-DUR-ein Werkstoff fur Chemie und Technik
- 9) Htw Hochtemperatur-Werkstoff GmbH; <http://www.htw-germany.com>
- 10) Neubauer, E; Thin Solid Films 2003, 433, 160
- 11) Schwarz, B; Master's thesis, Vienna University of Technology 2003
- 12) Srolovitz, D; J Mater 1995, 47, 31
- 13) Schrank, C; Thin Solid Films 2004, 459, 276
- 14) Eisenmenger-Sittner, C; Surf Coat Technol 2004, 180-181, 413
- 15) Warnes, B; J Less-Common Met 1985, 106, 241
- 16) Isobe, Y; J Less-Common Met 1989, 147, 261
- 17) Mayerhofer, K; Appl Surf Sci, in press, doi:10.1016/j.apsusc.2005.02.018

## **5.4. Characterization of molybdenum intermediate layers in Cu-C system with SIMS method**

Mayerhofer, K. E.; Schrank, C.; Eisenmenger-Sittner, C.; Hutter, H.  
Applied Surface Science (2005), 252(1), 266-270.

Abstract:

In the design of new high-speed chip generations a huge problem is bleeding off process heat during their operation. The installation of heat sinks onto such chips is necessary. Possible materials are copper-coated carbon composites. They combine high thermal cond. with low d. and a tailorable coeff. of thermal expansion (CTE). The low wettability of copper onto carbon necessitates a surface pretreatment. Flat slices of nitrogen-plasma etched vitreous carbon (Sigradur G) made up as a model system for carbon fiber material. The later serial fabrication of these fibers includes a hot pressing step after the deposition joining them to solid composites. It is simulated by a heat treatment step of the compd. The first sample series consisted of samples with 100 nm molybdenum and 500 nm copper layers (sputter deposited), as deposited and heat treated. The second run concludes samples without molybdenum layer but an addnl. 50 nm cap layer deposited after heat treatment. All samples were investigated with secondary ion mass spectrometry (SIMS), showing a diffusion of carbon into the molybdenum layer. Measuring MCs<sup>+</sup> secondary ions, both matrix elements and trace elements were detectable sufficiently.

Citations

- 1) Dezellus, O; Scripta Mater 1999, 40, 283
- 2) Mortimer, D; J Mater Sci 1973, 8, 640
- 3) DeVincent, S; J Mater Eng Perform 1993, 2, 323
- 4) Mayerhofer, K; Anal Bioanal Chem 2002, 374, 602
- 5) Mayerhofer, K; Appl Surf Sci 2001, 179, 275
- 6) Neubauer, E; Thin Solid Films 2003, 433, 160
- 7) Neubauer, E; Surf Coat Technol 2004, 180/181, 496
- 8) Eisenmenger-Sittner, C; Surf Coat Technol 2004, 180/181, 413
- 9) Schrank, C; Thin Solid Films 2004, 459, 276
- 10) Anon; Leaflet: HTW Hochtemperaturwerkstoffe GmbH, [www.htw-germany.com](http://www.htw-germany.com)
- 11) Dubgen, R; Glasartiger Kohlenstoff SIGRADUR--ein Werkstoff fur Chemie und Technik, Information leaflet of HTW Hochtemperaturwerkstoffe
- 12) Schrank, C; Thin Solid Films 2004, 459, 276
- 13) Gnaser, H; Vac Sci Technol A 1994, 12, 452
- 14) Gnaser, H; Secondary Ion Mass Spectrometry, SIMS 8, Proceedings of the Eighth International Conference 1992, 95
- 15) Anon; [www.srim.org](http://www.srim.org)
- 16) Warnes, B; J Less-Common Metals 1985, 106, 241
- 17) Isobe, Y; J Less-Common Metals 1989, 147, 261

## 5.5. Dose-rate dependence of damage formation in Si by N implantation as determined from channelling profile measurements

Otto, G.; Hobler, G.; Palmeshofer, L.; Mayerhofer, K.; Piplits, K.; Hutter, H.  
Nuclear Instruments & Methods in Physics Research, Section B: Beam Interactions with Materials and Atoms (2006), 242(1-2), 667-669.

### Abstract

While the dose-rate effect of ion implantation in Si is well known, a quant. description of the amt. of damage as a function of dose-rate has only been given for self-implantation. In order to investigate the dose-rate effect for light ion implantation, we have implanted 30 keV N at room temp. at dose-rates between 10<sup>10</sup> and 5 x 10<sup>12</sup> cm<sup>-2</sup> s<sup>-1</sup> and measured the resulting damage by 30 keV B implanted in [1 1 0] channelling direction by SIMS. In addn. one sample has been prepd. with the N implant performed at liq. nitrogen temp. We propose a method to ext. the relative amt. of damage from the channelling profiles. The amt. of damage caused by the N implant shows a sigmoidal dependence on the dose-rate with a transition region between 10<sup>12</sup> and 5 x 10<sup>12</sup> cm<sup>-2</sup> s<sup>-1</sup> where the damage increases by a factor of 1.6. This behavior is in contrast to the power law found for self-implantation.

### Citations:

- 1) F.H. Eisen, B. Welch, Radiat. Eff. 7 (1971) 143.
- 2) F.H. Eisen, B. Welch, J.E. Westmoreland, J.W. Mayer, in: Atomic Collision Phenomena in Solids, North-Holland, 1970, p. 111.
- 3) S. Prussin, P.F. Zhang, in: Ion Implantation Technology-96, IEEE, 1997, p. 555.
- 4) M. Posselt, L. Bischoff, J. Teichert, Appl. Phys. Lett. 79 (2001) 1444.
- 5) L. Bischoff, J. Teichert, S. Hausmann, Nucl. Instr. and Meth. B 178, (2001) 165.
- 6) O.W. Holland, D. Fathy, J. Narayan, O.S. Oen, Nucl. Instr. And Meth. B 10-11 (1985) 565.
- 7) O.W. Holland, D. Fathy, J. Narayan, O.S. Oen, Radiat. Eff. 90 (1985) 127.
- 8) S. Prussin, O.W. Holland, Nucl. Instr. and Meth. B 127-128 (1997) 18.
- 9) M.D. Giles, S. Yu, H.W. Kennel, P.A. Packan, Mater. Res. Soc. Symp. Proc. 469 (1997) 253.
- 10) G. Hobler, Nucl. Instr. and Meth. B 96 (1995) 155.
- 11) G. Hobler, G. Otto, D. Kovac, L. Palmeshofer, K. Mayerhofer, K. Piplits, Nucl. Instr. and Meth., submitted for publication.
- 12) G. Otto, D. Kovac, G. Hobler, Nucl. Instr. and Meth., submitted for publication.

## 5.6. Range evaluation in SIMS depth profiles of Er-implantations in silicon

Mayerhofer, K.; Foisner, H.; Piplits, K.; Hobler, G.; Palmetshofer, L.; Hutter, H.  
Applied Surface Science (2005), 252(1), 271-277.

### Abstract

In the last decade ion implantation of common dopants in silicon has been almost full characterised. However, data of inner transition elements are based on few measurements or even extrapolations. Our investigations focus on erbium, an upcoming dopant in photonic applications. Some of us have previously found errors of 20% in the projected range of Er in Si and SiO<sub>2</sub> when comparing the range profiles measured with SIMS and simulations using SRIM, T2D, and our own binary collision simulator IMSIL. Because of the far-reaching consequences, we have performed addnl., more precise expts. to confirm our previous results. Equal doses of Er has been implanted into SIMOX wafers with energies of 100, 200, 300, 400, 500, and 600 keV. Profiles have been measured with secondary ion mass spectrometry (SIMS). Relative sensitivity factors (RSF) were gathered from low-energy implantations, remaining within the Si top layer. We used the Si/SiO<sub>2</sub> interface at exactly 217.7 nm to calibrate the depth scale of all profiles. In addn. dynamical Monte-Carlo simulations of the sputter process were taken to correct the depth scale and the interface position.

- 1) Kenyon, A; Prog Quant Electron 2002, 26, 225
- 2) Anon; <http://www.srim.org>
- 3) Ziegler, J; The Stopping and Range of Ions in Solids 1985, 1
- 4) Ziegler, J; Handbook of Ion Implantation Technology 1992, 1
- 5) Palmetshofer, L; Mater Sci Eng B-Solid 2001, B81, 83
- 6) Piplits, K; Proceedings of the SIMS VIII 1992, 199
- 7) Piplits, K; Proceedings of the SIMS X 1995, 1007
- 8) Biersack, J; Appl Phys A 1984, 34, 73
- 9) Ullrich, M; Nucl Instrum Methods B 2005, 228, 373
- 10) van der Heide, P; Nucl Instrum Methods B 2003, 201, 413
- 11) Schueler, B; J Vac Sci Technol B 2000, 18, 496
- 12) Ronsheim, P; J Vac Sci Technol B 2000, 18, 501
- 13) Biersack, J; Nucl Instrum Methods B 1999, B153, 398
- 14) Stevie, F; J Vac Sci Technol A 1988, 6, 76
- 15) Prenitzer, B; Proceedings of the 12th International Conference on Secondary Ion Mass Spectrometry 2000, 77
- 16) Dowsett, M; J Vac Sci Technol B 1994, 12, 186

## **5.7. Multiscale approach for the analysis of channelling profile measurements of ion implantation damage**

Hobler, G.; Otto, G.; Kovac, D.; Palmetshofer, L.; Mayerhofer, K.; Piplits, K. Institut fuer Festkoerperelektronik, Vienna University of Technology, Vienna, Austria. Nuclear Instruments & Methods in Physics Research, Section B: Beam Interactions with Materials and Atoms (2005), 228(1-4), 360-363. Publisher: Elsevier B.V., CODEN: NIMBEU ISSN: 0168-583X. Journal written in English. CAN 142:487852 AN 2005:20037 CAPLUS

### Abstract

Coupled binary collision and kinetic lattice Monte Carlo simulations are used to analyze 30 keV B channelling profile measurements of damage from 30 keV N implants in (1 1 0)-Si. Collision cascades are generated in the binary collision approach, while dynamic annealing and post-implant annealing at room temp. are treated within the kinetic lattice Monte Carlo approach. In the binary collision simulations the atom positions of each defect and the lattice strain around the defects are considered. Strain is shown to have a weak but non-negligible effect on the channelling of 30 keV B. Comparison of the simulation results with the B profiles measured by SIMS suggests that interstitials and vacancies are attracted by clusters of the opposite type and/or repelled by clusters of the same type.

Indexing -- Section 65-4 (General Physical Chemistry)

### Citations

- 1) Giles, M; Materials Research Society Symposium Proceedings 1997, 469, 253
- 2) Hobler, G; J Vac Sci Technol B 1996, 14, 272
- 3) Yang, S; IEEE Trans Semicond Manufacturing 1996, 9, 49
- 4) Posselt, M; J Electrochem Soc 1997, 144, 1495
- 5) Lulli, G; Phys Rev B 2004, 69, 165216
- 6) Balboni, S; Phys Rev B 2002, 66, 045202
- 7) Westmoreland, J; Appl Phys Lett 1969, 15, 308
- 8) Holland, O; Radiat Eff 1985, 90, 127
- 9) Tian, S; IEEE Trans Electron Dev 1998, 45, 1226
- 10) Hobler, G; Nucl Instr and Meth B 1995, 96, 155
- 11) Kresse, G; Phys Rev B 1996, 54, 11169
- 12) Hobler, G; Radiat Eff Def Sol 1996, 139, 21
- 13) Hobler, G; Nucl Instr and Meth B 2003, 206, 81

## 5.8. Quantitative SIMS depth profiling of diffusion barrier gate-oxynitride structures in TFT-LCDs

Dreer, Sabine; Wilhartitz, Peter; Piplits, Kurt; Mayerhofer, Karl; Foisner, Johann; Hutter, Herbert.

Analytical and Bioanalytical Chemistry (2004), 379(4), 599-604

### Abstract

Gate oxynitride structures of TFT-LCDs were investigated by SIMS, and successful solns. are demonstrated to overcome difficulties arising due to the charging effects of the multilayer systems, the matrix effect of the method, and the small pattern sizes of the samples. Because of the excellent reproducibility achieved by applying exponential relative sensitivity functions for quant. anal., minor differences in the barrier gate-oxynitride compn. deposited on molybdenum capped aluminum-neodymium metalization electrodes were detd. between the center and the edge of the TFT-LCD substrates. No differences were found for molybdenum-tungsten metalizations. Furthermore, at the edge of the glass substrates, aluminum, neodymium, and molybdenum SIMS depth profiles show an exponential trend. With TEM micrographs an inhomogeneous thickness of the molybdenum capping is revealed as the source of this effect, which influences the elec. behavior of the device. The prodn. process was improved after these results and the aging behavior of TFT-LCDs was investigated in order to explain the change in control voltage occurring during the lifetime of the displays. SIMS and TEM show an enrichment of neodymium at the interface to the molybdenum layer, confirming good diffusion protection of the molybdenum barrier during accelerated aging. The reason for the shift of the control voltage was finally located by semi-quant. depth profiling of the sodium diffusion originating from the glass substrate. Molybdenum-tungsten was a much better buffer for the highly-mobile charge carriers than aluminum-neodymium. Best results were achieved with PVD silicon oxynitride as diffusion barrier and gate insulator deposited on aluminum-neodymium metalization layers.

- 1) Dreer, S; Pure Appl Chem (accepted for publication) 2003
- 2) Dreer, S; Fresen J Anal Chem 1999, 365, 29
- 3) Dreer, S; Mikrochim Acta 2000, 133, 75
- 4) Homma, Y; Secondary ion mass spectrometry SIMS IX 1994, 135
- 5) Breuer, U; Fresen J Anal Chem 1995, 353, 372
- 6) Gnaser, H; Fresen J Anal Chem 1991, 341, 54
- 7) Okada, Y; Appl Phys Lett 1992, 61, 3163

## 5.9. Investigations of corrosion phenomena of gold coins with SIMS

Mayerhofer, K. E.; Piplits, K.; Traum, R.; Griesser, M.; Hutter, H.  
Applied Surface Science (2005), 252(1), 133-138

### Abstract

This work focuses on secondary ion mass spectrometry (SIMS) investigations merely showing the distribution of electroneg. elements, such as sulphur, oxygen, and chlorine on the surface. Sulphur is highly suspected of causing the obsd. corrosion phenomena, and is indeed enriched near polluting splints. Since SIMS is a destructive method, the investigated samples are test coins with intentionally added impurities. These coins were manufd. in cooperation with the Austrian Mint. They were treated with potassium polysulfide ( $K_2S_x$ ) for 8 h gaining a rapid corrosion of the surface. SIMS mass spectra, depth profiles, and images were done (a) at non-polluted areas, (b) near polluted areas with slight coloring, and (c) directly at polluting stains showing enrichments of sulphur and chlorine. Due to the success of these investigations further studies on historic coins are intended.

### Citations

- 1) Anon; <http://www.khm.at/>
- 2) Griesser, M; Numismatic and Technology: Question and Answers 2003
- 3) Oddy, W; III: Papers of the Leiden Seminar 1993
- 4) Gusmano, G; Appl Phys A 2004, 79, 205
- 5) Linke, R; Numismatische Zeitschrift 1999, 106-107, 173
- 6) Rupprecht, L; Numismatic and Technology: Question and Answers 2003
- 7) Anon; <http://www.austrian-mint.com/>
- 8) Hutter, H; Anal Bioanal, Chemistry 1996, 355, 585

## 5.10. Brown spot corrosion on historic gold coins and medals

M. Griesser, R. Traum, K. E. Mayerhofer, K. Piplits, R. Denk and H. Winter  
Surface Engineering 2005, Vol 21 (5–6), 385-392

In 1998, in the Coin Cabinet of the Kunsthistorisches Museum, Vienna, Austria, brown spot corrosion was detected on about 400 gold coins and medals minted in Central Europe between the late 18th and early 20th century. The cause of the brown spots, their temporal and spatial frequency, the development of the corrosion and the most suitable restoration treatments and storage conditions for these objects has been and is still being studied. For the analysis of the historic coins and medals—as well as a set of test ducats produced in cooperation with the Austrian Mint—different analytical methods, i.e. light microscopy, scanning electron microscopy (SEM), measurement of polarisation curves, and secondary ion mass spectrometry (SIMS) were combined. From these investigations and the study of historical sources it could be shown that the brown spot corrosion is due to the inclusion of silver and/or silver/copper containing particles into the surface of the coins and medals. These inclusions are incorporated during the minting process. Afterwards they corrode to silver and copper sulphides owing to the presence of air pollution and objects releasing sulphur containing compounds (i.e. gypsum casts) nearby the historical objects.

Citations:

- 1) R. Linke, M. Schreiner, R. Denk and R. Traum: *Numismatische Zeitschrift*, 1999, 106/107, 173–179.
- 2) W. A. Oddy: in 'Images for posterity: the conservation of coins and medals', 29–40; 1995, Leiden, Rijksmuseum Het Koninklijk Penningkabinet.
- 3) G. Gusmano, R. Montanari, S. Kaciulis, G. Monesperelli and R. Denk: *Mater. Sci. Proc.*, 2004, A79, (2), 205–211.
- 4) L. Rupprecht, R. Montanari and G. Gusmano: in 'Numismatic and technology: question and answers', 99–112; 2003, Vienna, The Kunsthistorisches Museum.
- 5) H. Hutter, C. Brunner, S. Nikolov, C. Mittermayer and M. Grasserbauer: *Fresenius' J. Anal. Chem.*, 1996, 355, 585–590.
- 6) H. Ertl: *Numismatische Zeitschrift*, 1989, 100, 113–128.
- 7) J. Cribb (ed.): 'Money – from cowrie shells to credit cards'; 1986, London, British Museum.
- 8) 'Das Münzen des neuen deutschen Reichsgeldes', in: 'Deutscher Hausschatz in Wort und Bild', Vol. 2, No. 8 (Okt. 1875–Okt. 1876), 123–128; Verlag von Franz Pustet, Regensburg.
- 9) E. Schlösser: 'Die Münztechnik. Ein Handbuch für Münztechniker, Medaillenfabrikanten, Gold- und Silberarbeiter, Graveure und technische Chemiker', Hannover, 1884.
- 10) P. Arnold and U. Arnold (eds.): 'Münzstättenbesichtigungen der sächsischen Münz- und Hüttenmeister Gustav Julius Buschick und Theodor Choulant', *Numismatische Studien*, No. 9; 1991, Abt. Münzkabinett, Museum für Hamburgische Geschichte.
- 11) D. R. Cooper: 'The art and craft of coinmaking. A history of minting technology'; 1988, London, Spink & Son.
- 12) S. Becher: 'Das österreichische Münzwesen vom Jahre 1524 bis 1838 in historischer, statistischer und legislativer Hinsicht', 2 Volumes, 1838, Vienna, Möslé's Witwe und Braumüller.



- 13) J. Hassenbauer: '2. Reisebericht des kk. Hauptmünzamts Obergoldscheiders über die kk Münzstätten zu Venedig und Mailand, 1836.
- 14) A. Soetbeer: 'Deutsche Münzverfassung mit Erläuterungen', Appendix IV, 'Die Einrichtung und der Geschäftsgang der Münze in Berlin mit besonderer Rücksicht auf die Ausprägung der Reichsgoldmünzen', Erlangen, 1874.
- 15) M. Griesser, R. Denk, M. Griehl, R. Traum and H. Winter: in 'Numismatic and technology: question and answers', 91–98; 2003, Vienna, Kunsthistorisches Museum.

## 6. Images

Image 1: From <http://cim.aamu.edu/French/gcfr.html> (Howard J. Foster Center for Irradiation of Materials)

Images 44, 74, 75, 81, 84, 86, 88, 90: Rene Traum, Kunsthistorisches Museum Wien; reworked by Karl E. Mayerhofer

Image 96: S. Dreer in [68]

All other images by Karl E. Mayerhofer

- 
- 1 Online: <http://www.iontof.com/>
  - 2 Online: <http://www.minisims.com/home.htm>
  - 3 R. F. K. Herzog, F. P. Viehböck, *Phys. Rev.* 76(1949) 855f
  - 4 A. Benninghoven, F. G. Rüdener, H. W. Werner; *Secondary ion mass spectrometry*; Wiley Interscience publication, John Wiley & Sons; New York; ISBN 0-471-01056-1; (1987)
  - 5 Online: [http://en.wikipedia.org/wiki/Secondary\\_ion\\_mass\\_spectrometry](http://en.wikipedia.org/wiki/Secondary_ion_mass_spectrometry)
  - 6 H. Werner, H. de Grefte; *Vakuum-Technik*, 17, 37 (1968)
  - 7 R. Castaing, G. Slodzian; *J. Microscopie* (1962), 1(6), 395-410
  - 8 R. Wilson, F. Stevie, C. Magee; *Secondary Ion Mass Spectrometry*; Wiley Interscience publication, John Wiley & Sons; New York; ISBN 0-471-51945-6, (1989)
  - 9 Online: <http://www.cameca.fr/>
  - 10 A. Benninghoven, *Surface investigation of solids by the statical method of secondary ion mass spectroscopy (SIMS)*, *Surf. Sci.* 35 (1973) 427– 437.
  - 11 A. Bergauer, C. Eisenmenger-Sittner; *Physik und Technologie dünner Schichten*; Skriptum
  - 12 B. Rasser, D. Renard, M. Schuhmacher, *Secondary Ion Mass Spectrometry, SIMS 9, Proceedings of the Ninth International Conference 1993*, 278-281;
  - 13 H. Bubert, H. Jenett; *Surface and thin film analysis*; Wiley-VCH Verlag, D-69469 Weinheim (Germany); ISBN 3-527-30458-4; (2002)
  - 14 Online: <http://www.eaglabs.com/en-US/references/tutorial/simsinst/caisinst.html>
  - 15 R. Van Ham, L. Van Vaeck, A. Adriaens, F. Adams, B. Hodges, A. Appelhans, G. Groenewold, *International J. mass. Spectrum.* (2005), 247(1-3), 28-36;
  - 16 G. Slodzian, *Nat. Bur. Stand. U.S. Spec. Publ.* 427 (1975)
  - 17 Rouberol, J. M.; Lepareur, M.; Autier, B.; Gourgout, J. M. *Proceedings, Annual Conference - Microbeam Analysis Society (1977)*, 12 (*Int. Conf. X-Ray Opt. Microanal.*, 8th Annu. Conf. Microbeam Anal. Soc.), 133A-133D.
  - 18 H.N. Migeon, C. Le Pipec, J.J. Le Goux; *Secondary Ion Mass Spectrometry, SIMS 5, Proceedings of the Fifth International Conference 1985*, 155-160;
  - 19 H.N. Migeon, B. Rasser, M. Schuhmacher, J.J. Le Goux; *Secondary Ion Mass Spectrometry, SIMS 8, Proceedings of the Eighth International Conference 1991*, 195-198;
  - 20 Online: [http://www.cameca.fr/html/product\\_ims7f.html](http://www.cameca.fr/html/product_ims7f.html)
  - 21 M. Schuhmacher, B. Rasser, F. Desse, *CAMECA . J. Vac. Sci. Technol. B* 18 (1), Jan/Feb 2000; 529-532

- 
- 22 M. Grasserbauer, G. Stingeder, E. Guerrero, W. Fallmann; *Mikrochimica Acta* (1981), 2(5-6), 469-82.
- 23 E. Zinner, M. Grasserbauer; *Springer Series in Chemical Physics* (1982), 19(Second. Ion Spectrom. SIMS3), 292-6;
- 24 K. Piplits, W. Tomischko, G. Stingeder, H. Hutter; *Secondary Ion Mass Spectrometry, SIMS 8, Proceedings of the Eighth International Conference 1991*, 199-202
- 25 K. Piplits, W. Tomischko, Ch. Brunner, H. Hutter; *Secondary Ion Mass Spectrometry, SIMS 10, Proceedings of the Tenth International Conference 1995*, 1007-1010
- 26 **H. Hutter, Ch. Brunner, St. Nikolov, Ch. Mittermayr, M. Grasserbauer**; *Fresenius J Anal Chem* (1996) 355:585-590
- 27 **Hutter, H.; Nowikow, K.; Gammer, K.**; *Appl. Surf. Sci.* (2001), 179(1-4), 162-167
- 28 Online: [http://www.cameca.fr/html/product\\_nanosims.html](http://www.cameca.fr/html/product_nanosims.html)
- 29 Pierson, H. O.; *Handbook of carbon, graphite, diamond and fullerenes properties, processing and application* (1993); Park Ridge, New Jersey; ISBN: 0-8155-1339-9
- 30 E. Pop, D. Mann, Q. Wang, K. Goodson, H. Dai; *Nano Lett.* (2006), 6(1), 96-100;
- 31 M.J. Biercuk, M.C. Llaguno, M. Radosavljevic, J.K. Hyun, and A.T. Johnson; *Appl. Phys. Lett.*; 80(2002), 2767.
- 32 Neubauer, Erich; *Interface optimisation in copper carbon metal matrix composites*; Dissertation 2003, TU-Wien, Vienna
- 33 Mortimer, D; *J Mat Sci* 1970, 5, 149
- 34 Mortimer, D; *J Mat Sci* 1973, 8, 640
- 35 [http://www.htw-germany.com/en/content/physical\\_properties.php](http://www.htw-germany.com/en/content/physical_properties.php)
- 36 Sittner, Ch.; Bangert, H.; Duschlbauer, D.; Pettermann, H.; Korb, G.; *Mater. Technol.* (2003), 18(3), 144-149
- 37 Gnaser et al (energieverteilung negativer c-ionen)
- 38 C. Schrank ,C. Eisenmenger-Sittner, E. Neubauer, H. Bangert, A. Bergauer; *Thin Solid Films* 459 (2004) 276–281;
- 39 M. Rosner, E. Neubauer, Ch. Eisenmenger-Sittner, H. Bangert, H. Hutter; *Anal Bioanal Chem* (2004) 380, 838–842;
- [40] M. Rosner, C. Eisenmenger-Sittner, H. Hutter, *Microchim. Acta* 133 (2000) 267–271.
- 41 E. Neubauer, C. Eisenmenger-Sittner, H. Bangert, G. Korb, C. Thomastik; *Surf. Coat. Tech.* 180 –181 (2004) 496–499

- 
- 42 Mortimer, D. A.; Nicholas, M. G.; Crispin, R. M.; *Plastics & Polymers, Conf. Suppl.* 6 (1974), 101-4.
- 43 Online: <http://www.srim.org>
- 44 E. Neubauer, G. Korb, C. Eisenmenger-Sittner, H. Bangert, S. Chotikaprakhan, D. Dietzel, A.M. Mansanares, B.K. Bein; *Thin Solid Films* 433 (2003) 160–165
- 45 C. Eisenmenger-Sittner, E. Neubauer, C. Schrank, J. Brenner, C. Tomastik; *Surf. Coat. Tech.* 180 –181 (2004) 413–420
- 46 B.M. Warnes, G. Simkovich, *J. Less-Common Metals* 106; (1985) 241–249
- 47 Y. Isobe, P. Son, M. Miyake, *J. Less-Common Metals* 147; (1989) 261–268
- 48 Online: <http://www.khm.at/homeE/homeE.html>
- 49 Online: <http://www.khm.at/staticE/page23.html>
- 50 Online: <http://www.austrian-mint.com/e/menu.htm>
- 51 R. Linke, M. Schreiner, R. Denk and R. Traum: *Numismatische Zeitschrift*, 1999, 106/107, 173–179.
- 52 G. Gusmano, R. Montanari, S. Kaciulis, G. Monesperelli and R. Denk: *Mater. Sci. Proc.*, 2004, A79, (2), 205–211.
- 53 Online: <http://winter.group.shef.ac.uk/chemputer/isotopes.html>
- 54 M. Grießer, M. Kurznel-Runtscheiner, M. Novotny-Kargl in *Technologische Studien, Band 2/2005*, 87-115; Kunsthistorisches Museum, Wien (Eigenverlag); ISBN 3-85497-098-6
- 55 Online: <http://www.fz-juelich.de/zch/oberfl/>
- 56 Ionspec application; version 4.1.0.1 © IONTOF GmbH 1996-2004
- 57 Online: <http://de.wikipedia.org/wiki/Ionenimplantation>
- 58 H. Ryssel, I. Ruge: *Ionenimplantation*; Teubner; Stuttgart; ISBN: 3-519-03206-6
- 59 *The Stopping and Ranges of Ions in Matter, Vol. 1: The Stopping and Range of Ions in Solids.*; Ziegler, J. F.; Biersack, J. P.; Littmark; Pergamon Press, New York, USA (1985), ISBN: 0-08-021606-4
- 60 Online: <http://www.srim.org/SRIM/History/HISTORY.htm>
- 61 L. Palmetshofer, M. Gritsch, G. Hobler; *Mater Sci Eng B-Solid* 2001, B81, 83
- 62 Online: <http://www.fke.tuwien.ac.at/hobler/research/implant.htm>
- 63 Gnaser, H; *Secondary Ion Mass Spectrometry, SIMS 8, Proceedings of the Eighth International Conference* 1992, 95
- 64 Gnaser, H; *Vac Sci Technol A* 1994, 12, 452

---

65 S. Dreer; Quantitative characterisation of silicon- and aluminium oxynitride films produced by reactive dc-magnetron sputtering; Dissertation, Vienna, Technical University, 2000

66 S. Dreer, P. Wilhartitz, E. Mersdorf, G. Friedbacher; Mikrochim. Acta 130, 281-288 (1999)

67 S. Dreer; Fresenius J. Anal. Chem. (1999) 365; 85-95

68 S. Dreer, P. Wilhartitz, K. Piplits, H. Hutter, M. Kopnarski, G. Friedbacher; Mikrochim. Acta 133, 75-87 (2000)